An investigation of non-equilibrium effects in thermal argon plasmas

Citation for published version (APA):
Rosado, R. J. (1981). *An investigation of non-equilibrium effects in thermal argon plasmas*. [Phd Thesis 1 (Research TU/e / Graduation TU/e), Applied Physics and Science Education]. Technische Hogeschool Eindhoven. https://doi.org/10.6100/IR79267

DOI:
10.6100/IR79267

Document status and date:
Published: 01/01/1981

Document Version:
Publisher's PDF, also known as Version of Record (includes final page, issue and volume numbers)

Please check the document version of this publication:

• A submitted manuscript is the version of the article upon submission and before peer-review. There can be important differences between the submitted version and the official published version of record. People interested in the research are advised to contact the author for the final version of the publication, or visit the DOI to the publisher's website.
• The final author version and the galley proof are versions of the publication after peer review.
• The final published version features the final layout of the paper including the volume, issue and page numbers.

Link to publication

General rights
Copyright and moral rights for the publications made accessible in the public portal are retained by the authors and/or other copyright owners and it is a condition of accessing publications that users recognise and abide by the legal requirements associated with these rights.

- Users may download and print one copy of any publication from the public portal for the purpose of private study or research.
- You may not further distribute the material or use it for any profit-making activity or commercial gain
- You may freely distribute the URL identifying the publication in the public portal.

If the publication is distributed under the terms of Article 25fa of the Dutch Copyright Act, indicated by the "Taverne" license above, please follow below link for the End User Agreement:

www.tue.nl/taverne

Take down policy
If you believe that this document breaches copyright please contact us at:

openaccess@tue.nl

providing details and we will investigate your claim.

Download date: 04. Oct. 2023

AN INVESTIGATION OF NON-EQUILLIBRIUM EFFECTS IN THERMAL ARGON PLASMAS

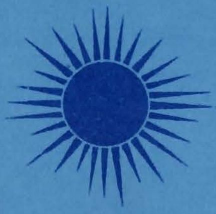

RUI JOSÉ ROSADO

AN INVESTIGATION OF NON-EQUILIBRIUM
EFFECTS IN THERMAL ARGON PLASMAS

proefschrift

Ter verkrijging van de graad van doctor in de
Technische Wetenschappen aan de Technische
Hogeschool Eindhoven, op gezag van de Rector
Magnificus, prof.ir. J. Erkelens, voor een
commissie aangewezen door het College van
Dekanen in het openbaar te verdedigen op
vrijdag 23 oktober 1981 te 16.00 uur

door

Rui José Rosado

geboren te Willemstad

DIT PROEFSCHRIFT IS GOEDGEKEURD
DOOR DE PROMOTOREN

PROF.DR.~~IR.~~ D.C. SCHRAM
EN
PROF.DR. N.F. VERSTER

With a little help
from my friends ...

CONTENTS

CHAPTER I, GENERAL INTRODUCTION

The study of the plasma state has always been accompanied by the evaluation of the validity criteria for the description of the plasma state by an equilibrium model.

The more a plasma approaches equilibrium, the less parameters are needed to describe radiation emission, absorption and transport coefficients. In the case of complete thermodynamic equilibrium, a description in terms of one parameter, the temperature, is possible. In the other limit there is no equilibrium, and detailed information about excitation, ionisation and radiation processes, and the reverse processes is needed to describe the excitation state. Additionally, information about momentum transfer cross-sections has to be supplied.

In order to use a certain equilibrium model, the limitations of the model with respect to the determination of plasma parameters, e.g. electron temperature and density, have to be established.

As laboratory plasmas are almost never in Complete Thermodynamic Equilibrium, the study of the Local Thermal Equilibrium (LTE) model has become very important. For many applications this model is used to determine plasma parameters. Directly connected with this, the study of the next model in the equilibrium hierarchy, the Partial Local Thermal Equilibrium (PLTE) model has gained importance. [CIL75, GRI64, VEN71]

One type of plasma that has received interest for its applications in industry and in applied physics is the high current, atmospheric pressure arc discharge. The atmospheric pressure arc plasma is nowadays widely used in such applications as plasma jet cutting, plasma spraying and plasma welding.[FAU79]

Noble gas arc plasmas provide an adequate high temperature environment, for the study of chemical reactions. Inductively heated arcs are currently being used, e.g. in element analysis. [VEN71]

One line of study on arc plasmas is their possible application as absolute intensity standards. The quality of importance in this case is the high intensity that can be produced by high pressure arcs. Although most interest is directed at the use of hydrogen as the arc gas, argon also has its merits, specially because of the high emission intensity in the vacuum ultra violet spectral region. [BRI77a, BRI77b, OTT75, OTT76, SAV78]

For all these applications, a good description of the plasma parameters is very important. The applicability of the LTE model versus the PLTE model becomes of special interest, as the arc plasma is usually close to, but not already in, LTE.

In the past several criteria for the validity of LTE have been formulated, and expressed in terms of n_e, cf. [CIL75] . These criteria are obtained from models which account for the effects of diffusion, excitation, ionization and recombination. For illustration we compare three of the widely used criteria:

by Wilson et al. : $n_e > 6.10^{19}\ E_2^3\ \hat{T}_e^{\frac{1}{2}}\ m^{-3}$, [WIL62] (1a)

by Drawin : $n_e > 1.10^{20}\ E_2^3\ \hat{T}_e^{\frac{1}{2}}\ m^{-3}$, [DRA69] (1b)

by Griem : $n_e > 1.2.10^{22}\ E_2^3\ \hat{T}_e\ m^{-3}$ [GRI63] (1c)

where $\hat{T}_e$ is expressed in eV, and where E_2 represents the excitation energy of the first excited level, also in eV. With typical values for an atmospheric pressure argon arc plasma $\hat{T}_e$ = 1eV and E_2 = 10eV we obtain from (1) as criteria for LTE respectively (argon):

$n_e > 5.10^{22}$ m^{-3}, $n_e > 10^{23}$ m^{-3} and $n_e > 10^{25}$ m^{-3}.
These numbers demonstrate that the theoretically determined criteria for LTE are strongly dependent upon the point of departure in the reasoning. In addition, it is obvious that the value of T_e is also important in the establishment of LTE. This calls for a detailed further evaluation with emphasis on acquiring additional experimental data on the deviation from LTE.

The experimental study of LTE, motivated by the reasons sketched above, must thus be based on an accurate determination of T_e and n_e. In general, the measured values of n_e and T_e at a certain gas pressure are compared with values $n_{e,LTE}$ that follow from calculations of the plasma composition at that pressure, and temperature T_e assuming LTE. [CHA75, EDD73, UHL70]
A necessary condition is that no assumption of LTE is made in the derivation of the values of T_e and n_e from experimental quantities.
We have followed this approach, assuming that the argon plasma studied has already reached a PLTE state in which the populations of all the energy states of the argon neutral spectrum, with exception of the ground state, are in thermal equilibrium with the electrons. This assumption will be motivated in chapter 2.

The determination of the *electron temperature* then follows from measurement of the ratio of the population densities of two excited levels of the neutral-atom spectrum [LEC77, DRA73, PRE77]. The measurement technique involves the determination of the source function of a suitable emission line, i.e. the ratio of the emission - and the absorption coefficients of the line. [DRA73]
Measurements of the temperature in this way eliminates the need for a transition probability value in the calculations. On the other hand only sufficiently absorbed lines come into consideration for measurement. Moreover an absolute calibration of the line intensity is needed.

The *electron density* follows from the Saha relation, applied to the measured population densities. In this case the total line intensity is needed, and also the relevant transition probability value.

We also use an interferometric method to determine n_e. In this case the transition probability is not needed.

In our method, based on independent measurement of n_e and T_e, $(n_e, T_e)_{PLTE}$ points are obtained for one pressure value. These points lie on a curve that does not coincide with the LTE relation for n_e and T_e, $(n_e, T_e)_{LTE}$. This situation is represented in fig. 1.1.

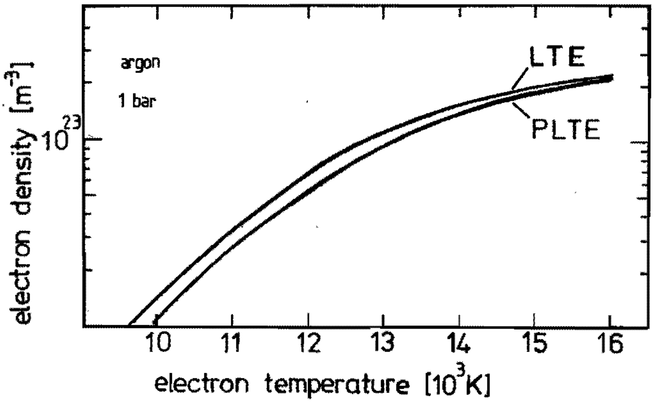

Fig. 1.1
Sketch of the LTE relationship between the electron density and the electron temperature and of the measured PLTE relationship.

Anticipating the results that will be described in chapter 5, this figure displays schematically our expectations of a situation that is farther from LTE at the lower n_e and T_e values and approaches LTE for higher values of n_e and T_e.

As will become clear later an important characteristic of the source function method is that small errors in the determination of T_e give such changes in the determination of the electron density, that the conclusion on the (n_e, T_e) interdependence is hardly affected.

If we compare our method with established methods found in the literature we note the following:

1. Some other methods require a more extensive variation of the conditions of measurement. For example, for the method based on the determination of the norm temperature of a certain line (e.g. [BOB70]), the maximum intensity of the line must be measured for several combinations of temperature and pressure. Moreover, this method enables only the check of validity of LTE in the neighbourhood of the norm temperature.
2. Another method, proposed by Richter [RIC71] is based on measurement of the intensities of two lines from different ionization stages. The comparison with LTE values is not unambiguous and an additional, separate and accurate measurement of T_e is still needed.

Although the plasma equilibrium is usually investigated under stationary conditions, in this thesis we also report on the study of the (n_e, T_e) relation under time varying conditions. In these experiments the plasma current is increased for a short period of time (about 0.5 ms) to a substantially higher value. The current-pulse duration is long enough, so that significantly higher values of T_e and n_e can be attained, with the same equipment.

A second result, obtained from the pulsed experiments, is information concerning the mechanisms that determine the deviation from LTE. Furthermore the rise and fall times associated with the establishment of the new plasma state and subsequent decay to the original state can be studied.[PIE78]
In the pulsed experiments we again use the source function method to determine T_e. This is justified because the time constant associated with the establishment of a PLTE population is much shorter than the rise-time of the applied current pulse. The electron density is determined interferometrically.

In this thesis a theoretical model for the deviation from equilibrium of the excited states of the plasma will be described in chapter II.
In chapter III an analysis of the measurement methods will be given. The source function method will be described in detail, together with the application of this method in the pulsed experiments. The interferometric method will also be discussed. Chapter IV concerns the experimental set-up and contains a description of the arrangements and of the optics, both for the spectroscopic and the interferometric set-up. The data collection and analysis are also treated..
A description of the current pulse system is also given.
Results of the stationary measurements are found in chapter V. In particular the (n_e, T_e) relations will be dealt with in detail. The experimentally obtained relationship is used for the determination of transport properties. Special attention is dedicated to the consequences of using the $(n_e, T_e)_{LTE}$ relation in the determination of plasma parameters.
The first results of our pulsed experiments are given in chapter VI. These results concern the behaviour of n_e and T_e under pulsed conditions as functions of time.
The last chapter, chapter VII, contains conclusions that have resulted from the present work.

CHAPTER II, EQUILIBRIUM CONSIDERATIONS FOR THE ARGON NEUTRAL SYSTEM

2.1 Introduction

The description of the density distribution among the excited states of a plasma by the Partial Local Thermal Equilibrium (PLTE) model allows for the introduction of deviations from Boltzmann statistics in the population of the excited levels.

In the argon neutral system (ArI) at atmospheric pressure and at temperatures of about 1eV, the ground level is usually overpopulated with respect to the other levels. For lower values of the temperature, even the excited states are not necessarily in equilibrium with the ground state of the next ionization stage (Saha equilibrium). [EDD73, BIB73]

An elaborate study of the overpopulation of several excited levels of the helium system has been published by Uhlenbusch et al. [UHL74], and in this context helium has received by far the most attention of the noblegasses. This is not so surprising as one of the major causes of overpopulation of the ground level, inward diffusion, is very pronounced in helium. In argon it is usually assumed beforehand that the deviation from equilibrium of the higher excited levels are negligible. [UHL70, LEC77, PRE78]

For a general approach to the problem of PLTE this assumption seems justified. However, the non-equilibrium population of the excited levels becomes an important factor when a more precise determination of the electron temperature from line intensity measurements is aimed at.

In this chapter we will use a collisional-radiative approach to determine population densities of the levels of a simplified model of the ArI system. Our aim is not to present an exhaustive description of all the contributing processes, but rather to illustrate the influence of the more important processes on the distribution of the population densities.

2.2 A collisional radiative model and the validity of PLTE

We will consider the balance equation for particles in state q and we use the convention N>r>p>q>1 for denoting the considered excited levels. The symbol N identifies the maximum level which needs to be considered; r and p are symbols of levels to be summed up (see fig. 2.1). The index i indicates summation over levels both above and below the level q.

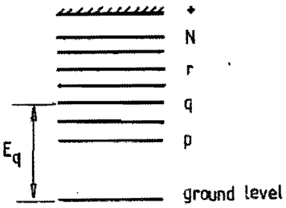

Fig. 2.1
Schematic representation of the distribution of excited levels in the energy spectrum with the notations used in this section.

The following balance equation results:

$$\frac{dn_q}{dt} = n_e\Big[\underbrace{\sum_{p=1}^{q-1} (n_p k_{pq} - n_q k_{qp})}_{\text{exc-deexc from below}} - \underbrace{\sum_{r=q+1}^{N} (n_q k_{qr} - n_r k_{rq})}_{\text{exc-deexc from above}} - \underbrace{n_q k_{q+}}_{\text{electr. ionization}} + \underbrace{n_e n_+ k^{(3)}_{+q}}_{\text{3 particle recombination}}\Big] +$$

$$\underbrace{n_e n_+ k^{(2)}_{+q} \quad \Lambda^{(2)}_{+q}}_{\text{radiative recombination}} - \underbrace{\sum_{p=1}^{q-1} n_q A_{qp} \Lambda_{qp}}_{\text{spontaneous emission}} + \underbrace{\sum_{r=q+1}^{N} n_r A_{rq} \Lambda_{rq}}_{\text{cascade radiation}} \qquad (2.1)$$

In table 2.1 the symbols are explained

Table 2.1
Symbols used in equation (2.1).

n_p	population density of state p
n_+	ion ground level density
k_{pq}	electron excitation rate p→q
k_{q+}	electron ionization rate from level q
$k^{(3)}_{+q}$	three particle recombination rate coefficient
$k^{(2)}_{+q}$	radiative recombination rate coefficient
$\Lambda^{(2)}_{+q}$	trapping coefficient for recombination radiation
A_{qp}	transition probability for transitions from state q to state p
Λ_{qp}	trapping coefficient for line radiation of the line q→p

Radiation absorption is treated by the inclusion of trapping coefficients, a local approximation, which is a valid description provided that the optical depth is large enough. This is only marginally valid for the free-bound radiation. We will return to the matter of the use of the local description later in this section (cf. section 2.2.2).

Using the principle of detailed balancing, equation (2.1) can be reduced to a simpler expression, which is especially valuable for situations close to (P)LTE. We introduce the reduced density b_q, defined as:

$$b_q = \frac{n_q}{n_{q,saha}} \tag{2.2}$$

where $n_{q,saha}$ is given by the Saha equation:

$$\frac{n_e n_+}{n_{q,saha}} = \frac{2g_+}{g_q}\left[\frac{2\pi m k T_e}{h^2}\right]^{1.5}\exp\left[-\frac{E_{01}-\Delta E_{01}-E_q}{kT_e}\right] \tag{2.3}$$

Here, g_+ is the statistical weight of the ion ground level, g_q is the statistical weight of excited level q, E_q is the energy of q (cf. fig. 2.1),

E_{01} is the ionization energy of the ArI system (E_{01}=15.759eV) and ΔE_{01} is the reduction of the ionization energy, which accounts for the influence of the surrounding particles on the discrete levels of the atom near the ionization limit. ΔE_{01} is given by: [GRI63]

$$\Delta E_{01} = C_{\Delta E}\sqrt{n_e/T_e}, \tag{2.4}$$

with

$$C_{\Delta E} \simeq 2.95\ 10^{-11}\ [\mathrm{eV\ m^{1.5}\ K^{0.5}}] \tag{2.4a}$$

The ratio of n_p to n_q in (2.1) is given by the Boltzmann equation

$$\frac{n_q}{n_p} = \frac{g_p}{g_q} \cdot \exp[-\frac{E_q-E_p}{kT_e}] \tag{2.5}$$

With the Saha equation and using the notation (2.2) and the principle of detailed balancing, we obtain for (2.1)

$$\frac{1}{n_{q,saha}} \cdot \frac{dn_q}{dt} = n_e[\sum_{\substack{i=1\\ i\neq q}}^{N} (b_i-b_q)k_{qi}-k_{q+}(b_q-1)] + R^{(2)}_{q+}k^{(2)}_{+q}\Lambda^{(2)}_{+q} -$$

$$\sum_{p=1}^{q-1} b_q A_{qp}\Lambda_{qp} + \sum_{r=q+1}^{N} b_r R_{rq} A_{rq}\Lambda_{rq} \tag{2.6}$$

where we have used the notations:

$$R^{(2)}_{q+} = \frac{n_e n_+}{n_{q,saha}} = \frac{2g_+}{g_q}\ [\frac{2\pi mkT}{h^2}]^{1.5} \exp[-\frac{E_{01}-E_q-\Delta E_{01}}{kT_e}] \quad \text{and} \tag{2.7}$$

$$R_{rq} = \frac{n_{r,saha}}{n_{q,saha}} = \frac{g_r}{g_q} \exp[-\frac{E_r-E_q}{kT_e}] \tag{2.8}$$

both, $R^{(2)}_{q+}$ and R_{rq}, are only functions of the electron temperature. The functions $R^{(2)}_{q+}$ and R_{pq} are shown in fig. 2.2a-2.2d for the temperature range of interest.

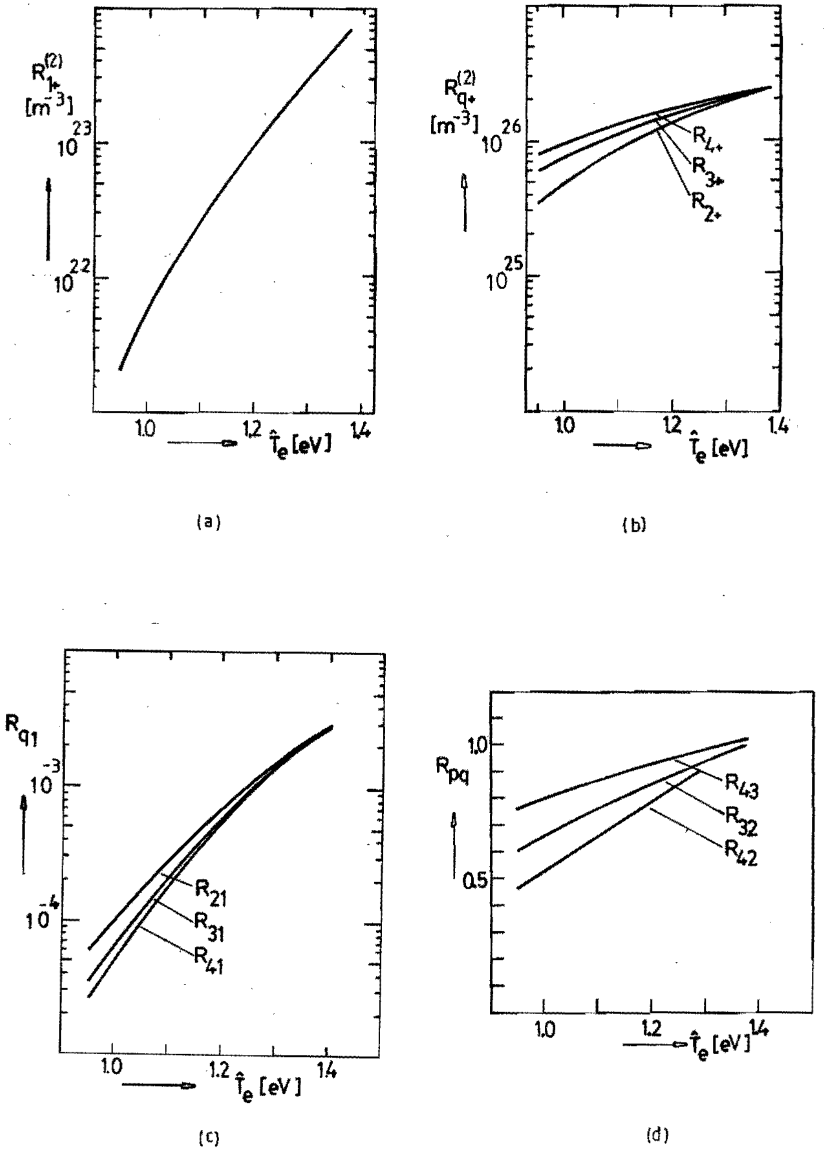

Fig. 2.2
The functions $R^{(2)}_{q+}$ *and* R_{rq} *(equations (2.7) and (2.8))for the considered effective levels of the 4 level model shown as functions of the temperature.*

For the relative deviation from Saha, $\delta b_q \equiv b_q - 1$, we obtain:

$$\frac{1}{n_{q,saha}} \cdot \frac{dn_q}{dt} = n_e \Big[\sum_{\substack{i=1 \\ i \neq q}}^{N} (\delta b_i - \delta b_q) k_{qi} - k_{q+} \delta b_q \Big] +$$

$$R^{(2)}_{q+} k^{(2)}_{+q} \Lambda^{(2)}_{+q} - \sum_{p=1}^{q-1} (1+\delta b_q) A_{qp} \Lambda_{qp} + \sum_{r=q+1}^{N} (1+\delta b_r) R_{rq} A_{rq} \Lambda_{rq} \qquad (2.9)$$

From this equation the non-equilibrium population of the different excited levels can be calculated.

Note that in (2.9) $\frac{dn_q}{dt}$ is defined by

$$\frac{dn_q}{dt} \equiv \frac{\partial n_q}{\partial t} + \mathrm{div}(n_q \underline{w}_q) \qquad (2.10)$$

where $\underline{w}_q$ stands for the diffusion velocity of particles in the state q.

Equation (2.9) represents a set of coupled equations which have to be solved simultaneously in order to obtain information about $\delta b_q (q=1, \ldots N)$ Provided that data about cross-sections are available this solution can be obtained from a straightforward numerical analysis. This lies outside the scope of the present study and would be redundant for the high density plasma under consideration, which is at least close to equilibrium. Therefore, we will choose another approach, considering only a limited number of levels, and making some a priori approximations.

Our simplified model of the argon level scheme is shown in fig. 2.3.

Here we consider all the sublevels of one group as e.g. 4s or 4p as one effective level. This is justified because of a sufficiently strong coupling between these sublevels. As typical example we can quote results for the $^3P_2$-$^3P_1$ sublevels of the 4s group for 1eV:

$n_e \langle \sigma v_e \rangle_{exc} \approx 5.10^9\ s^{-1}$ for $n_e \approx 10^{22}\ m^{-3}$ and $5.10^{10} s^{-1}$ for $n_e = 10^{23}\ m^{-3}$.

These rates are considerably larger than the transition probabilities.

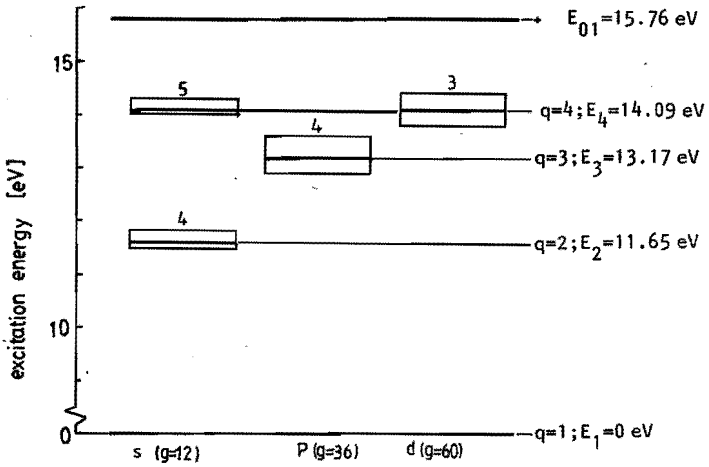

Fig. 2.3
Simplified diagram of the considered ArI excited levels showing the relation with our 4 level model.

If the rates for excitation from the sublevels of one group to the sublevels of the other group are not too much different, then it is justified to average over the sublevels, and consequently use the effective level scheme described above. In appendix A, definitions and numerical values for the effective energies, statistical weights and other relevant quantities are given.

Now we will derive expressions for δb_1, δb_2 and δb_3 assuming that $\delta b_4 = 0$. Again the relevant rate coefficients, trapping coefficients and transition probabilities can be found in appendix A.

In our derivation of δb_q, we will assume that the population of the excited levels (q>1) is mainly caused by (de)excitation and ionization, and accordingly diffusion effects will be neglected. For the ground level this assumption is not valid, and so we will treat δb_1 separately.

2.2.1 *Non-equilibrium of excited states (with exception of the ground state)*

When diffusion is neglected in (2.9) we obtain for the stationary state:

$$\delta b_q = \frac{n_e \sum\limits_{\substack{i=1 \\ i\neq q}}^{N} \delta b_i k_{qi} + R^{(2)}_{q+} k^{(2)}_{+q} \Lambda^{(2)}_{+q} - \sum\limits_{p=1}^{q-1} A_{qp}\Lambda_{qp} + \sum\limits_{r=q+1}^{N} (1+\delta b_r) R_{rq} A_{rq} \Lambda_{rq}}{n_e K_q - \sum\limits_{p=1}^{q-1} A_{qp}\Lambda_{qp}} \qquad (2.11)$$

$$\text{where } K_q \equiv \sum_{\substack{i=1 \\ i\neq q}}^{N} k_{qi} + k_{q+} \qquad (2.11a)$$

With the assumption $\delta b_4 = 0$, the following relation results between the levels q=1, q=2 and q=3.

$$\delta b_2 \simeq \{\delta b_1 k_{21} + \delta b_3 k_{23} + \frac{1}{n_e} [R^{(2)}_{2+} k^{(2)}_{+2} - A_{21}\Lambda_{21} + (1+\delta b_3) . R_{32} A_{32}]\}/K_2 \text{ and} \qquad (2.12)$$

$$\delta b_3 \simeq \{\delta b_1 k_{31} + \delta b_2 k_{32} + \frac{1}{n_e} [R^{(2)}_{3+} k^{(2)}_{+3} - A_{32} + R_{43} A_{43}]\}/K_3 \text{ and} \qquad (2.13)$$

In (2.12) and (2.13) we have made the following simplifications:

$A_{21}\Lambda_{21} << K_2 n_e$	This is correct by more than three orders of magnitude for $n_e \gtrsim 10^{22}\ m^{-3}$
$\Lambda^{(2)}_{+2}, \Lambda^{(2)}_{+3} = 1$	Only recombination radiation to the ground state is partially trapped.
$\Lambda_{32} = \Lambda_{43} = 1$	Line radiation is also not trapped. For several of the 3-2 transitions the optical depth may approach 1. So the value for Λ_{32} will be slightly smaller than 1.

We note that the transition 3-1 is forbidden, so $A_{31}\Lambda_{31} = 0$.

From (2.12) and (2.13) δb_2 and δb_3 can be expressed in δb_1:

$$\delta b_2 = \frac{k_{21}K_3 + k_{31}[k_{23} + \frac{\gamma}{n_e}]}{K_2K_3 - k_{32}[k_{23} + \frac{\gamma}{n_e}]}\,\delta b_1 + \frac{K_3\frac{\alpha}{n_e} + [k_{23} + \frac{\gamma}{n_e}]\frac{\beta}{n_e}}{K_2K_3 - k_{32}[k_{23} + \frac{\gamma}{n_e}]} \qquad (2.14a)$$

and

$$\delta b_3 = \frac{k_{23}k_{21} + k_{31}K_2}{K_2K_3 - k_{32}[k_{23} + \frac{\gamma}{n_e}]}\,\delta b_1 + \frac{k_{32}\frac{\alpha}{2n_e} + K_2\frac{\beta}{2n_e}}{K_2K_3 - k_{32}[k_{23} + \frac{\gamma}{n_e}]} \qquad (2.15)$$

where the notations

$$\alpha = (R^{(2)}_{2+}k^{(2)}_{+2} - A_{21}\Lambda_{21} + R_{32}A_{32}) \qquad (2.16a)$$

$$\beta = (R^{(2)}_{3+}k^{(2)}_{+3} - A_{32} + R_{43}A_{43}) \qquad (2.16b)$$

and $\gamma = R_{32}A_{32}$ (2.16c)

have been used for the radiative contributions.

In table 2.2 we give typical values for the relevant collision cross-sections and radiative contributions (we refer to fig. A.7 - A.9 and 2.3a - 2.3f for more precise information).

So the following relations result from (2.14) - (2.16)

$$\alpha \simeq R_{32}A_{32} \simeq 2.10^7 s^{-1},\ \beta \simeq (R_{43}A_{43} - A_{32}) \simeq -3.10^7 s^{-1}$$

and with $\gamma/n_e \ll k_{23}$ for $n_e > 5.10^{20}\ m^{-3}$

$$\delta b_2 \simeq \frac{\frac{k_{21}}{k_{23}}k_{34} + k_{31}}{k_{34} - k_{32}} + \frac{\alpha + \beta}{n_e(k_{34} - k_{32})} \simeq 2.10^{-3}\delta b_1 - \frac{5.10^{19}}{n_e} \qquad (2.14a)$$

$$\delta b_3 \simeq \frac{k_{21} + 2k_{31}}{2k_{34} - k_{23}} + \frac{\alpha + 2\beta}{n_e(2k_{34} - k_{23})} \simeq 10^{-3}\delta b_1 - \frac{10^{20}}{n_e} \qquad (2.15a)$$

Table 2.2

Numerical values of the functions of equation (2.14) - (2.16) for $\hat{T}_e = 1eV$.

Radiative contributions $[s^{-1}]$	Collision cross sections $[m^3 s^{-1}]$
$R^{(2)}_{2+}k^{(2)}_{+2} \simeq 2.10^6$	$k_{21} \simeq 2.10^{-16}$
$R_{32}A_{32} \simeq 2.10^7$	$k_{31} \simeq 2.10^{-16}$
$A_{21}\Lambda_{21} \simeq 8.10^5$	$k_{23} \simeq 3.10^{-13}$
$R^{(2)}_{3+}k^{(2)}_{+3} \simeq 3.10^5$	$k_{32} \simeq 1.5\ 10^{-13}$
$R_{43}A_{43} \simeq 8.10^6$	$k_{34} \simeq 4.10^{-13}$
$A_{32} \simeq 4.10^7$	$K_3 \simeq k_{34}$, $K_2 \simeq k_{23}$

From these equations it appears that non-equilibrium of the levels q=2 (4s group) and q=3 (4p group) are caused mainly by the competition between overpopulation due to collisional (de)excitation and underpopulation due to radiative losses.

For the parameter range of interest ($5.10^{22} < n_e < 2\ 10^{23} m^{-3}$) underpopulation of level q=2 is only to be expected for high values of T_e and n_e, where δb_1 will be small (near - LTE situation). In all other situations of interest, δb_2 will remain positive, and level q=2 will be slightly overpopulated. This overpopulation is very small, a few parts in a thousand, and is of negligible influence on our measurements.

The level q=3 (4p group) is underpopulated, mainly due to the strong radiative decay to the slightly overpopulated level q=2.

We conclude that, indeed, PLTE is justified provided that δb_1 remains small enough. A second conclusion is that a slight underestimation of the temperature will result from our measurements (see chapter 3) if we neglect the non-equilibrium of the levels with q=2 and q=3.

2.2.2 *Non-equilibrium of the ground state level*

In this case, diffusion cannot be neglected. For the stationary state, we obtain from (2.9) and (2.10), for the 4-level model:

$$\delta b_1 = [R^{(2)}_{1+}\, k^{(2)}_{+1}\, \Lambda^{(2)}_{+1} + R_{21}A_{21}\Lambda_{21} + R_{41}A_{41}\Lambda_{41} - \frac{\mathrm{div}(n_1\underline{w}_1)}{n_{1,saha}}]/n_e K_1 \quad (2.17)$$

We will discuss the radiative terms and the diffusion term consecutively.

<u>The radiative terms in (2.17):</u>

From the numerical values in table A.2 and figure 2.3 we see that for $\frac{\Lambda_{21}}{\Lambda^{(2)}_{+1}} < 0.1$ and $\frac{\Lambda_{41}}{\Lambda^{(2)}_{+1}} < 0.1$, the recombination radiation term is the dominant term of the radiative contributions. The trapping coefficient for recombination radiation will appear to be in the range 0.2-0.6. Since the trapping coefficient for resonance lines are of the order of 10^{-3}-10^{-2} we can neglect the contribution of resonance lines with respect to that of the recombination radiation.

For our conditions the calculation of the reabsorption of recombination radiation to the ground state imposes a serious problem. The optical depth $\bar{\kappa}\bar{R}$ is of the order of one, so that absorption should be taken into account. On the other hand $\bar{\kappa}\bar{R}$ is not large enough, and so a local approximation by a trapping coefficient is even not sufficient.
To cope with this problem we will use a calculation by Hermann [HER68] who analysed a 5 mm Ar arc at atmospheric pressure. Under the assumption of LTE, and neglecting the effect of continuum radiation with wavelength above the free-bound edge, he obtained the results which are shown in fig. A.5. (cf. appendix A).

As can be observed from this figure, the radiation loss from the plasma at the axis is slightly reduced as expected. There we can use the local approximation with the values from Hermann for $\Lambda^{(2)}_{+1}$. In the outer layers of the plasma radiation which is generated closer to the plasma axis is reabsorbed. There even photo ionization may be larger than the local recombination and so a negative value of $R^{(2)}_{1+}\kappa^{(2)}_{+1}\Lambda^{(2)}_{+1}$ would result. As will appear in chapter V, diffusion is far more important in the outer regions, so that we do not expect serious consequences from this reabsorption effect and we can use the local approximation throughout the plasma.
For the temperature range of interest, $\Lambda^{(2)}_{+1}$ varies between 0.2 and 0.6. In figure 2.4 the magnitude of the three radiative terms of (2.17) is shown as a function of temperature. Here we have used Hermann's values for $\Lambda^{(2)}_{+1}$.

The diffusion term in (2.17):

We will express the contribution of diffusion to δb_1 in terms of n_e and T_e by using the relations

$$n_1\underline{w}_1 = -n_e\underline{w}_e = -n_e\underline{w}_A = \frac{D_A}{kT_1}\,\mathrm{grad}(p_e+p_i) \qquad (2.18)$$

where $\underline{w}_e$ is the diffusion velocity of the electrons, $\underline{w}_A$ is the ambipolar velocity, p_e and p_i are the partial pressures of electrons and ions and D_A the ambipolar diffusion coefficient, is given by [DEV65]:

$$D_A \approx 2D_{i1} = 2\cdot\frac{3kT_1}{8(n_1+n_+)\Omega_{i1}^{(1,1)}m_1} \qquad [\mathrm{m}^2\mathrm{s}^{-1}] \qquad (2.19)$$

Here m_1 is the heavy particle mass, and $\Omega_{i1}^{(1,1)}$ is a first approximation to the ion-atom collision integral, which can be calculated from:

$$\Omega_{i1}^{(1,1)} \approx 2.84\ 10^{-17}\ T_1^{0.36} \qquad [\mathrm{m}^3\ \mathrm{s}^{-1}] \qquad (2.20)$$

We will assume that $T_1 \approx T_e$ in our plasma. This assumption is justified for the majority of conditions that have been investigated, as in most cases the electrical field strength is quite low, and the electron-ion-atom collision frequencies are relatively high. In addition experimental determination of $T_e - T_1$ by Gurevich et al. [GUR63] have demonstrated that $T_1 \doteq T_e$ for $T_e > 7500$K.

As a typical result of their measurements we recall:

$T_e - T_1 \approx 120$K for $T_e \approx 7500$K at atmospheric pressure.

So T_1 in (2.20) and (2.19) can be replaced by T_e, and we obtain for D_A

$$D_A \approx 2\cdot\frac{2.76\ 10^{18}}{(n_1+n_e)}\cdot T_e^{0.64} \qquad (2.19a)$$

Evaluation of the term div$(n_1\underline{w}_1)$ is only possible when radial profiles of $n_e(r)$, $n_1(r)$, $p_e(r)$ and $T_e(r)$ are available. We will postpone such calculations to chapter 5 where results of the radial profile measurement will be discussed. Here we will suffice with an estimation of the order of magnitude of the contributions to δb_1 for a 40A arc, where the effect of diffusion is expected to be the largest.

We will assume LTE-equilibrium, and we will anticipate the results of chapter 5 by using the measured values of $T_e(r=0.4R)$, and of the temperature and density gradients at $r=0.4R$, where the diffusion velocity appears to be maximal. We find: $\frac{1}{n_{1,saha}} \nabla \cdot n_1\underline{w}_1 \simeq 700\ s^{-1}$ for the diffusion term in (2.17) and $R^{(2)}_{1+}\ k^{(2)}_{+1}\ \Lambda^{(2)}_{+1} \simeq 300\ s^{-1}$, $R_{21}A_{21}\Lambda_{21} \simeq 50\ s^{-1}$ and $R_{41}A_{41}\Lambda_{41} \simeq 8s^{-1}$ for the different contributions due to radiative transitions.

With $n_{e,\ LTE}\ K_1 \simeq 2300\ s^{-1}$ we obtain from this estimation: $\delta b_1 \simeq 0.46$

Our measurements at this current yield $\delta b_{1m} \simeq 0.77$ which is larger than the calculated value of δb_1 by a factor 1.7.

If instead, the PLTE value of n_e was used in n_eK_1, we would have obtained $n_{e,PLTE}\ K_1 \simeq 1800$ s and $\delta b_1 \simeq 0.59$ and the ratio $\delta b_{1m}/\delta b_1 \simeq 1.3$.

So, indeed we obtain a deviation from the equilibrium population of the ground level. The influence of diffusion is about 2.5 times the influence of the recombination radiation at a radial position where the diffusion is maximum. This influence will become smaller for larger values of the current as the radial profiles will become flatter. Also on the axis of the discharge this influence is smaller.

We will discuss the overpopulation of δb_1, δb_2 and δb_3 later in chapter 5 where some more detailed calculations from the measured profiles will be given.

CHAPTER III, PRINCIPLES OF MEASUREMENT

3.1 Introduction

In this chapter we describe the plasma diagnostic methods that were used to obtain information about the plasma parameters.

In our measurements we determine the source function [DRA73] of a transition in the argon neutral spectrum to obtain information about the electron temperature in the plasma.

The considered transitions are optically thick, i.e. $\kappa_L(\lambda)\cdot\ell>1$, but not to such extent that the methods proposed by Drawin in [DRA73] (which are mainly intended for resonance lines with $\kappa_L(\lambda)\cdot\ell>>1$) can be used.

Here we determine the source function directly by measuring the emission and absorption coefficients of the considered transitions.

Our method resembles the one used by Bober and Tankin [BOB70] in their investigation of equilibrium of an argon plasma by measurement of the transition probability of an atom line at various pressures.

An important difference is that we observe the plasma end-on, instead of side-on as in their experiments, eliminating the need for Abel inversion of the measured profiles (which introduces inaccuracies in the measured radial profiles).

From the source function the electron temperature is calculated, and from the total line intensity together with the obtained value of the electron temperature, the electron density is determined.

Here the assumption of Partial Local Thermal Equilibrium is needed.

These methods are described in section 3.2

We also describe an interferometric method for an independent determination of the electron density.

Interferometric methods have the advantage of being independent of an assumption of (P)LTE.

Several methods for the determination of the electron density by interferometry have been described in the literature [BAU75, BAK69].

The method of Baum et al.[BAU75] is based on an interferometer of the Mach-Zehnder type with a HeNe laser as the light source. Their measurements were performed side-on, yielding radial profiles for the electron density, but again after Abel-inversion.

We used an interferometer of the coupled-cavity type as described by Ashby and Jephcott [ASH63] and used by Bakeyev [BAK69].

The advantage of this type of interferometer is the possibility for performing end-on measurements, and in addition in our case the possibility of probing the same plasma volume as with the spectroscopic set-up.

The interferometric set-up is described in section 3.3.

3.2 Spectroscopic methods

3.2.1 The equation of radiative transfer

The cascade arc plasma can be considered a cylindrically symmetric radiator of radius R and length l. The symmetry axis is taken as the z-direction. We will make the following assumptions:

1. The plasma is homogeneous in the z-direction, i.e. $\varepsilon_\lambda, \kappa(\lambda)$, T_e and n_e are only functions of the radial coordinate r.
2. There is no emission and absorption of radiation by the plasma, outside the region $0 \leq r \leq R$ and $0 \leq z \leq l$.

The plasma is observed end-on (parallel to the z-axis), as sketched in fig. 3.1.

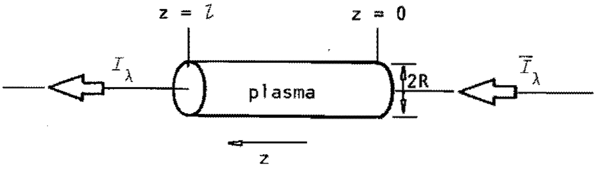

Fig. 3.1
Illustration of the geometry for the derivation of equations (3.2) and (3.3)

We consider the 1 dimensional equation of radiative transfer.

The spectral intensity passing through a volume element between z and z+dz, at radial position r, increases due to the spectral emission ($\varepsilon_\lambda(r)dz$) and decreases due to the spectral absorption ($\kappa(\lambda)I_\lambda(r,z)dz$). The change of I_λ (r,z) as a function of z is given by:

$$\frac{\partial I_\lambda(r,z)}{\partial z} = \varepsilon_\lambda(r) - \kappa(\lambda,r)\, I_\lambda(r,z) \tag{3.1}$$

Integration of equation (3.1) over the length of the cilinder ($0 \leq z \leq l$) with the boundary condition $I_\lambda(r,0) = 0$, yields:

$$I_\lambda(r,l) = \frac{\varepsilon_\lambda(r)}{\kappa(\lambda,r)}[1-\exp(-\kappa(\lambda,r)l)] \tag{3.2}$$

With an additional radiative flux of spectral intensity $\bar{I}_\lambda$ in the direction of the plasma at z=0 (cf. fig. 3.1), the boundary condition at z=0 becomes $I_\lambda(r,0) = \bar{I}_\lambda$ and from (3.1) results:

$$I_\lambda(r,l) = \frac{\varepsilon_\lambda(r)}{\kappa(\lambda,r)}[1-\exp(-\kappa(\lambda,r)l)] + \bar{I}_\lambda(r)\cdot\exp(-\kappa(\lambda,r)l) \tag{3.3}$$

Note that the emission and absorption coefficients in equations (3.1) - (3.3) are a combination of line (L) and continuum (C) contributions:

$$\varepsilon_\lambda = \varepsilon_{\lambda,L} + \varepsilon_{\lambda,C} \qquad \text{and} \tag{3.4a}$$

$$\kappa(\lambda) = \kappa_L(\lambda) + \kappa_C(\lambda) \tag{3.4b}$$

Consequently, also the intensities contain line and continuum contributions (cf. appendix B).

3.2.2 *Evaluation of the source function*

The ratio $\varepsilon_\lambda/\kappa(\lambda)$ is generally known [DRA73] as the source function, which we will denote by the symbol S_λ. Under equilibrium conditions S_λ is equal to the spectral intensity of a blackbody radiator, and follows from Kirchoff's law: *

$$S_\lambda = \frac{\varepsilon_\lambda}{\kappa(\lambda)} = \frac{2hc^2}{\lambda^5}\frac{1}{\exp(\frac{hc}{\lambda kT})-1} \tag{3.5}$$

---

* *Note: In this section we will assume that the refractive index of the plasma is equal to one.*

For a situation in which PLTE with $T_{gas} = T_e$ holds, the temperature T in equation (3.5) is equal to the electron temperature T_e. We will use this equation to obtain values for T_e from intensity measurements.

First we will describe the evaluation of S_λ, and in section 3.2.3 the determination of T_e will be delt with.

From (3.2) follows

$$S_\lambda(r) = \frac{I_\lambda(r,l)}{1-\exp(-\kappa(\lambda,r)l)} \tag{3.6}$$

We observe that measurement of $I_\lambda(r,l)$ alone is not sufficient to determine $S_\lambda(r)$. We need an additional measurement of the absorption coefficient $\kappa(\lambda,r)$. To this end the following method is used (please refer to fig. 3.2).

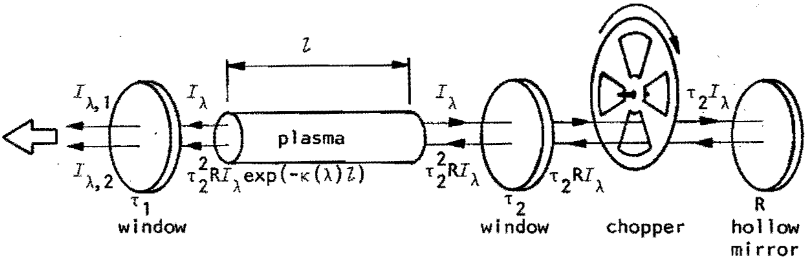

Fig. 3.2
Principle of measurement for the determination of the source function.
Note that the light paths have been separated exagerately for clearness.
In reality they coincide.

The plasma in fig. 3.2 is observed end-on. The position of the concave spherical mirror is such that the observed plasma cilinder is imaged onto itself. With the chopper we can create each of the two conditions:

1. With the chopper closed no intensity is radiated towards the plasma.
2. When the chopper is open a well-known intensity is radiated towards the plasma.

Taking into account the finite transmissivity τ_1 and τ_2 of the end windows of the plasma vessel, and the finite reflectivity R of the hollow mirror, we obtain (cf. equations (3.2), (3.3) and figure 3.2):

Chopper closed:

$$I_{\lambda,1}(r) = \tau_1 I_\lambda(r,l) \tag{3.7}$$

Chopper opened:

$$I_{\lambda,2}(r) = I_{\lambda,1}(r) \cdot [1 + \tau^2 R \exp(-\kappa(\lambda,r) l)] \ , \tag{3.8}$$

with $\tau = \tau_2$.

Here we have used the fact that the same spectral intensity is radiated at each end of the plasma, which is in accordance with our assumption of homogeneity (in the z-direction).

Before being able to solve equations (3.7) and (3.8) for $I_\lambda(r,l)$ and $\kappa(\lambda,r)$, which is our aim as we want to calculate $S_\lambda(r)$ using equation (3.6), values for τ_1 and $\tau^2 R$ must be supplied.

Both quantities are functions of the wavelength, and their value may change with time.

Determination of τ_1 is straightforward: during the calibration procedure (cf. section 4.2 and 3.2) the window can simply be placed in the light path. The calibration factor will then include the value of τ_1.

For $\tau^2 R$ the following procedure can be used:

Defining the quantity v_λ by

$$v_\lambda \equiv \frac{I_{\lambda,2} - I_{\lambda,1}}{I_{\lambda,1}} \tag{3.9}$$

We obtain from (3.8)

$$v_\lambda = \tau^2 R \exp(-\kappa(\lambda) \cdot l) \tag{3.10}$$

In the continuum $\kappa(\lambda) = \kappa_L(\lambda) + \kappa_C(\lambda) \approx \kappa_C(\lambda)$ and from (3.10)

$$v_{\lambda,C} \approx \tau^2 R \exp(-\kappa_C(\lambda) l) \qquad (3.10a)$$

Usually $\kappa_C(\lambda) l$ is small, and is negligible at low values of the current ($I<25A$; 5 mm diameter arc). In the limit to low current must hold:

$$\lim_{I \to 0} v_{\lambda,C} = \tau^2 R \qquad (3.10b)$$

The change of $v_{\lambda,C}$ with current is shown in figure 3.3

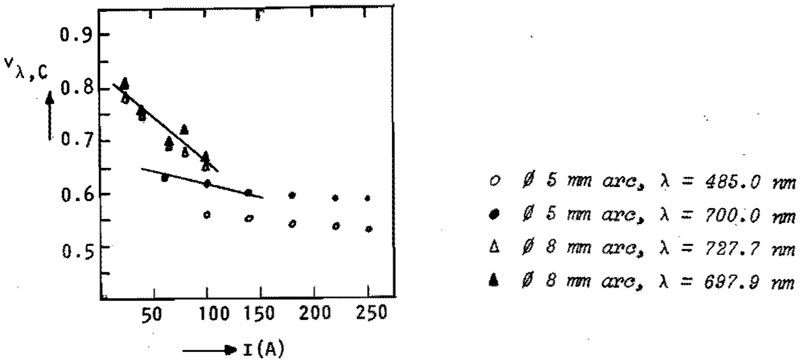

Fig. 3.3
The quantity $v_{\lambda,C}$ (equation 3.10a) as a function of the arc current and for two values of the wavelength.

In this figure some results for two different arcs (ϕ5 mm and ϕ8 mm) are collected. For each arc $v_{\lambda,C}$ is shown for two different values of the wavelength. Usually these wavelength values are taken in the vicinity of spectral lines that will subsequently be investigated. The expected behaviour is evident, while in addition the dependence of $\tau^2 R$ on λ is also apparent. For the ϕ8mm arc quartz windows were used and so a higher value of $\tau^2 R$ is obtained.

Note, that from this figure also values of $\kappa_C l$ can be obtained (after the extrapolation to low currents which gives $\tau^2 R$).

3.2.2.1 *Accuracy of the determination of the source function*

The accuracy of the obtained values of S_λ is determined by:

1. The accuracy of the absolute calibration of the spectral intensity. The influence of the absolute calibration on S_λ is straightforward (equation (3.6)): $\Delta S_\lambda/S_\lambda = \Delta C/C$; $\Delta C/C$ is the relative error in the calibration factor. We will return to this source of error in section 3.2.3, where its influence on the measured plasma parameters will be discussed in more detail.
2. The accuracy with which $\tau^2 R$ and $I_\lambda(r)$ can be determined. To obtain an estimate of $\Delta S_\lambda/S_\lambda$ in this case we will write S_λ in terms of $I_{\lambda,1}$ and $I_{\lambda,2}$, using (3.6) and (3.8):

$$S_\lambda = \frac{\tau^2 R\, I^2_{\lambda,1}}{(\tau^2 R+1) I_{\lambda,1} - I_{\lambda,2}} \tag{3.11}$$

(We have set $\tau_1=1$, but this is of no influence on the conclusions).

From (3.11) we obtain for the relative error in S_λ:

$$\frac{\Delta S}{S} = \frac{\left(\frac{I_1}{I_2} - 1\right)\cdot\frac{\Delta T}{T} + \left[(T+1)\,\frac{I_1}{I_2} - 1\right]\,\frac{\Delta I_1}{I_1} + \frac{\Delta I_2}{I_2}}{(T+1)\,\frac{I_1}{I_2} - 1} \tag{3.12}$$

Here we have used the notation $T = \tau^2 R$, and dropped the subscript λ for convenience.

In figure 3.4 the relative error in S_λ is plotted versus the parameter $\alpha \equiv (T+1)\cdot I_1/I_2$ for the following conditions:

$T \equiv \tau^2 R = 0.6$, $\Delta I_1/I_1 = \Delta I_2/I_2 = 2\%$ and $\Delta T/T = 2\%$ (curve A), 5% (curve B)

(The calibration error has not been included here).

As expected, the uncertainty in S_λ increases for $I_1/I_2 \rightarrow (T+1)^{-1}$

Also the influence of the accuracy of T on S_λ is apparent.

Note that we have used a worst-case estimate for the uncertainty in the relative intensity measurements. In practice the relative error in

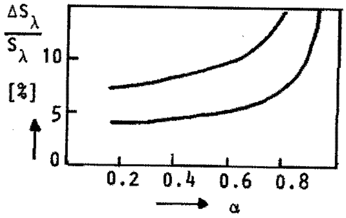

Fig. 3.4
Dependence of the relative error in the source function on $\alpha \equiv (\tau^2 R + 1).I_{\lambda,1}/I_{\lambda,2}$ *for the conditions:* $\tau^2 R = 0.6$, $\Delta I_{\lambda,1}/I_{\lambda,1} = \Delta I_{\lambda,2}/I_{\lambda,2} = 2\%$ *and* $\Delta\tau^2 R/(\tau^2 R) = 2\%$ *(curve A) and 5% (curve B)*

$I_{\lambda,1}$ (or $I_{\lambda,2}$) remains below 0.5% especially when line intensities are measured.

In our measurements, the source function is determined in a wavelength interval in the argon spectrum that includes a spectral line and its adjacent continuum. The scanning is performed by an automatically controlled monochromator, and the signals are measured with a photomultiplier as will be described in chapter 4.

Each time the monochromator is positioned at a different wavelength value. The intensities $I_{\lambda,1}$ and $I_{\lambda,2}$ are measured after the chopper (cf. fig. 3.2) has been closed or opened. Then the monochromator is positioned at the next wavelength value. In this way the wavelength interval is scanned in a large number of equally spaced wavelength steps, and complete intensity profiles for $I_{\lambda,1}$ and $I_{\lambda,2}$ are obtained. In section 4.2 this procedure is described in more detail.

Figure 3.5 shows a typical scan of the profiles of $I_{\lambda,1}$, $I_{\lambda,2}$ and in addition a reference signal that is included in the measurements and from which the apparatus profile of the monochromator can be obtained.

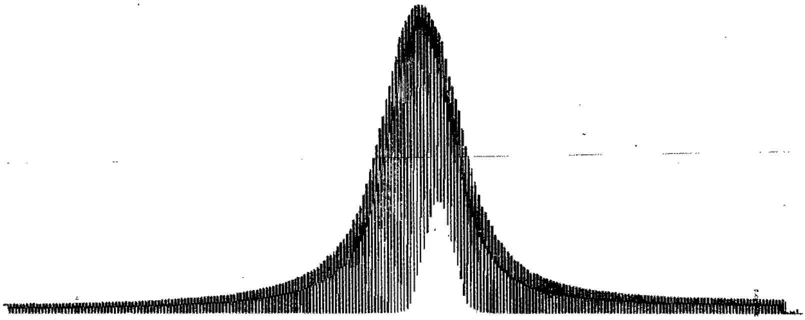

Fig. 3.5
Scan of the profiles of $I_{\lambda,1}$, $I_{\lambda,2}$ *and the reference signal.*
Ø 8 mm argon arc, $I = 80A$, $\lambda_0 = 696.5$ *nm*
The scanning in this figure is from right to left (696.0 nm → 697.1 nm)

As this additional line is produced by a low pressure, low current argon arc discharge (low values of the electron density) the line width of the measured profile can be used as the apparatus profile of the monochromator. Furthermore as the line profiles from the low pressure discharge are not shifted (again due to the low value of the electron density) they can be used as wavelength references for the lines from the atmospheric pressure arc discharge.

The measuring set-up and techniques are described in chapter 4.

The shape of the measured intensity profiles of $I_{\lambda,1}$ and $I_{\lambda,2}$ which we shall denote by $\bar{I}_{\lambda,1}$ and $\bar{I}_{\lambda,2}$, is determined by:

1. The profile of $\kappa_L(\lambda)$.

The line profile of $\kappa_L(\lambda)$ is determined by the combined effect of Stark and Doppler broadening in the plasma [GRI64, SOB72]. The Doppler contribution (Gaussian shape) to the total profile width is small compared with the contribution due to the Stark effect (Lorentzian shape). At λ= 700 nm and T_e = 1eV: Doppler width ≈ 8.10^{-3} nm and Stark width ≈ 5.10^{-2} nm. The line profile of $\kappa(\lambda)$ is a Voigt profile with a small value of the ratio Gaussian width/Lorentzian width. Note: we will not neglect the contribution of the Doppler broadening in the derivation of the plasma parameters (next section).

2. Self-absorption

Because the line absorption is larger at the line center than in the line-wings, the line profile of $I_{\lambda,1}$ and $I_{\lambda,2}$ is different from that of $\kappa(\lambda)$. This is expressed by the factor $1-\exp(-\kappa(\lambda)l)$ in equations (3.2) and (3.8).

3. Convolution with the apparatus profile of the monochromator.

(Apparatus width ≈ 2.10^{-2}nm depending on the setting of the entrance and exit slits of the monochromator). This broadening effect is constant during a measurement, but becomes an important contribution to profiles that are measured at low values of the arc current.

Measurement of the line-profiles of $I_{\lambda,1}$ and $I_{\lambda,2}$ allow us to determine besides S_λ (and thus T_e), also other plasma parameters, e.g. the electron density.

The accuracy in the determination of the plasma parameters is not only improved because of the better statistics (more values), but also because:

1. The a priori knowledge of the shape of the $\kappa_L(\lambda)$ profile, which must be a Voigt profile. As the parameters that determine the Voigt shape follow directly from the plasma parameters, additional criteria for the latter can be formulated.

2. The accuracy in the determination of τ^2R can be improved with the help of the relation $S_{\lambda,C} = S_{\lambda,C}$ ($S_{\lambda,C} \equiv \varepsilon_{\lambda,C}/\kappa_C(\lambda)$ and $S_{\lambda,L} \equiv \varepsilon_{\lambda,L}/\kappa_L(\lambda)$. This relation is valid in PLTE throughout the profile of the observed line, provided that the considered wavelength interval is not too large; cf. equation (3.5). In our measurements the wavelength range was about 4 nm, so this assumption is valid.

$S_{\lambda,L}$ can be determined with a higher precision than $S_{\lambda,C}$. In the continuum $I_{\lambda,C} \simeq \varepsilon_{\lambda,C} \cdot l$ as $\kappa_C(\lambda) \cdot l$ is negligible in (3.2), and so the continuum absorption can be obtained from $\kappa_C(\lambda) = S_{\lambda,L} \cdot \varepsilon_{\lambda,C}$. This value of $\kappa_C(\lambda)$ can be inserted directly in (3.10a) to obtain τ^2R without extrapolation.

3.2.3 Determination of the plasma parameters

The plasma parameters of interest are evaluated as follows. The electron temperature, T_e, is obtained from equation (3.5):

$$T_e = \beta \frac{1}{\ln(1 + \frac{\alpha}{S_\lambda})} \qquad (3.13)$$

with $\beta = \frac{hc}{\lambda k}$ and $\alpha = \frac{2hc^2}{\lambda^5}$

- The electron density, n_e, follows from $\kappa_L(\lambda)$ after integration over the considered wavelength interval.
  With equation (b3b) from appendix B, the lower level density, n_1, of the considered transition can be determined, and with the assumption of PLTE n_e is obtained from equation (2.3).

- The density of ground state atoms n_1 is determined from the pressure relation

$$p = (2n_e+n_1)kT_e \tag{3.14}$$

As we also want to determine δb_1 (cf. chapter 2) we need the Saha value of the neutral density $n_{1,saha}$. This value follows directly from equation (2.3) with the experimental value of n_e and T_e.

3.2.3.1 *Approximation procedures for the plasma parameters*

In all these calculations the influence of the apparatus profile has to be accounted for.

We have used a numerical procedure in which values of the relevant plasma parameters were approximated iteratively in such a way that intensity distributions $I_{\lambda,1}$ and $I_{\lambda,2}$ were obtained that would fit to the measured intensity distributions $\bar{I}_{\lambda,1}$ and $\bar{I}_{\lambda,2}$.

In the numerical procedure theoretical representations for $I_{\lambda,1}$ and $I_{\lambda,2}$ are obtained as follows:

First an approximation for $\kappa(\lambda)\cdot l$ is calculated. From trial values of T_e and n_e the parameters that determine $\kappa(\lambda)\cdot l$ are derived:

1. The Lorentzian component of the profile width of $\kappa_L(\lambda)$ follows from n_e together with an approximation for the Stark parameter.
2. The Gaussian component to $\kappa_L(\lambda)$ is the Doppler width, which can be calculated with T_e.
3. The line center is a parameter in the procedure.
4. The area of $\kappa_L(\lambda)$ follows from equation (b3b), where n_1 is calculated from n_e, using the Saha relation (2.3) (with q=1).
5. $\kappa_C(\lambda)l$ is obtained from equation (b5) with the trial values of T_e and n_e and an approximation for ξ_{fb}. The ksi-factor for free-free emission, which is almost constant is taken from litterature [VEN71]

The line profile of $\kappa_L(\lambda)l$ is a Voigt function which can be calculated from the real part of the complex error function [ABR64], with the algorithm developed by Gautschi [GAU70].

Afterwards the continuum contribution to $\kappa(\lambda)l$ is added.

With $\kappa(\lambda)l$ and the value of T_e, $I_{\lambda,1}$ and $I_{\lambda,2}$ follow from equation (3.5), (3.2) and (3.8).

Now an approximation for the measured profiles is obtained from:

$$\bar{I}_{\lambda,1} = I_{\lambda,1} * A(\lambda) \tag{3.15a}$$

$$\bar{I}_{\lambda,2} = I_{\lambda,2} * A(\lambda) \tag{3.15b}$$

with the definition of convolution:

$$f*a = \int_{-\infty}^{\infty} f(\lambda')a(\lambda-\lambda')d\lambda' \tag{3.16}$$

The convolution integral was calculated from a Gauss-Hermite approximation for the integral in (3.16):

$$\int_{-\infty}^{+\infty} h(x)dx \approx \sum_{i=1}^{n} w_i \, e^{x_i^2} g(x_i) \qquad (3.17)$$

The abcissa's $\pm x_i$ and the weight factors $w_i \, e^{x_i^2}$ can be found in [SAL52]. We used the approximation with n=9.

The fit to the measured profiles was performed with a least-squares minimalisation procedure [EIL75] in which the Marquardt algorithm was used [MAR63].

In this procedure the calculated intensity distributions $\bar{\bar{I}}_{\lambda,1}$ and $\bar{\bar{I}}_{\lambda,2}$ are compared with the measured distributions $\bar{\bar{I}}_{\lambda,1}^{m}$ and $\bar{\bar{I}}_{\lambda,2}^{m}$ for each wavelength value, and the function:

$$\left(\left(\sum_{i=1}^{n} (\bar{\bar{I}}_{\lambda_i,1} - \bar{\bar{I}}_{\lambda_i,1}^{m})^2\right)^2 + \left(\sum_{i=1}^{n} (\bar{\bar{I}}_{\lambda_i,2} - \bar{\bar{I}}_{\lambda_i,2}^{m})^2\right)^2\right)^{\frac{1}{2}} \qquad (3.18)$$

is minimized.

Figure 3.6 shows the structure of the numerical procedure. In figure 3.7 an example of the result of a fit to the measured profiles is shown while in fig. 3.8 the residuals at the end of the minimalisation process have been plotted as a function of wavelength. These residuals give an impression of the quality of the approximation.

3.2.3.2 Accuracy of the plasma parameters

An important factor determing the accuracy with which the various parameters are evaluated is the absolute calibration of the measured intensity.

For the intensity calibration we used a tungsten ribbon lamp (Philips model T234 type W2KGV22i). This lamp was calibrated at the University of Utrecht against a blackbody radiator. At a current setting of I = 12.736A the emissivity of this lamp can be found from the tables given by De Vos [VOS53] for a strip temperature of 2600K. The relative accuracy of the calibration procedure is about 3%.

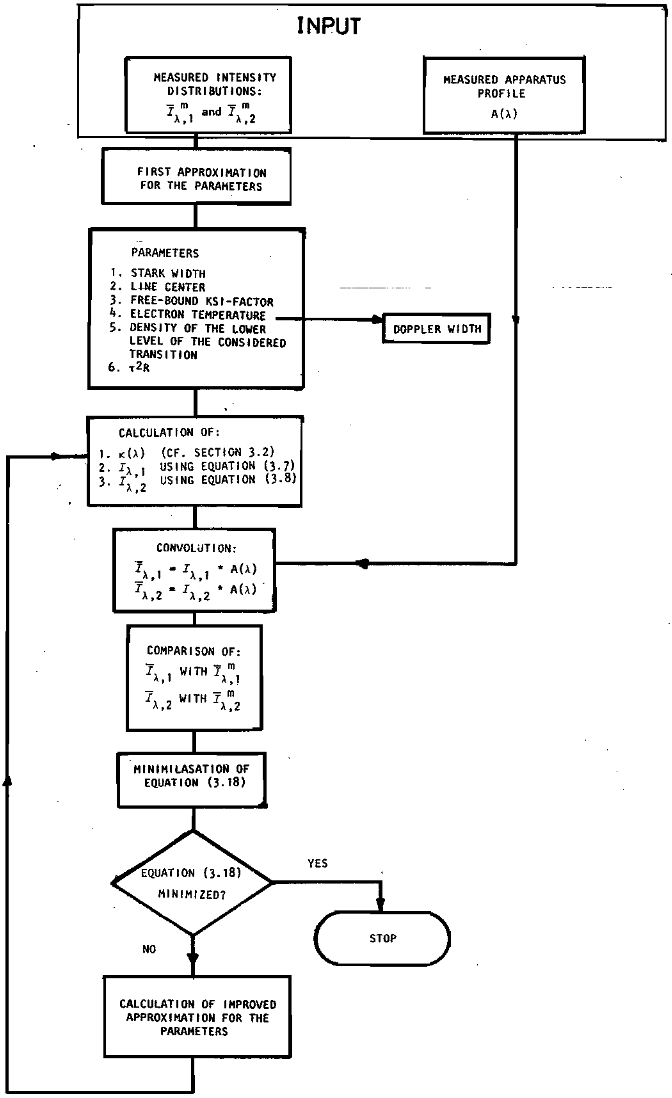

Fig. 3.6
Flow-chart of the numerical method for the approximation procedure.

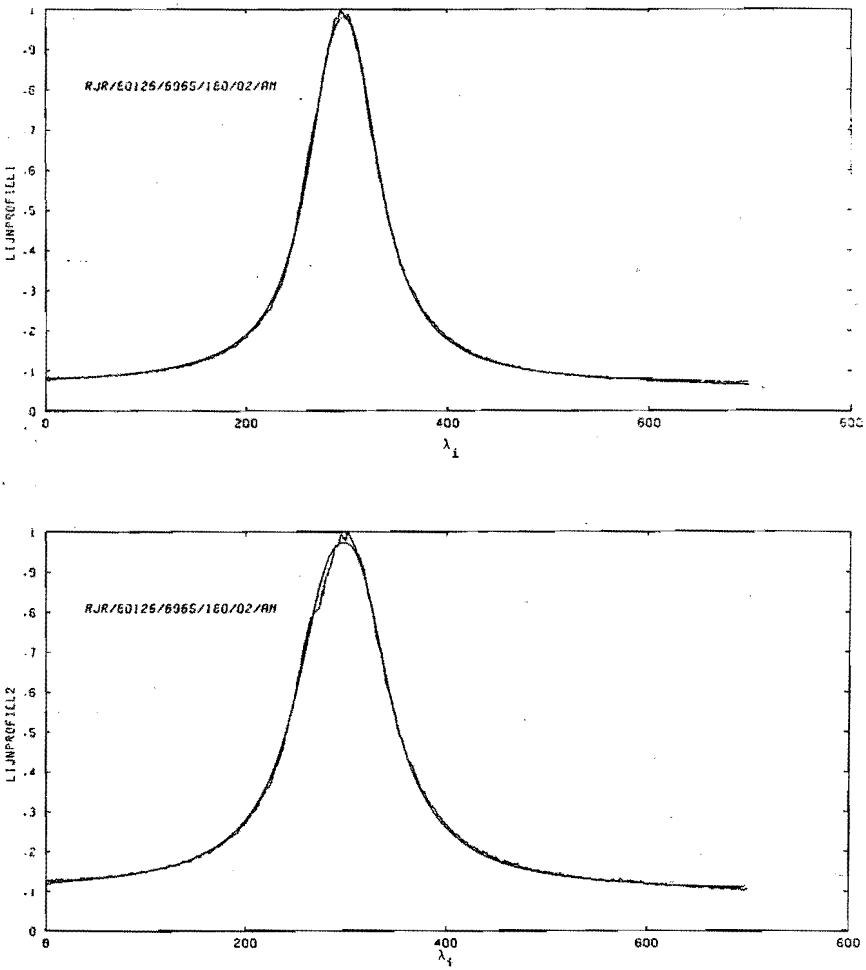

Fig. 3.7

Example of a result of the fitting procedure for an argon neutral line from a Ø 5 mm atmospheric argon arc λ_0*=696.5 nm, I=180A, arc axis.*

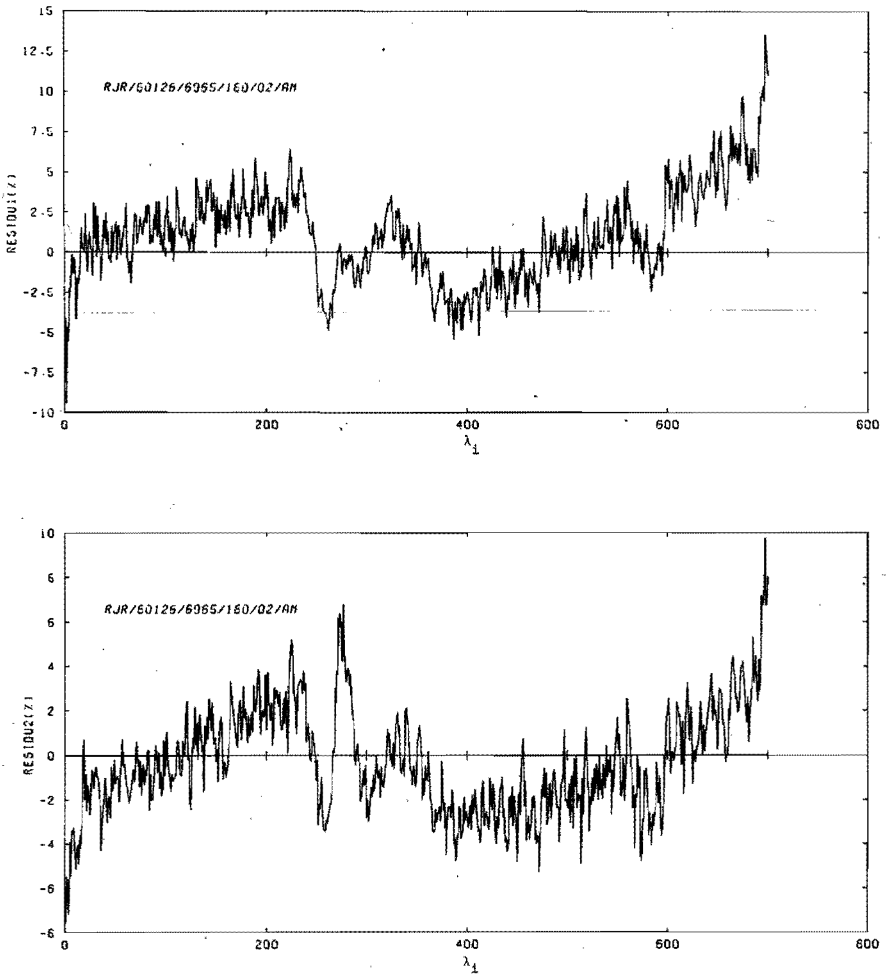

Fig. 3.8

Residuals of the fit shown in fig. 3.7

These residuals are defined by $100\times(\overline{I}_{\lambda_i,1} - \overline{I}^m_{\lambda_i,1})/\overline{I}^m_{\lambda_i,1}$ *and* $100\times(\overline{I}_{\lambda_i,2} - \overline{I}^m_{\lambda_i,2})/\overline{I}^m_{\lambda_i,2}$ *respectively.*

An error in the calibration factor leads to errors in

1. The source function
2. The temperature
3. The density of the excited states
4. The electron density

ad 1: The relative error in the source function is equal to the relative error in the calibration factor.

ad 2: The relative error in the temperature follows from (3.13).

With $T_e = T_{e0} + \Delta T$ and $S_\lambda = S_0 + \Delta S$ we obtain after linearization:

$$\frac{\Delta T_e}{T_{e0}} \simeq g(T_{e0}) \cdot \frac{\Delta S}{S_0} \qquad (3.19)$$

where $g(T_{e0})$ is given by:

$$g(T_{e0}) = [1-\exp(-\frac{\beta}{T_{e0}})] \cdot \frac{T_{e0}}{\beta} \qquad (3.20)$$

and $\beta = hc/\lambda k \simeq 2.18\ 10^4$ [K] at $\lambda = 696.5$ nm.

The function $g(T_{e0})$ is shown in fig. 3.9 for $\lambda = 696.5$ nm.

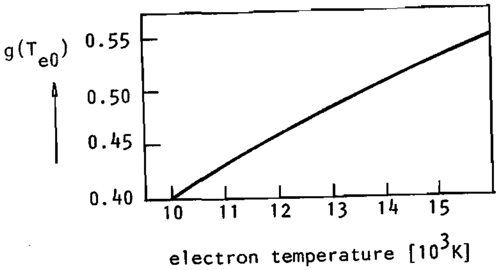

Fig. 3.9
The function $g(T_{e0})$ showing the influence of the relative error in S_λ on the determination of T_e.

With $\Delta S/S \approx \Delta C/C = 3\%$ (the calibration error), the error in the temperature is about 2%.

Another source of error in the determination of the temperature is a possible overpopulation of the lower excited state.
As was shown theoretically in chapter 2, this error amounts to a few tenths of a procent and we will accordingly neglect it.

ad 3: The error in the excited level density is caused by three effects: the calibration error, the uncertainty in the arc length and the uncertainty in the value of the transition probability. We estimate $\Delta n_1/n_1 \approx \Delta n_u/n_u \approx 5\%$.

ad 4: The error in the determination of the electron density is dominated by two effects:

a. The error in n_1

b. The error in T_e, which influences the determination of n_e through the factor $T_e^{1.5}[\exp -(E_{01}-E_1-\Delta E_{01})/kT_e]$ in the Saha equation (cf. (2.3)).

We obtain for the total error in n_e,

$$\frac{\Delta n_e}{n_e} \simeq \left(\frac{3}{4} + \frac{\gamma}{2T_{e0}}\right) \frac{\Delta T_e}{T_{e0}} + \frac{\Delta n_1}{n_1} \tag{3.21}$$

where $\gamma = (E_{01}-E_1-E_{01})/k \approx 4.78\ 10^4$ K for a 4p-4s transition.
The error in n_e determined in this way amounts to about 10% and is shown in fig. 3.10 as a function of T_e.
Additionally it can be remarked that the functional relationship between $\Delta n_e/n_e$ and $\Delta T_e/T_e$ is such that the variation in the values of $\Delta n_e/n_e$ as a function of T_e has practically the same slope as the $n_e(T_e)$ relation. This is an important conclusion to which we shall return in chapter 5.

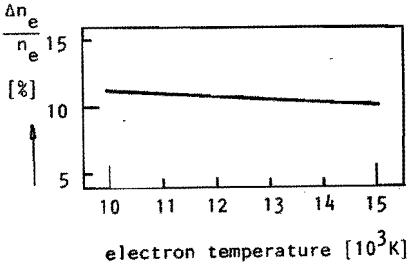

Fig. 3.10
Relative error in n_e as a function of T_e.

3.2.4 Determination of T_e from relative measurements of S_λ.

In the pulsed experiment that will be described in chapter 6, the spectral intensities $I_{\lambda,1}$ and $I_{\lambda,2}$ are measured as a function of time for one wavelength value in the line profile.

For these measurements the full spectral profiles of $I_{\lambda,1}(t)$ and $I_{\lambda,2}(t)$ are not available, and so we could not use the procedure described in section 3.2.3 to determine the plasma parameters.

A measurement under stationary conditions usually precedes the pulsed measurements, so a departing value of $S_\lambda(t_0)$ and accordingly of $T_e(t_0)$ is available ($t=t_0$ is the moment of pulse application).

From $I_{\lambda,1}(t)$ and $I_{\lambda,2}(t)$, $S_\lambda(t)$ can be calculated from the equations (3.6) (3.7) and (3.8). The temperature ratio $(T_e(t_1)/T_e(t_0))$ is obtained from equation (3.5):

$$\frac{T_e(t_1)}{T_e(t_0)} = \frac{\ln[\frac{\beta}{S_\lambda(t_0)} + 1]}{\ln[\frac{\beta}{S_\lambda(t_1)} + 1]} \tag{3.22}$$

The temperature $T_e(t)$ is determined from equation (3.22) as follows:

From the measured values of $I_{\lambda,1}(t)$ and $I_{\lambda,2}(t)$ we derive the ratio $S_\lambda(t)/S_\lambda(t_0)$. From the known value of $T_e(t_0)$ and equation (3.22) follows $S_\lambda(t)$ and using equation (3.22) again, we obtain $T_e(t)$.

3.3 Interferometric methods

3.3.1 Basic principles

Interferometric methods of measurement are based on the determination of changes in the index of refraction of a plasma. The change of the plasma refractive index is given by:

$$\delta(\mu_r-1) = 2\pi\alpha_A(\lambda)\delta n_1 + [2\pi\alpha_I(\lambda) - \omega_p^2/2\omega^2]\ \delta n_e \qquad (3.23)$$

where μ_r is the plasma index of refraction, $\alpha_A(\lambda)$ is the polarizibility of the atoms, $\alpha_I(\lambda)$ that of the ions ω_p is the plasma frequency and $\omega=2\pi c/\lambda$.

In equation (3.23) we have assumed quasi-neutrality, i.e. $\delta n_+=\delta n_e$, and we have neglected the contribution of the excited states to the refractive index. This is in accordance with the findings of Baum et al. [BAU75].

The output of the interferometer due to changes in n_e and n_1 is proportional to $\delta(\mu_r-1)$ by the relation (l is the plasma length):

$$\Delta(\lambda) = \delta(\mu_r-1)\cdot\frac{2l}{\lambda} \qquad (3.24$$

Where $\Delta(\lambda)$ is the so-called fringe shift in the interferometer signal. The fringe shift is measured. Note that twice the plasma length has been introduced in this equation. This is a consequence of the set-up used, which will be discussed in section 3.5.2.

We want to deduce δn_e from (3.24), from measurements of the fringe shift $\Delta(\lambda)$. However $\delta(\mu_r-1)$ depends on both δn_1 and δn_e. By measuring the change of μ_r-1 for two values of the wavelength λ_1 and λ_2, we obtain 2 equations for δn_e and δn_1. These are solved to yield:

$$\delta n_e = \frac{B\lambda_1\Delta(\lambda_1) - \lambda_2\Delta(\lambda_2)}{2l\cdot\frac{\omega_p^2}{\omega^2}[\lambda_2^2-B\lambda_1^2]} \tag{3.25a}$$

$$\delta n_1 = \frac{\lambda_2\Delta(\lambda_1) - \lambda_1\Delta(\lambda_2)}{2l\cdot 2\pi\alpha_A(\lambda_1)[\frac{\lambda_2}{\lambda_1} - B\frac{\lambda_1}{\lambda_2}]} - A\delta n_e \tag{3.26a}$$

In these equations the following notations have been used:

- $A=\alpha_I(\lambda)/\alpha_A(\lambda)$ is the ratio of the ion polarizability to that of the atoms. We have taken values for α_I and α_A from Ferfers [FER79]. $\alpha_I=1.03\ 10^{-30}\ m^3$ and $\alpha_A=1.642\ 10^{-30}\ m^3$.
- $B=\alpha_A(\lambda_1)/\alpha_A(\lambda_2)=1.01$ for $\lambda_1=0.6328\mu m$ (red) and $\lambda_2=3.3912\mu m$ (infrared). [ALP65, FER79, NIC79].

  λ_1 and λ_2 are the two laser wavelengths of the HeNe laser (cf. section 3.3.2).

With $\omega_p^2/\omega^2=4.46\ 10^{-20}\cdot\lambda^2\ m^3$, (3.25a) and (3.26a) yield:

$$\delta n_e = [-3.404\ 10^{20}\ \Delta(\lambda_2) + 0.628\ 10^{20}\ \Delta(\lambda_1)]/l \tag{5.25b}$$

$$\delta n_1 = [-0.558\ 10^{22}\ \Delta(\lambda_2) + 3.099\ 10^{22}\ \Delta(\lambda_1)]/l \tag{5.26b}$$

In these equations $\Delta(\lambda_1)$ and $\Delta(\lambda_2)$ are the fringe shifts for the red and infrared laser wavelengths.

We will use these equations to determine δn_e and δn_1 from measurement of the fringe shifts Δ with the set-up which will be described briefly in the next section.

3.3.2 *Principle of operation of the interferometer*

The interferometer used is of the coupled cavity type (cf. [ASH63]). The basic set-up is shown in figure (3.11).

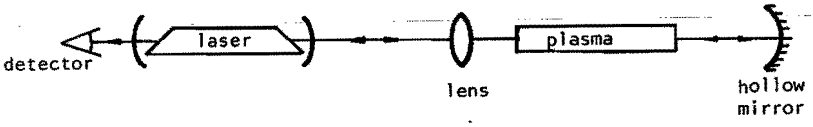

Fig. 3.11
Basic set-up of the coupled cavity laser interferometer.

The optical cavity of the laser corresponds to the reference arm of a conventional interferometer.

The laser beam passes through the plasma twice, before and after being reflected by the spherical mirror.

Due to changes in the plasma refractive index the beam arrives at the laser with different phase, and this causes interference in the laser cavity [KIN63]. The resulting modulation in the laser amplitude (fringes) can be used to determine the change of refractive index.

The variation in the refractive index can be produced in different ways.

a. To obtain values of n_e in the stationary state, the arc is short-circuited. The resulting fringes, due to the decay of n_e, are counted during a period of time that is long enough for the electrons to decay to negligible values. The resulting change $\delta n_e(t \to \infty)$ yields the value of n_e at the moment that the arc was short-circuited.

b. Application of a current pulse to the arc, which also causes a change of $\delta(\mu_r - 1)$ due to the subsequent changes of the particle densities.

We note here that generally δn_e can be determined from (3.25) with more precision than δn_1 (from (3.26)).

In the afterglow measurements (after shortcircuiting of the arc) usually n_e decays faster than n_1, and so a stationary value of δn_e is obtained in the measuring interval.

This is not so for δn_1, which increases much slower. Increasing the period of measurement is not always successfull, because then mechanical vibrations of the set-up are also measured.

In addition, the number of fringes is usually much larger for the infrared wavelength (λ_2=3.3912 m) than for the red one (λ_1=0.6328μm) as $\omega_p^2/\omega^2 >> \alpha_A$ or α_I and $\lambda_2^2 >> \lambda_1^2$.

Typically $\Delta(\lambda_2) \simeq 5\Delta(\lambda_1)$ and from (5.25b) and (5.26b) it is apparent that the error in δn_1 is more sensitive for errors in the fringe-count than δn_e.

CHAPTER IV. EXPERIMENTAL SET-UP

4.1 Introduction

In this chapter the different arrangements used for the experiments in this thesis are briefly described.

The chapter consists of three sections in which the spectroscopic set-up (4.2), the interferometric set-up (4.3) and the apparatus (4.4) are described.

In each section the experimental arrangements for the stationary and for the pulsed measurements are shortly discussed.

Also the data collection and analysis is described for the different situations.

4.2 The spectroscopic set-up

We have used the methods described in section 3.2 for the measurement of T_e in two different situations:

1. Stationary measurements in which the plasma current is kept constant during the whole measurement procedure.

   $I_{\lambda,1}$ and $I_{\lambda,2}$ are determined in a number of equally spaced wavelength intervals in the line profile. In this way the information contained in the line can be used fully and, in addition, a check can be made on the assumption of constancy of S_λ over the line profile and its adjacent continuum.

2. Pulsed measurements.

   In these measurements the current through the arc is pulsed from a certain stationary value to a substantially higher value. At these conditions the time development of the intensities $I_{\lambda,1}(t)$ and $I_{\lambda,2}(t)$ are measured for several wavelength positions in the line profile.

Knowing the temperature before the application of the current pulse, it is possible to follow the temperature evolution during the pulse (section 3.2.4). In this way additional information can be obtained about the dynamic processes that determine the equilibrium state of the plasma (cf. chapter 6).

4.2.1 Experimental arrangements and data collection

Figure 4.1 is a schematic representation of the spectroscopic set-up. (next page).

Table 4.1 explains the notations used in this figure.

Table 4.1

BM	Back mirror (spherical; R=0.5m)
CH1, 2, 3	Computer controlled choppers
CL	Calibration lamp
D1, D2	Pinholes
F	Filter
L1, L2, L3, L4	Lenses
M	Plane mirror
PM	Photomultiplier
PRM	Partially reflecting mirror
RM	Rotatable mirror

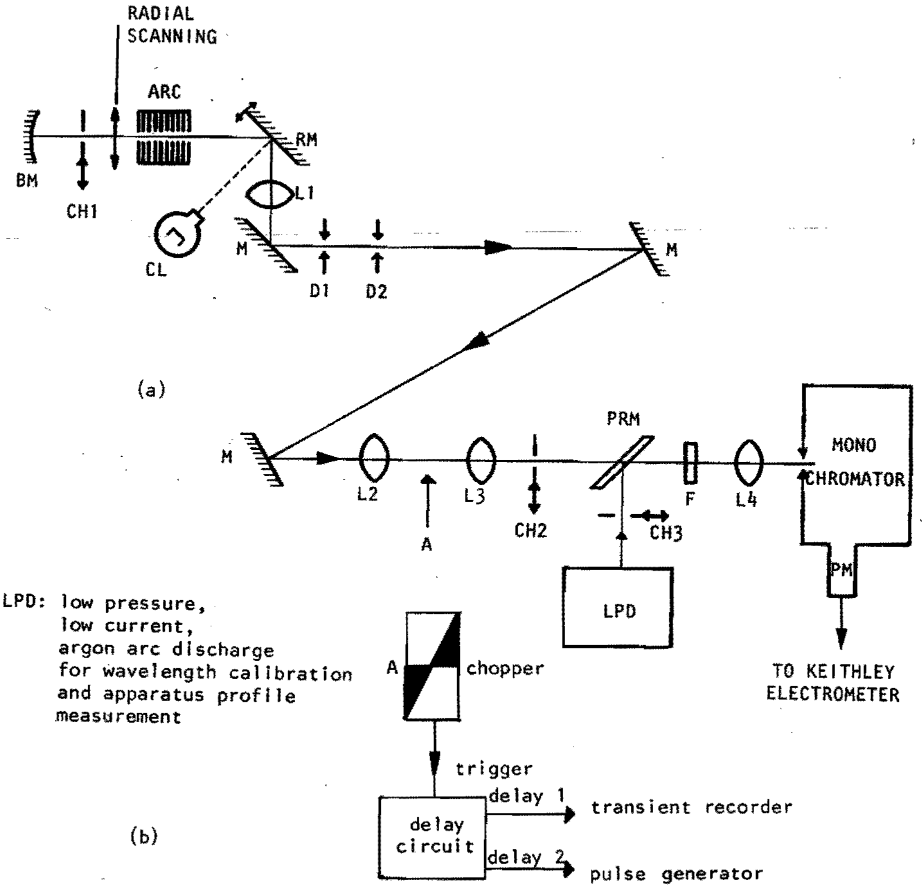

Fig. 4.1

Diagram of the spectroscopic set-up

a. Set-up used for the stationary measurements

b. Extension of the set-up during pulsed measurements. The additional chopper is placed in position A.

Radial scanning of the plasma is possible by moving the entire arc in a direction perpendicular to the optical axis (keeping the axis of the plasma parallel with the optical axis).

Next we will consider the different parts of this set-up.

4.2.1.1 The optical system

The arc plasma is observed end-on through the telecentric optical system formed by the lens L1 which is positioned at a distance of twice its focal length from the center of the plasma.

At the other side of this lens two pinholes are placed: D1 in the focal point of the lens and D2 at twice the focal length. The remainder of the optical arrangement images the arc on the entrance slit of the monochromator.

The diameter of pinhole D1 and the focal length of L1 determine the acceptance angle of the optical system. In most cases this angle was limited to less than 1 mrad.

The diameter of D2 determines the diameter of the cylindrical region of the plasma that is observed. This diameter has to be chosen small compared to the plasma diameter. For 5-8 mm diameter arcs we have taken 0.4 mm pinholes for both D1 and D2.

By these values of the pinhole diameter the observed beam of light is diffraction limitted. The pinholes pass a beam consisting of one transversal mode with a waistlength $L_w \approx 0.02$ m. (cf. section 4.3).

The spherical mirror behind the arc makes it possible, in combination with the chopper CH1, to measure $I_{\lambda,1}$ and $I_{\lambda,2}$ alternatively (cf. section 3.2). It is placed at a distance of 0.50 m behind the arc and images the center of the arc back onto itself. As the arc length is not negligible, the arc and its image do not coincide exactly.

We used ray tracing matrix methods [GER75] to estimate the influence of the non-ideal imaging. We obtain a mismatch between the ideal and the actual radial position in the plasma column (after reflection by BM) of less than 5%, for a plasma length of 0.1 m.

The image of the arc on pinhole D1 is a circular spot with a diameter which depends on the axial position in the arc.

For $I_{\lambda,1}$ the imaging is such that the spot diameter is smaller than the pinhole diameter for all axial positions.

For $I_{\lambda,2}$, the spot diameter is larger than the pinhole diameter, for those parts of the arc at distances (to D1) greater than the distance from the arc center to the pinhole.

This results in an additional attenuation of the intensity of $I_{\lambda,2}$. This effect is accounted for in our measurements as it can be included in the factor τ^2R (cf. equation 3.8).

Selffocussing of the reflected beam has been investigated with the approach given by Kleen et al. [KLM69] assuming a parabolic profile for the radial density profiles. For the conditions of our measurement this effect is negligible.

The remainder of the optical system forms an image of the plasma on the entrance slit of the monochromator (a Jarrell-Ass 1 meter double monochromator of the Czerny-Turner type).

Part of the light path consists of a parallel beam in which a partially transparent mirror (PRM in fig. 4.1) has been placed. This allows the inclusion of an additional profile from a low pressure argon discharge [NIE79]. We used this additional profile to obtain 1. an independent measurement of the apparatus profile (the broadening of these profiles is negligible) 2. a wavelength reference for the measured profiles from the investigated arc.

4.2.1.2 Data collection

Depending on the measurement conditions (stationary or pulsed), the electrical signal from the photomultiplier is processed in two ways:

1. Stationary measurements:

The current from the photomultiplier (type EM19698QB/S20) is measured by a Keithley 602 solid state electrometer in the configuration of fig. 4.2.a. The output signal from the amperemeter is then converted to a pulse train by an analog to frequency converter. The frequency is proportional to the amplitude of the measured signal. (Voltage range 0-3V; frequency range 0-500kHz). The pulse train is fed to a micro-processor (M6800) controlled gate with programmable gate time (usually set to 0.1 sec).

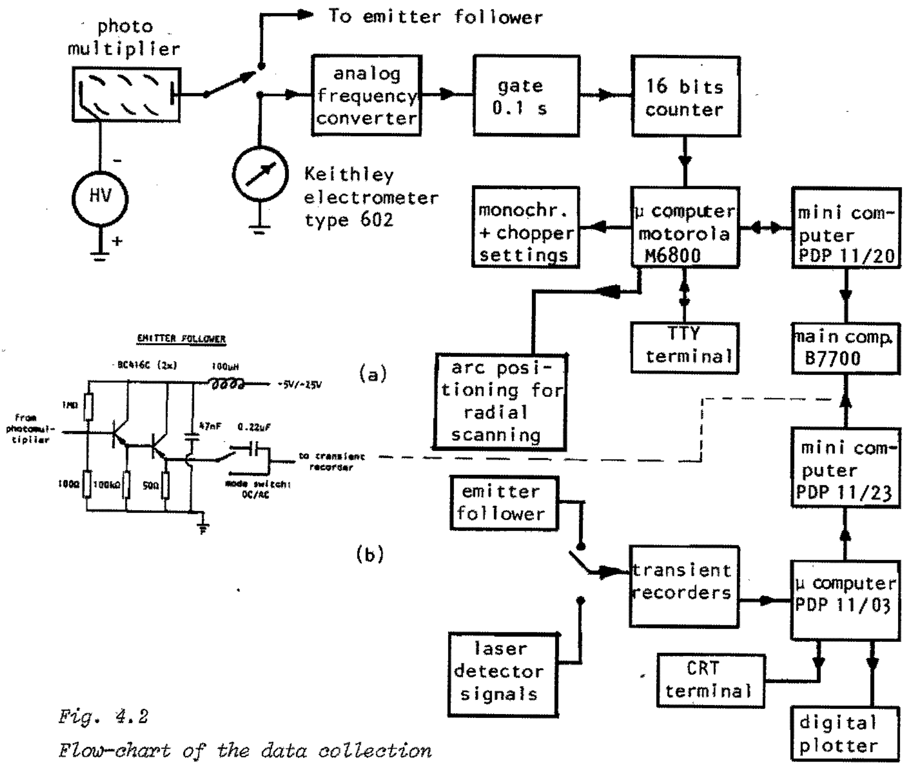

Fig. 4.2
Flow-chart of the data collection
a. Spectroscopic measurements
b. Pulsed measurements and interferometry.

The pulses which arrive during the gate-time, are counted and the accumulated number is stored.

The measurement sequence is sketched in fig. 4.3. (Next page).

Each signal (reference signal, $I_{\lambda,1}$ and $I_{\lambda,2}$) is measured a predetermined number of times. Then a mean value is calculated and stored in an appropriate memory location. The monochromator is set to the next wavelength setting, and a new sequence is measured. After scanning the complete line, first the collected data are displayed on a local plotter, then they are sent to a DEC PDP 11/20 computer for storage, and later they are sent to the central computer system (Burroughs B7700) for data analysis.

After measurement of a line under different conditions (e.g. different values of the current) an absolute calibration is made (cf. section 3.2.2).

2. Pulsed measurements

For the pulsed measurements the spectroscopic set-up is extended with an additional chopper and timing circuit as shown in fig. 4.1.b.

The diameter of pinholes D1 and D2 has to be increased to 1 mm to pass sufficient photons in the pulsed state. The data collection is performed by a circuit that is schematically represented in figure 4.2.b.

The photomulitplier signal is fed to a cascaded emitter-follower with an impedance transformation ratio of 100kΩ to 50Ω, so a current amplification factor of 4.10^4 is achieved, at a time-constant of about 0.1μs.

The signals are then measured by a transient recorder, which admits signals with a peak-to-peak value of 512mV.

The digitizer is triggered by the chopper. About 100μs later the pulse generator is triggered by the delayed trigger of the chopper, initiating the current pulse. As the chopper frequency is adjusted in such a way that the light path is closed, before the sampling cycle ends, also the zero light

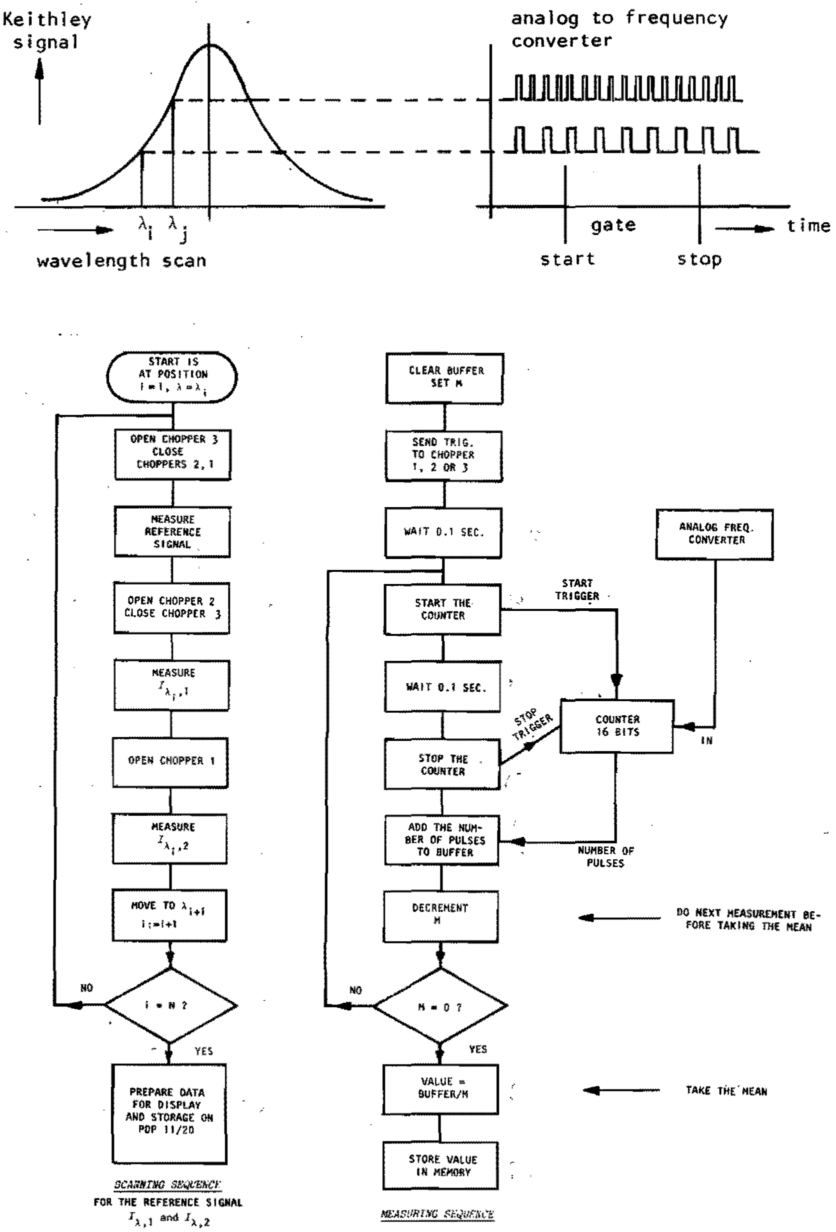

Fig. 4.3

Measuring sequence and first step in the data collection procedure, for stationary measurements.

level is obtained. After receiving a trigger signal, the transient recorder samples the signal for 1024 time-intervals of a preselected duration (from 50μs per sample to 5μs per sample). The signal is then digitized and stored in a buffer memory. This buffer can be displayed on an oscilloscope, and eventually stored in the main memory of an online PDP 11/03 microcomputer. With the PDP 11/03 computer, the results of a certain number of shots can be averaged and afterwards sent to a larger computer for storage. An example of the digitized, time varying intensity of the 696.5nm ArI line (at λ=696.6nm and apparatus profile width of about 0.04nm) is shown in fig. 4.4.

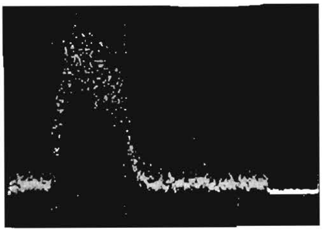

Fig. 4.4
Picture of the digitized intensity variation for the pulsed measurements. Note that also the light level corresponding to the stationary situation and the zero light level are shown.
Vert.scale: relative units; hor.scale: 204.8 μs/div (1024 samples; 2 μs/sample).
Argon arc; ∅ 8mm; stationary arc current: 80A; 1 bar; λ_0 *= 696.6 nm; arc axis.*

Before a pulsed measurement, a stationary measurement is done at the same current setting. In this way an indirect calibration of the time dependent intensities is obtained (cf. section 3.2.4).

All datasets are processed on the central computer system.

4.3 Interferometric set-up

The theory of the change in the plasma refractive index caused by density changes in the plasma has been briefly described in section 3.3. In this section we will use the mentioned principle for the determination of density variations in a decaying and in a pulsed plasma. First the principles of operation of our interferometric set-up will be described, and then the data collection and reduction will be discussed.

4.3.1 *Experimental arrangements*

The experimental set-up is shown in figure 4.5

The abbreviations used are explained in the following table, table 4.2.

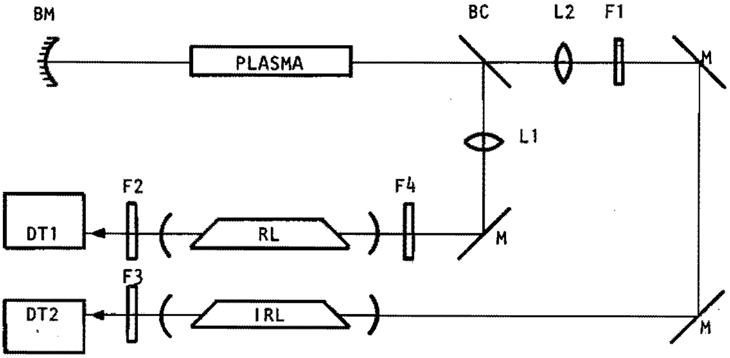

Fig. 4.5
Diagram of the interferometric set-up.
The two laserbeams probe the same plasma volumes as in the spectroscopic set-up.
Also the same spherical mirror is used and in the same position as in the spectroscopic set-up.

Table 4.2

BC	Beam combiner; reflecting on the front side for $\lambda = 0.6328\mu m$ transparent from the rear for $\lambda = 3.3912\mu m$
BM	Back mirror (hollow; R = 0.250µm)
F1	Blocking filter for $\lambda < 3.3912\mu m$
F2, F3	Line filters 0.6328µm
F4	Gray filter
L1, L2	Quartz lenses ($f_1 = 0.5$ m $f_2 = 0.45$ m)
DT1, DT2	Pin diodes (D_1: EG&G SGD 100A and D_2: Wacker JD 12.)
M	Plane mirrors
RL	He Ne laser $\lambda = 0.6328\mu m$ (Spectra Physics)
IRL	He Ne laser $\lambda = 0.6328\mu m$ and $\lambda = 3.3912\mu m$ (this laser was developed and built, in cooperation with the laser Metrology group of the department of Mechanical Engineering of this university).

By carefull alignment of the interferometric set-up in conjunction with the spectroscopic set-up nearly the same cylindrical part of the plasma column was observed in both experiments.

Due to the fact that the laser beam waists are functions of wavelength and position, each beam is a compromise between the minimum waist diameter w_0 and the divergence $\lambda/\pi w_0$ of the beam.

We calculated the minimum beam waist for each wavelength using the formalism of Kogelnik and Li [KOG66] for the description of gaussian beams.

First the volume that a beam of minimum waist w_0 occupies in the plasma of length l is calculated from:

$$V(\lambda, L, l) = \pi \int_{-\frac{1}{2}l}^{+\frac{1}{2}l} w^2(z)\, dz = \lambda l L_w \{1 + l^2/3L_w^2\} \qquad (4.1)$$

where the position dependent waist w(z) is given by

$$w^2(z) = w_0^2 \{1+(z/L_w)^2\}, \tag{4.2}$$

and the waistlength L_w by

$$L_w = \frac{\pi w_0^2}{\lambda} \tag{4.3}$$

The minimum waist has been positioned at the center of the arc and the integration is over the arc length.

For a given plasma length l the volume V is minimized with respect to L_w by setting $\frac{\partial V}{\partial L_w} = 0$. The following relation between L_w and l results:

$$L_w = \frac{1}{2\sqrt{3}}\, l \tag{4.4}$$

For V_{min} we get

$$V_{min} = \frac{1}{3}\sqrt{3}\,\lambda l^2 \tag{4.5}$$

This is a relation for obtaining a beam of minimum volume in a plasma of given length, when the waist is positioned at the center of the plasma. From equation (4.2) it follows that the variation of the waist of the infrared laser beam is more pronounced than that of the red laser beam. So we minimize the infrared laser beam volume. For a plasma length l = 80mm we obtain from (4.4) for the waist length at minimum volume:

$$L_w\ (\lambda=3.3912\mu m) \approx 23\ mm \tag{4.6}$$

or equivalently

$$w_o(\lambda=3.3912\mu m) \approx 0.16\ mm \tag{4.6a}$$

Next the minimum volume for the red laser beam is set equal to $V_{min}(\lambda=3.3912\ m)$ and we obtain

$$L_w(\lambda=0.6328\mu m) \simeq 247\ mm \qquad (4.7)$$

and $w_0(\lambda=0.6328\ m) \simeq 0.22$ mm (4.7.a)

We recall that the beam waist for the spectroscopic measurement is about 0.25 mm (with a waist length of about 200 mm at λ=700 nm).

The beam profiles are shown in figure 4.6 for the red and infrared laser beams, and for the spectroscopic measurement.

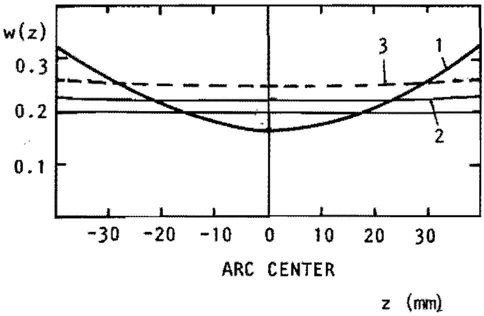

Fig. 4.6
Beam waists in the plasma.
1. Infrared laserbeam (λ = 3.3912 μm)
2. Red laserbeam (λ = 0.6328 μm)
3. Spectroscopy.

Note that as the waist lengths are relatively long for the red laser beam and in the spectroscopic measurements, the characteristic hyperbolic profile is not pronounced for these beams.

In interferometers of the feed-back type usually the reflected laserbeam is made to coincide with the incoming beam to avoid exagerated losses. This is only possible when the wavefront at the spherical mirror has the same radius of curvature as the mirror. In addition, this condition should be fulfilled for both the red and the infrared wavelengths.
As the radius of curvature of a gaussian wavefront is given by [KOG66]:

$$R(z) = z\{1+(L_w/z)^2\} \tag{4.8}$$

Deviations from the ideal situation result from our choice of waistlengths as $R(z = 500\ \text{mm}; \lambda=0.6328\mu\text{m}) = 620$ mm and $R(z=500\ \text{mm}; \lambda=3.3912\mu\text{m}) = 501$ mm.

The radius of curvature of the spherical mirror is $R = 500$ mm.

For the red laser beam the mismatch is approximately 25%. However, as the waistlength of this beam is long, a small shift of the position of the waist in the plasma, does not affect the beam profile in the arc. A shift of about 50 mm proved to be sufficient for optimizing the interference signal, and match the radius of curvature of the beam to that of the mirror. This was done during the alignment procedure.

4.3.2 *Data collection*

We used the interferometric set-up in the determination of particle density changes in the two situations of interest: (1) stationary determination of n_e and n_1 in the afterglow following arc interruption, and (2) changes of n_e and n_1 during the application of a current pulse to the plasma.

1. Afterglow measurement

For these measurements, the arc current is short-circuited with a fast switching device, with the set-up described in section 4.4.

Subsequently particle densities and temperatures will decay to values corresponding to the room-temperature situation. The changes in n_e and n_1 that accompany this decay then produce the fringe shifts that are detected and counted.

Figure 4.7 shows typical interferograms that result after interruption of the arc current. Part a of this figure is the resultant interferogram for the red laser line $\lambda=0.63\mu m$, and part b is the result for the infrared line $\lambda=3.38\mu m$.

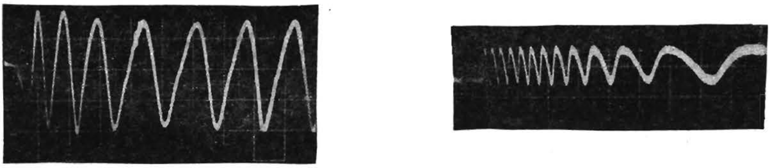
(a) (b)

Fig. 4.7
Example of oscilloscope traces of the fringe patterns in the afterglow following short-circuiting of the arc.
Argon arc; Ø 8mm; DC current: 65A; 1 bar.
Vert. scale: relative units.
Hor. scale: (a) red laser line (λ = 0.6328 μm): 200 μs/div
(b) infrared laser line (λ = 3.3912 μm): 100 μs/div

In the measurements the interferograms are recorded for longer periods of time than follow from these figures. Even then n_1 does not reach a saturation value. For n_e the time interval of measurement is sufficient.

Recording the interferograms for still longer periods of time not always results in an improved situation, because then mechanical vibrations of the set-up interfere with the experiment.

2. Pulsed measurements

The density variations are produced by a current pulse as will be discussed in section 4.4. As the amplitude of the applied current is quite high, the increase and decrease of the infrared fringes during the pulse is very fast. The 1024 samples that can be obtained of the interferogram are not enough to describe the interferometric signals completely.

For this situation usually three transient recorders are connected in "cascade" according to the scheme presented in figure 4.8.

Here we have used a feature of the transient recorders that allows the recorders to trigger one another, e.g. TR2 is triggered by TR1 204.8μs (= 1024x0.2μs) and TR3 is triggered by TR2 409.6μs (= 204.8μs + 1024 x 0.2μs) after initiation of the current pulse (cf. fig. 4.8).

So the total interferogram is sampled for 921.6μs, with increasing sampling rates in different portions of the waveform (cf. fig. 4.8a).

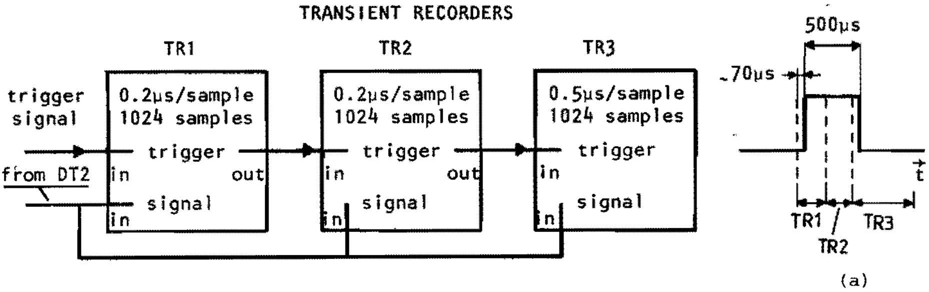

Fig. 4.8
Timing sequence and connection of the 3 transient recorders for pulsed measurement of the infrared interferograms.
(a) Timing with respect to the current pulse.

4.4 Apparatus and technical set-up

4.4.1 *Apparatus*

The plasma is produced in a cascade arc as sketched in figure 4.9. The arc channel is formed by the central bore of a series of copper plates (cf. fig. 4.10). Each plate contains an interval channel system through which a cooling liquid (in our case water) can flow; the plates are isolated electrically from one another by means of appropriate silicone rings. The plate thickness is 1.6 mm, the interspacing between the plates is about 0.2 mm.

By means of the water-collectors the plates are pressed together, allowing the coolant to flow from plate to plate without leaking into the arc channel. A reservoir and a circulating pump complete the cooling system. Typical flow-rate is 200 l/min at a water pressure of 10 bar.

The watercollectors also contain the 8 electrodes. Each electrode, consisting of a hollow copper shaft and a tungsten tip, is individually cooled. The diameter of the electrodes for high current values is about 8 mm. For lower values of the current the cathode tip diameter was reduced to 6 mm. The electrodes are positioned, along the arc circumference, 4 on each side of the arc channel, in such a way that the plasma can be observed end-on.

The arc current is supplied by a current regulated power supply; either a "Diode" 750V/100A or a "Smit" 250V/300A can be connected to the electrode assembly. A stabilizing resistor is placed in series with the arc. This resistor dissipates around 40% of the total power supplied to the electrical circuit. For good stability, a value of 3Ω proved to be sufficient in the case of the "Diode" power supply, while with the "Smit" supply a value of 0.16Ω was used (because of the lower supply voltage).

In order to provide a means for short-circuiting and pulsed operation, several extensions have been added to the basic set-up.

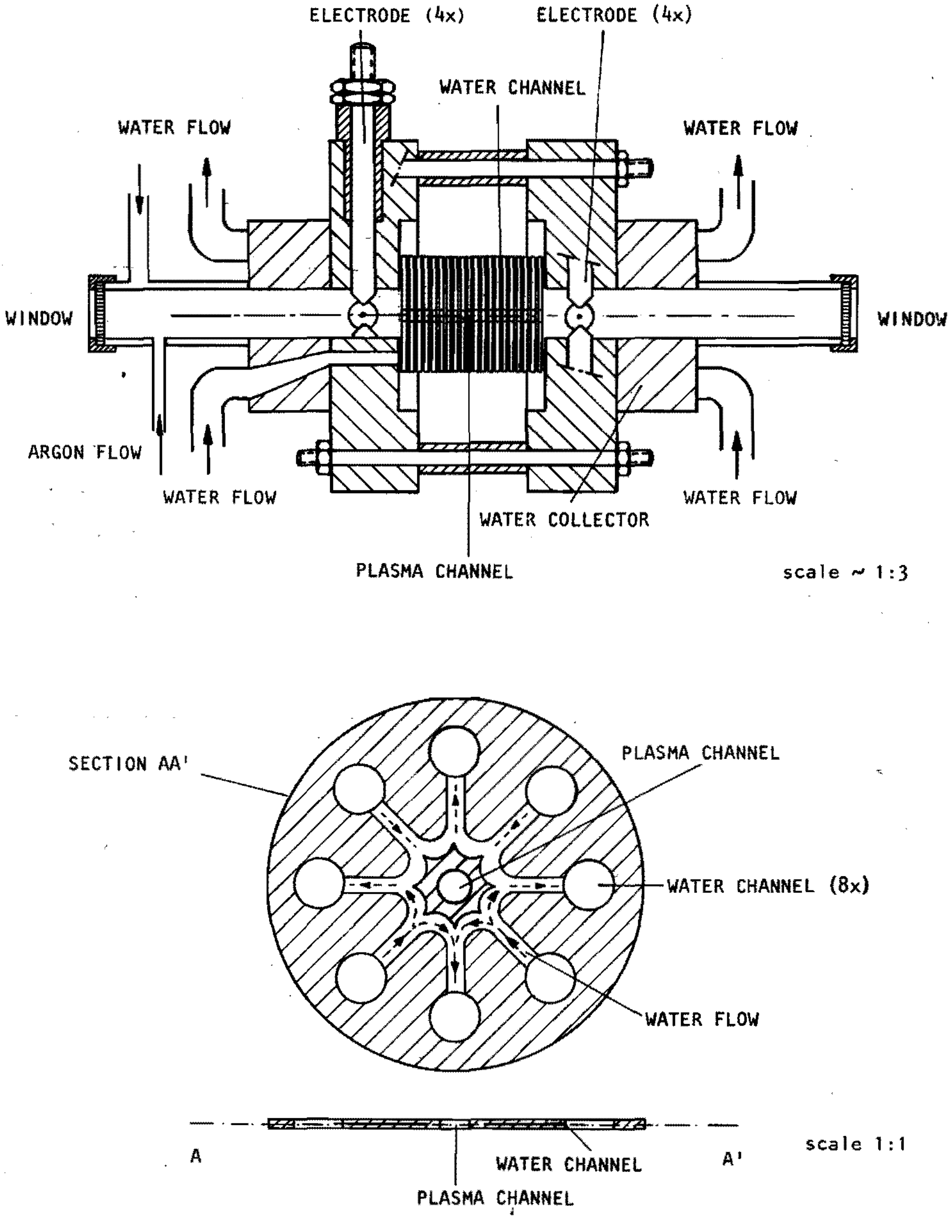

Fig. 4.9 and 4.10
Overall view of the cascade arc and of one of the cascade arc plates.

4.4.2 *Controlled short-circuiting of the arc*

By short-circuiting the arc the electron and neutral densities can be changed from the stationary value to a value corresponding to zero current conditions.

Short-circuiting of the arc current can be accomplished by switching a Silicon Controlled Rectifier (thyristor), that is connected in parallel with the electrodes, to the conducting state.

The arc current can be switched off in a time of less than 1μs, corresponding to the on-state transition time of the thyristor ("Brown Boveri"; type CS110) used. Diodes are placed in series with the switch-off thyristor to prevent current oscillations in the circuit.

4.4.3 *Current pulsing*

Pulsed operation of the arc is achieved with a high current, fast rising pulser built in our group, after the design of Pearce et al. [PEA67].

Fig. 4.11 is a schematic representation of the current pulser. Referring to this figure, the operating principle of the pulser can be described as follows:

Capacity C_1 (1360μF) is charged through R_1 to a voltage V_1 ($V_{1max} = 700V$, typically 500V). The start pulse switches on thyristor SCR1, initiating the main current pulse. The rise-time of the pulse is short: typically less than 2μs. The maximum voltage at the output is V_1 volts. This level decays with a time constant equal to the product of the load impedance plus 1Ω and the capacitance of C_1. This is typically 2.5 ms. After a preselected time delay, the stop pulse is applied to the circuit, switching on thyristors SCR2 and SCR3 at the same time. SCR2 connects a lower impedance in parallel with the load, decreasing the time-constant of the circuit by a factor of 5. At the same time SCR3 discharges C_2, which is loaded to a value $-V_1$(through R_2) across C_1.

By applying the voltage of C_2 to the circuit, thyristor SCR1, a fast turn-off type, is switched off abruptly, terminating the pulse with a short fall-time (<3µs). The advantage of this circuit is that full profit is taken of the fast turn on time of most thyristors, and additionally, by choosing the pulse length not too large (max. 500µs) the duty cycle is reduced, as C_1 does not become discharged completely each time. A major draw-back of this circuit is that it is in fact a "constant" voltage circuit, and so to a certain extent the pulse current depends on the load impedance (for small loads). Accordingly the pulse current applied to the arc depends on the dynamic impedance of the arc.

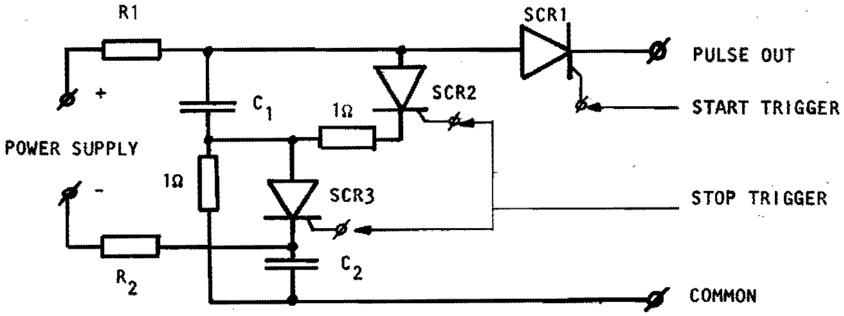

Fig. 4.11

Simplified electrical circuit diagram of the current pulse generator for illustration of the principle of operation.

C_1: *1360µF/900V*

C_2: *~ 5000µF/900V*

SCR 1, 2 and 3: BBC CS38-12ip

R_1, R_2 *loading resistors*

The current pulse is supplied to the arc through diodes. An additional feature of these diodes is that they protect the current pulser with respect to the DC power supply. On the other hand the series inductance in the circuit (distributed and lumped; 100 mH) and parallel capacitors (5000μF) protect the arc power supply from the current spikes.

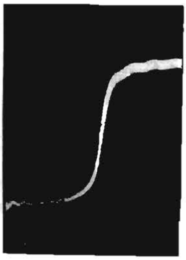

(a)

(b)

Fig. 4.12
Rise-time (a) and overall shape (b) of the current pulse measured with a Rogowskii coil. (400 turns; Ø 0.5mm wire; winding 35x2 mm^2; coil diameter 70mm; core: teflon; around the arc plates.
Vert.scale: 25A/div
Hor.scale : (a) 1μs/div
(b) 100μs/div

Figure 4.12 is an example of an oscilloscope trace, which shows the overall shape of the current pulse.

Part a of this figure shows the rise-time of the pulse, and in part b the complete pulse is shown. The droop in the signal which is caused by the slow discharging of C_1, and which amounts to about 12%, can also be seen. This means that after each pulse, C_1 has only lost about 12% of its charge.

For a pulse-width of 500μs, a pulse repetition frequency of 10 Hz can be attained. If the pulse-width is decreased, then a maximum repetition frequency of about 100 Hz can be attained.

CHAPTER V EXPERIMENTAL RESULTS OF THE STATIONARY MEASUREMENTS

5.1 Introduction

In this chapter we present results obtained with the experimental methods and arrangements described in the chapters 3 and 4.
First the results of the measurements of the electron temperature and density are given and compared with the corresponding LTE values (section 5.2).
The overpopulation of the ground state density is derived from the measurements and compared with the results of the simplified 4 level model of chapter 2 (section 5.2.2.).
From the obtained results, values for the total excitation-ionization rate coefficient (section 5.2.3) and the electrical and thermal conductivities (section 5.2.5) are derived and compared with the literature.
The influence of diffusion is treated separetely in section 5.2.1 and in section 5.2.4 the time constants for diffusion and radiative recombination are compared.
In section 5.3 the results for the electron density obtained with the source function method are compared with results obtained with the interferometric methods.

5.2 Results for the electron temperature and density

The electron temperature and electron density were measured at atmospheri pressure, in arcs of different diameters (5 mm and 8 mm) and of different lengt Using the procedure described in section 4.2 the absorption and emission profi of several lines of the 4p-4s group of the argon neutral spectrum were measure The relevant parameters of these lines are given in table 5.1 [WIE69].

Table 5.1 Parameters of the measured transitions

λ_0 (nm)	transition	$A[10^7 sec^{-1}]$	g_u	g_l	$\hat{E}_e$[eV]	$\hat{E}_l$[eV]
696.5	$4s[\frac{3}{2}]^0-4p'[\frac{1}{2}]$	6.7	3	5	13.328	11.549
727.3	$4s[\frac{3}{2}]^0-4p'[\frac{1}{2}]$	2	3	3	13.328	11.624
750.4	$4s'[\frac{1}{2}]^0-4p'[\frac{1}{2}]$	4.72	1	3	13.480	11.828
763.5	$4s[\frac{3}{2}]^0-4p[\frac{3}{2}]$	2.74	5	5	13.173	11.549
794.8	$4s[\frac{1}{2}]^0-4p'[\frac{3}{2}]$	1.96	3	1	13.284	11.724

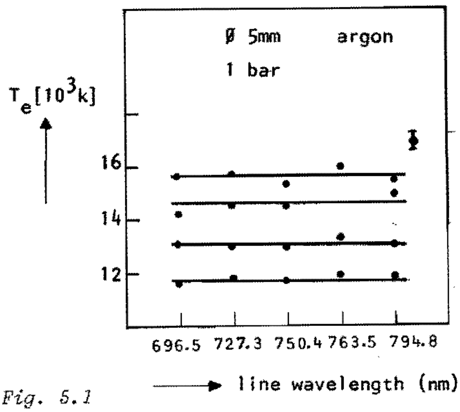

Fig. 5.1

Electron temperature values as determined from various transitions of the 4s-4p groups.

Under assumption of PLTE we determined the temperature T_e from the source function. Fig. 5.1 shows values of T_e found from measurements at the different wavelengths, for several values of the arc current (5 mm diameter arc). The values of T_e obtained in this way coincide within about 2% which is within the experimental error. We conclude from these measurements that further investigations of T_e can be carried on using the results of measurements at one wavelength. In this chapter we report on results based mainly on measurements at 696.5 nm.

Figure 5.2 shows measured radial profiles of T_e.

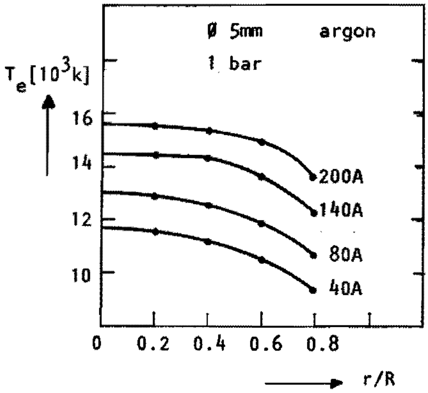

Fig. 5.2
Radial dependence of the electron temperature for 4 values of the arc current.

The temperature profiles are given for different values of the current. We used these profiles in our estimates of the effect of diffusion and to obtain values for the electrical and thermal conductivities. We will return to these calculations later in this chapter.

From the total line intensity, values of n_e can be calculated using the assumption of PLTE (cf. section 3.2).

For each measurement we obtain thus pairs of values of n_e and T_e. The $n_e(T_e)$ relation is shown in fig. 5.3

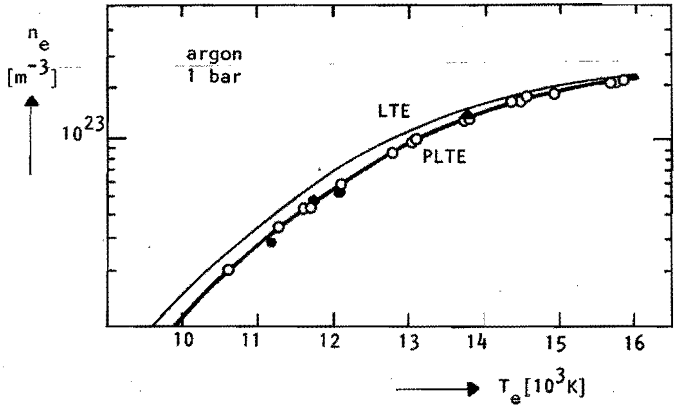

Fig. 5.3

The relation between the electron temperature and electron density in an atmospheric argon arc plasma.

PLTE : values of n_e and T_e determined experimentally under the assumption of Partial Local Thermal Equilibrium.

LTE : Values of n_e and T_e from LTE calculations of the plasma composition.

0 : results of measurements with a 5 mm diameter arc.

● : results from a 8 mm diameter arc.

▲ : a result obtained in a 4 mm diameter arc of the University of Kiel (BRD).

In this figure measurements are shown for 5 mm and 8 mm diameter argon arcs at atmospheric pressure. Also drawn in the figure is the $n_e(T_e)$ relationship, that results from LTE calculations. The different values of T_e in the figure were obtained from the experiment by

1. Variation of the arc current. From I=40A to I=220A for the 5 mm diameter arc and from I=25A to I=100A for the 8 mm arc;
2. Performing measurements at different values of the arc radius.

Note that at higher values of $n_e(T_e)$, the measured curve approaches the LTE curve; at lower value of $n_e(T_e)$ the discrepancy becomes larger, as expected. Also shown in the figure is a value obtained from a measurement on a 4 mm diameter atmospheric pressure argon arc. This measurement was performed by a research group at the University of Kiel (BRD).

The data analysis was done with the numerical methods that are described in section (3.2.3).

Referring to the discussion on the errors in the determination of n_e (cf. section 3.2.3.2) we show in fig. 5.4 the variation of $\Delta n_e/n_e$ as a function of T_e.

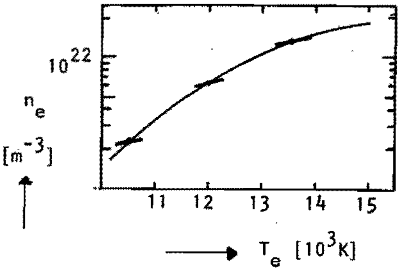

Fig. 5.4
Variation of $\Delta n_e/n_e$ *along the measured* $n_e(T_e)$ *relation; for an uncertainty in* T_e *equal to 2%.*

As is evident, the variations in n_e due to the method used, are nearly parallel to the $n_e(T_e)$ relationship. This means that small errors introduced in the determination of n_e from the source function method will hardly influence our comparisons between the experimentally determined $n_e(T_e)$ relationship and the LTE relationship as these errors in the n_e measurements propagate almost along the experimental $n_e(T_e)$ curve.

As described in section (3.2.3) also the neutral density can be determined with the source function method. Values of $n_{1,LTE}(T_e)$, $n_{1,PLTE}(T_e)$ and also $n_{1,saha}(T_e)$ are shown in figure 5.5.

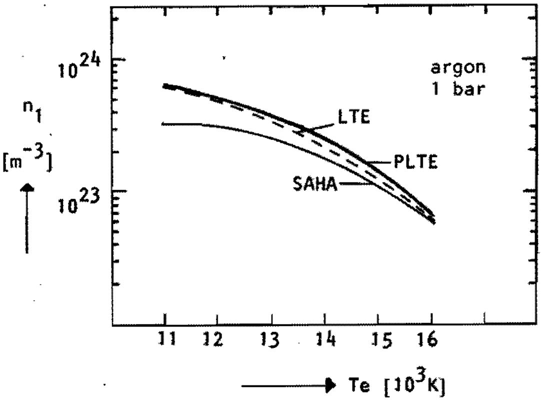

Fig. 5.5
The density of the neutral ground level as a function of the electron temperature.
PLTE : measured relationship; assumption of PLTE
LTE : LTE calculation of n_1
Saha : Values from the Saha equation (2.3) with experimental values of n_e *and* T_e.

Note that we have compared the experimental values for $n_{1,PLTE}(T_e)$ with:

1. Values of $n_{1,LTE}(T_e)$ obtained from LTE calculations of the plasma components. This is the value for the ground state density in LTE at atmospheric pressure.
2. Values of $n_{1,saha}(T_e)$ which are calculated from equation (2.3) by inserting the *experimentally* obtained values of n_e and T_e in this equation and solving for n_1.

From the comparison between $n_{1,PLTE}(T_e)$ and $n_{1,saha}(T_e)$ it can be deduced that the neutral ground level is overpopulated with respect to the Saha value. The corresponding values of $\delta b_1 = n_{1,PLTE}/n_{1,saha}-1$ can be compared with the results from our simplified 4 level model of the ArI spectrum of chapter 2.

To this end, first we will discuss the rediative and diffusive effects that contribute to δb_1 in some more detail.

5.2.1 The influence of diffusion

From the measured radial profiles of T_e and n_e, it is possible to estimate the influence of the diffusion term in equation (2.17). In the figures 5.6a and 5.6b the radial dependence of $n_e(r)$ and $n_1(r)$ are shown.

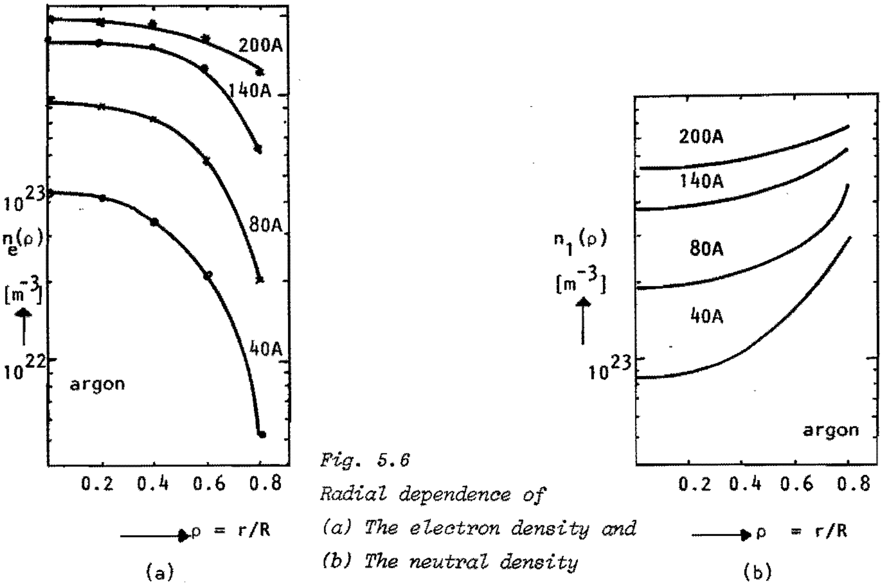

(a)

(b)

Fig. 5.6
Radial dependence of
(a) The electron density and
(b) The neutral density
Parameter is the arc current.
Argon; 1 bar; Ø 5mm arc.

From equation (2.19a) and these profiles (and the profiles of $T_e(r)$ in figure 5.2), the radial dependence of the ambipolar diffusion coefficient can be obtained. Profiles of $D_A(r)$ are shown in fig. 5.7.

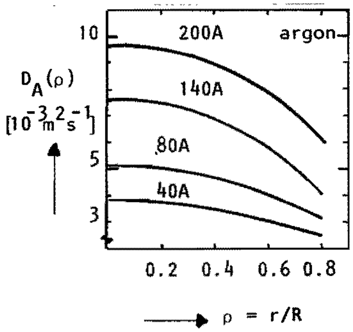

Fig. 5.7
Radial profiles of the ambipolar diffusion coefficient D_A.
Argon; 1 bar; Ø 5mm arc.

From these profiles the radial dependences of p_e and of $n_1\underline{w}_1$ are calculated (cf. equation 2.8) after fitting appropriate bi-quadratic profiles (of the form: $X(\rho)/X(0) = 1+X_1\rho_2+X_2\rho^4$; $\rho = r/R$ and for X the plasma paramter is introduced) to the relevant quantities. The fitting is done by a least-squares approximation process.
These profiles are then differentiated to yield values for the diffusion term, $-\operatorname{div}(n_1\underline{w}_1)/n_{1,saha}$ in (2.17). The radial dependence of the diffusion term is shown in figure 5.8.

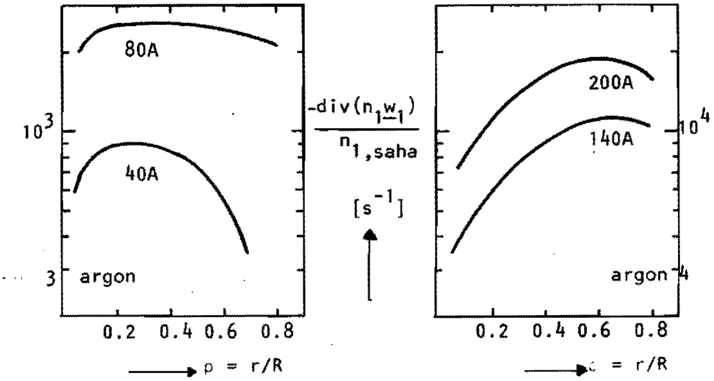

Fig. 5.8
The diffusion term of equation (2.17) as a function of the arc radius.
Argon; 1 bar; Ø 5mm arc

5.2.2 Comparison of the measured overpopulation factor δb_1 with the predictions

In figure 5.9 the overpopulation of the neutral ground level obtained from the comparison between $n_{1,PLTE}$ and $n_{1,saha}$ is plotted as a function of the temperature. These *measured* values of δb_1 will be denoted by δb_1^m.

In this figure we also show the corresponding *calculated* values, δb_1, (as function of the temperature) which follow from our simplified 4 level model of chapter 2.
In figure 5.10 the radiative contributions to δb_1 are shown (cf. equation (2.17)). The diffusion term in (2.17) has already been given in figure 5.8.

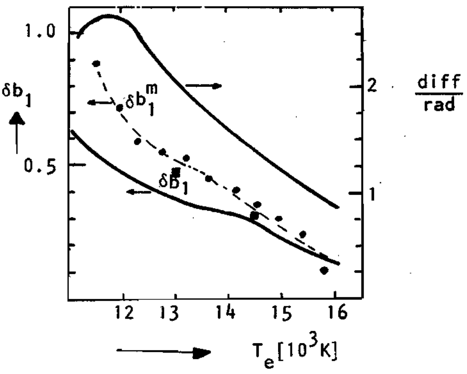

Fig. 5.9

Measured overpopulation δb_1^m (●) of the neutral ground level as a function of the electron temperature.

Also shown in this figure:

The calculated values of δb_1 using the simplified 4 level model of chapter 2 and

The ratio of the diffusive to the radiative (diff/rad) contributions to δb_1.■Results of Bober and Tankin [BOB70]

Argon; 1 bar; Ø 5mm arc.

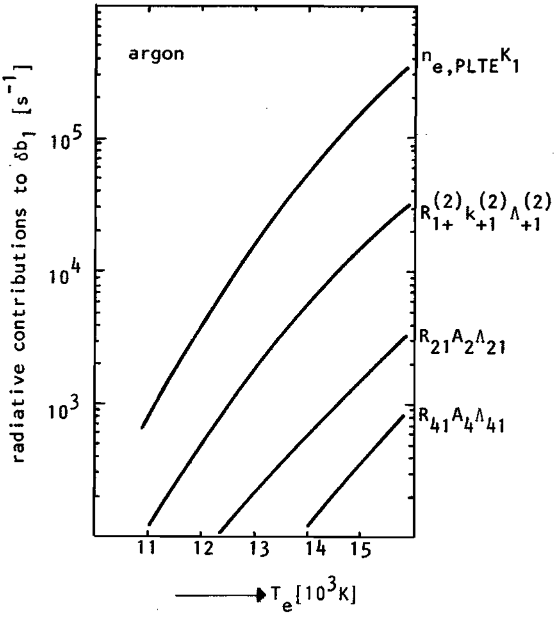

Fig. 5.10

The different radiative terms that contribute to δb_1, plotted as a function of the electron temperature (cf. equation 2.17).

The relative influence of diffusion compared to that of radiation is also shown in fig. 5.9.
For increasing values of the temperature the influence of diffusion decreases, at least on the axis, as the radial profiles become flatter.

In figure 5.11 the radial dependence of δb_1^m is shown for two values of the plasma current: 40A and 200A. In these figures also the calculated radial profiles of δb_1 are shown.

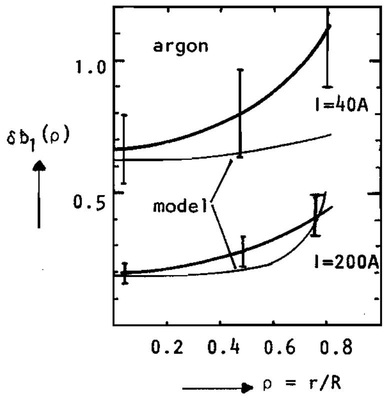

Fig. 5.11
Comparison of the experimentally determined radial dependence of δb_1^m *with the calculated dependence of* δb_1*, for two values of the arc current.*
Argon; 1 bar; Ø 5mm arc.

As expected the δb_1^m profile is flatter at the highest current. The values of δb_1 calculated with the model with diffusion and radiation prove to account reasonably for the processes that determine the establishment of at least this overpopulation near the arc axis. Further towards the wall the agreement is less. At low currents our model underestimates the overpopulation, while at the higher currents an overestimation of δb_1 results close to the wall. In both cases for the largest part of the arc cross-section the agreement between the model and the experiment is reasonable, although it seems that at low currents additional effects influence δb_1.

For comparison, 2 values obtained by Bober and Tankin [BOB70] have also been inserted in figure 5.9. The agreement with our measurements is good although also these values seem to indicate that δb_1 is underestimated by our model.

The results for δb_2 and δb_3 confirm the conclusions of section 2.2.1, i.e. $\delta b_2 \simeq 10^{-3}$ and $\delta b_3 \simeq -3\ 10^{-4}$ at $\hat{T}_e = 1\text{eV}$, so δb_2 and δb_3 are negligible.

5.2.3 *The total excitation and ionization rate coefficient for the neutral ground level*

From the measured values of δb_1, n_e, $\delta b_{1,saha}$ and the calculated diffusion flux (cf. figures 5.9, 5.3, 5.5 and 5.8 respectively) the total excitation and ionization rate coefficient can be determined from equation (2.17) (section 2.1.2).

Neglecting the contributions from resonance radiation in (2.17) (cf. figure 5.10) we obtain for K_1

$$K_1 \simeq [R_{+1}^{(2)}\ k_{+1}^{(2)}\ \Lambda_{+1}^{(2)} - \frac{\operatorname{div}(n_1 \underline{w}_1)}{n_{1,saha}}]/n_e\ \delta b_1\ [m^3 s^{-1}] \qquad (5.1)$$

Results for $K_1(T_e)$ are shown in figure 5.12. In the derivation of K_1 the PLTE relation between n_e and T_e has been used and also the $\Lambda_{+1}^{(2)}$ values from Hermann's calculations (cf. figure A.5 in appendix A).

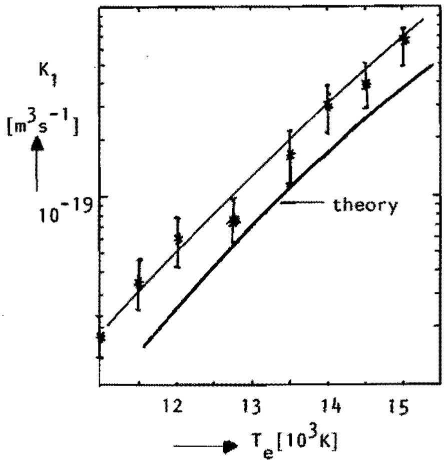

Fig. 5.12
Measured total excitation and ionization cross-section for the neutral ground state as a function of the electron temperature.
Also shown is the theoretical relation $K_1(T_e)$ from appendix A, fig. A.7.

Also shown in this figure is the theoretical relation between K_1 and T_e following Pots [POT79]. Here we have used the theoretical values divided by a factor 2.5 in accordance with the discussion on the rate coefficients of appendix A.

As can be seen the measured values are somewhat larger than the theoretical ones, even if the uncertainty in the measurments is taken into account. The important fact, however, is the agreement between threshold behaviour of the experimentally determined values of K_1 and the theoretical values.

Although the accuracy in the determination of K_1 can be improved (e.g. by better values of $\Lambda_{+1}^{(2)}$), we have demonstrated here that K_1 can be determined from a relatively simple experiment.

5.2.4 *Time constants for diffusion and for radiative recombination*

The influence of diffusion can also be compared to that of radiative recombination by comparing the relevant time constants:

For diffusion:

$$\tau_D = \frac{n_1}{\mathrm{div}\ n_1 \underline{w}_1}\ [\mathrm{s}], \tag{5.2}$$

and for radiative recombination

$$\tau_R = \frac{1}{n_e k_{+1}^{(2)}\ \Lambda_{+1}^{(2)}}\ [\mathrm{s}] \tag{5.3}$$

We take Hermann's value for $\Lambda_{+1}^{(2)}$ in equation (5.3) [HER68]

The results are summarized in table 5.2 as a function of the arc current and of the radial position:

TABLE 5.2

Time constants [s] *for diffusion and recombination*

	I=40A		I=80A		I=140A		I=200A	
r/R	τ_D	τ_R	τ_D	τ_R	τ_D	τ_R	τ_D	τ_R
0.2	$2\ 10^{-3}$	10^{-3}	$6\ 10^{-4}$	$4\ 10^{-4}$	$2\ 10^{-4}$	$1\ 10^{-4}$	10^{-4}	$0.5\ 10^{-5}$
0.4	$2.5\ 10^{-3}$	$2\ 10^{-3}$	$6\ 10^{-4}$	$4\ 10^{-4}$	$2\ 10^{-4}$	$1.5\ 10^{-4}$	10^{-4}	10^{-4}
0.6	$3\ 10^{-3}$	$4\ 10^{-3}$	$6\ 10^{-4}$	$8\ 10^{-4}$	10^{-4}	$2\ 10^{-4}$	10^{-4}	10^{-4}
0.8	10^{-1}	$2\ 10^{-2}$	10^{-3}	$3.5\ 10^{-3}$	10^{-4}	$7\ 10^{-4}$	10^{-4}	$2\ 10^{-4}$

We deduce from this table that even close to the axis of the discharge, diffusion cannot be neglected.

5.2.5 *The electrical and thermal conductivities*

In this section the values for the electrical and thermal conductivities abtained from the measured $n_e(T_e)$ relationship and the various radial profiles, are compared with values from the literature.

5.2.5.1 *The electrical conductivity*

From the measured profiles of $n_e(r)$ and $T_e(r)$ the electrical conductivity of the arc plasma is determined. The obtained values can then be compared with values of the arc conductance which follow from measurements of the electric field and current density of the arc.

The electrical conductivity $\sigma(r)$ follows from Spitzer's expression [SPI65]:

$$\sigma(r) = \frac{e^2 n_e(r)}{m_e\ \upsilon_{ei}(r) + \upsilon_{ea}(r)} \qquad (5.4)$$

In this expression, the electron-ion collision frequency is given by

$$\upsilon_{ei} = 1.8\ n_e \frac{\ln\Lambda_1}{T_e^{1.5}} \qquad [s^{-1}] \qquad (5.5)$$

with

$$\Lambda_1 = 1.25\ 10^4 \frac{T_e^{1.5}}{\sqrt{n_e}} \qquad (5.6)$$

υ_{ea} is the electron neutral collision frequency and is given by

$$\upsilon_{ea} = n_1 \langle\sigma_{ea}\ v_e\rangle \qquad [s^{-1}] \qquad (5.7)$$

where σ_{ea} is the electron atom collision cross-section.

From the values of σ_{ea} given by Devoto [DEV67] and $n_{1,PLTE}$, we calculated υ_{ea} and from the measured values of $n_{e,PLTE}$ and T_e, υ_{ei} is obtained. The results are shown in figure 5.13 as a function of T_e.

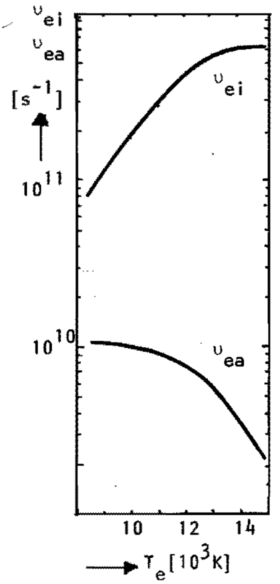

Fig. 5.13
The electron-ion and electron neutral collision frequencies, calculated with the measured values of n_e, T_e and n_1.

Note that the addition of frequencies is only admissible if $\upsilon_{ei} > \upsilon_{ea}$, thus if the electron-ion and electron-electron collisions determine the distribution function. At low current values when $\upsilon_{ea} \approx \upsilon_{ei}$ (in particular in the outer layers of the arc) expression (5.4) may overestimate the conductance even in the framework of classical plasma theory.

The arc conductance, G, is calculated from

$$G_{calc} = \frac{2}{R^2} \int_0^R \sigma(r)dr \qquad (5.8)$$

where the radial component of the electric field has been neglected.

From measurements of the arc current and electric field, experimental values for the arc conductance G_{meas} are obtained:

$$G_{meas} = \frac{I}{E\pi R^2} \qquad (5.9)$$

where I is the electric current through the arc, E the longitudinal electric field and R is the plasma radius:

Determination of G_{meas} at different values on the arc current yields the results shown in table 5.3 for a 5 mm diameter arc. In this table $\Delta G = G_{meas} - G_{calc}$.

TABLE 5.3 Comparison between the calculated and measured values of the arc conductance

I [A]	E [V/m]	$10^3 * G_{meas}$ [m/Ω]	ΔG (%)
40	790	50.6	19
80	1041	76.9	7
140	1360	102.9	6
200	1620	123.5	2

For high values of the current the measured values agree well with the values calculated using Spitzer's equation (equation 5.4), although Spitzer's expression was derived for ideal plasma's (i.e. for which the number of particles in the Debye sphere, $n_D \gg 1$) while for a thermal argon plasma $n_D \simeq 6$ at high currents (the plasma can be considered to be weakly non-ideal).

For low currents the discrepancy between G_{meas} and G_{calc} is larger. For I = 40A the temperature close to the wall is relatively low ($T_e \simeq 9500K$ at $r/R = 0.8$), $n_{e,PLTE} \ll n_{1,LTE}$, $n_{1,PLTE} > n_{1,LTE}$, $\upsilon_{ei,PLTE} \ll \upsilon_{ei,LTE}$ and $\upsilon_{ea,PLTE} \gg \upsilon_{ea,LTE}$.

In this situation $\upsilon_{ei,PLTE}$ may become comparable to $\upsilon_{ea,PLTE}$ so that Spitzer's approach, where only coulomb interactions are considered ceases to be valid.

The influence of this low temperature region which is highest at the lowest currents, decreases rapidly with increasing current and the agreement with Spitzer's results becomes better.

5.2.5.2 *A simplified expression for the thermal conductivity*

Our aim here is to derive a simple expression for the thermal conductivity κ_{th}, on the axis of the arc plasma.

To this end we make the following simplifications and assumptions:

1. The radial dependence of κ_{th} is ingnored. We restrict the conclusions to the arc axis, where the gradients in T_e are small.
2. We consider the total free bound radiation loss as the only radiation loss mechanism. Expressions for the different types of radiation losses can be found in appendix C. Values for the different contributions to the total radiation loss, for several values of the electron temperature can be found in table 5.4. As follows from this table and the discussions in appendix C, the contribution from the free-free continuum and the line radiation can be neglected.
3. Diffusion effects on the axis are also neglected. This assumption is based on the fact that the total free-bound radiation $(\bar{u}_{fb}+u_{fb}^{(1)}\,\Lambda_{+1}^{(2)}$ in table 5.4) is larger than the free-bound radiation to the ground level by a factor of 20 at T_e = 11000K and a factor of 5 at T_e = 16000K (cf. table 5.4). For the same temperature range the relative influence of diffusion compared to that of $u_{fb}^{(1)}$ decreases from a factor 2.5 to less than one (cf. figure 5.9).

   So compared to the total radiative losses the diffusion remains small.

TABLE 5.4 Radiative losses as a function of temperature

T_e	n_e	$u_{fb}^{(1)}$	$u_{fb}^{(1)}\Lambda_{+1}^{(2)}$	$\bar{u}_{fb}$	u_{ff}	u_{line}	u_{total}
$[10^3 K]$	$[10^{22} m^{-3}]$	$[Wm^{-3}$ sterad$]$					(with reabsorption of $u_{fb}^{(1)}$
11	2.6	$1.4\ 10^7$	$2.2\ 10^6$	$4.1\ 10^7$	$4.9\ 10^6$	$8.0\ 10^6$	$5.6\ 10^7$
12	5.4	$5.8\ 10^7$	$1.3\ 10^7$	$1.7\ 10^8$	$2.4\ 10^7$	$2.4\ 10^7$	$2.3\ 10^8$
13	9.2	$1.7\ 10^8$	$5.1\ 10^7$	$4.9\ 10^8$	$7.6\ 10^7$	$5.1\ 10^7$	$6.7\ 10^8$
14	13.7	$3.6\ 10^8$	$1.5\ 10^8$	$1.1\ 10^9$	$1.9\ 10^8$	$8.5\ 10^7$	$1.5\ 10^9$
15	17.0	$5.5\ 10^8$	$2.9\ 10^8$	$1.6\ 10^9$	$3.1\ 10^8$	$1.0\ 10^8$	$2.3\ 10^9$
16	19,7	$7.3\ 10^8$	$4.8\ 10^8$	$2.1\ 10^9$	$4.6\ 10^8$	$1.1\ 10^8$	$3.2\ 10^9$

From these assumptions the stationary energy balance equation(Elenbaas-Heller equation) can be written as:

$$jE = \frac{1}{r}\frac{\partial}{\partial r}[\kappa_{th}(r)\ r\ \frac{\partial T_e(r)}{\partial r}] + n_e^2(r)[k_{+1}^{(2)}E_{01}\Lambda_{+1}^{(2)} + 5.93\ 10^{-38}\ \hat{T}_e^{-0.27}] \qquad (5.10)$$

In this equation the second term on the right represents the total free bound power loss (cf. appendix C). The radial dependence of the factor between brackets will be ignored.

The first term on the right symbolizes the power loss by heat conduction and the left hand side is the power input to the arc.

Now we integrate equation (5.10) over the arc radius. For the temperature profiles of $T_e(r)$, $n_e(r)$ and $j(r)$ we take Gaussian profiles:

$$T_e(r) = T_{e0} \exp(-\frac{r^2}{\sigma_{T_e}^2}) \quad (5.11)$$

$$n_e(r) = n_{e0} \exp(-\frac{r^2}{\sigma_{n_e}^2}) \quad \text{and} \quad (5.12)$$

$$j(r) = j_0 \exp(-\frac{r^2}{\sigma_j^2}) \quad (5.13)$$

Note that these Gaussian profiles ~~need only~~ to describe the functions in the central region of the arc cross section. Because of this, the Gaussian effective widths (σ_{T_e}, σ_{n_e} and σ_j) may be much larger than the radius of the arc.

With the approximation $\sigma_j \simeq \sigma_{T_e}$ and $\sigma_{n_e} \simeq \sigma_{T_e}$ we obtain from (5.10) after integration:

$$\kappa_{th} \simeq \frac{Ej_0 - n_{e_0}^2 \{k_{+1}^{(2)} E_{01} \Lambda_{+1}^{(2)} + 5.93\ 10^{-38}\ \hat{T}_e^{-0.27}\}}{4T_{e0}} \sigma_{T_e}^2 \quad (5.14)$$

This is a simple approximation for κ_{th} as a function of T_e the results of which are shown in figure 5.14

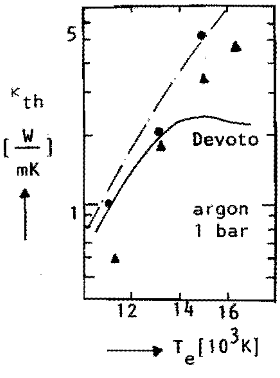

Fig. 5.14
Temperature dependence of the thermal conductivity for argon.

▲ *This thesis*

● *Kopainsky [KOP71]*

−.− *Approximation to results of other authors (cf. [DEV73])*

In this figure we have also plotted the theoretical curve of Devoto [DEV73] and some experimental values of Kopainsky [KOP71].
The values from our approximate expression for κ_{th} lie in between the results from these two authors.
Also shown in this figure is a line which is an approximation to results of measurements on κ_{th} obtained by different authors (cf. [DEV73] for the references). Our values agree quite well with these measurements.

5.3 Results from the interferometry

With the interferometric set-up of chapter 4, values of n_e were obtained as a function of the arc current.
The accuracy of these results on n_e is better than for the spectroscopic results and for the measurements presented here it is about 3%.
The dominant factor for the accuracy in these measurements is the uncertainty in the arc length. Only when measurements with different values of the arc length have been performed, the accuracy can be improved. Our results are based on measurements with two different arc lengths.
Figure 5.15 shows the results as a function of the arc current.
Also shown in the figure are measurements by Nick[NIC79] and results from the spectroscopic methods. As can be seen the agreement is good.

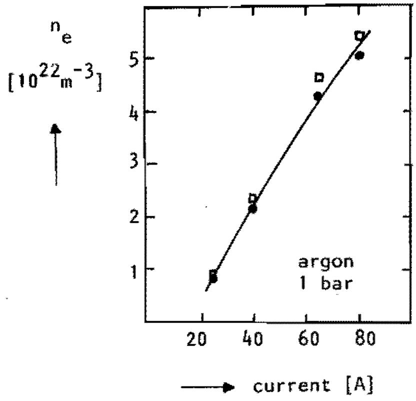

Fig. 5.15
Comparison of values of the electron density determined by
- ● *2 wavelength H_eN_e interferometry; this thesis*
- □ *Spectroscopic methods; this thesis*
- – *Nick [NIC79]*

We note here that as the accuracy in the interferometric results is better, these results can be used in conjunction with figure 5.3 to obtain a precize temperature determination. As has been stated before (section 5.2) the $n_e(T_e)$ relationship is rather unsensitive to small errors in the measurement procedure. So, because the $n_e(T_e)$ dependence is known (figure 5.3) the use of accurate values of n_e in this figure can yield accurate values of T_e.

CHAPTER VI FIRST RESULTS OF THE PULSED EXPERIMENTS

6.1 Introduction

In this chapter we present the first results obtained from the pulsed current experiment that has been described in chapters III and IV. One of the important features of a pulsed experiment is the possibility to achieve substantially higher values of electron density and temperature during a (positive) current pulse, without having to resort to a high power current supply and cooling system.

The results of such an experiment can provide additional information about time-constants involved with the establishment of equilibrium in a plasma. Of importance is also, to know which processes determine these time-constants [PIE78].

The time varying characteristics of thermal plasmas can provide important additional information concerning the dynamic properties of devices based on electric arcs that are used in industrial processes, e.g. in plasma arc spraying and in arc switching [VAE81].

Usually the study of time dependent effects is performed in decaying plasmas [KAF79, VAC76, CAC76].

The time variation of the plasma parameters after application of a current pulse was studied by Pierstorff [PIE78]. In his study the rise time of the applied current pulse is relatively slow (> 15 μs) and the maximum pulse amplitude does not exceed 100A.

Here we will report on the first results obtained after application of a current pulse with an amplitude of about 250A and a rise-time of less than 2 μs.

We will limit ourselves to a discussion of the total energy balance equation and of the continuity equation for the electrons. Our main aim is to investigate under which conditions the arc plasma can be considered as quasi-stationary during the pulse.

Secondly, we will try to obtain information about some processes that determine the establishment of PLTE.

6.2 Some considerations about the heat and mass balance equations

We investigated the time development of the arc parameters under the following assumptions:

1. PLTE is maintained throughout the pulse at a value of the pressure that is equal to the stationary value (1 bar in our case).
2. The energy balance is governed by the increase of the internal energy of the plasma and the change of Joule dissipation, which increases much faster than the temperature.
3. Finally we have limited our discussions to the first 60 μs of the current pulse (which is of 500 μs duration). Under these conditions transport processes can be neglected.

We will discuss the second of these assumptions to some more detail here.

6.2.1 Pressure changes during the current pulse

We ignore particle fluxes at the on-set of the current pulse (t=0). Denoting the change of electron and neutral densities by Δn_e and Δn_1,

$$\Delta n_e = n_e(t) - n_{e0} = - \Delta n_1 \quad , \tag{6.1}$$

we obtain in first approximation for the pressure change:

$$\frac{\Delta p}{p_0} \simeq \frac{\Delta n_e}{2n_{e0}+n_{10}} + \frac{\Delta T_e}{T_{e0}} \tag{6.2}$$

Here the subscript 0 denotes values at t=0.

Anticipating the results on the temperature and density changes during the pulse, we will use the measured values of $n_e(t)$ and $T_e(t)$ to estimate the pressure change.

For a 8 mm diameter argon arc at atmospheric pressure with stationary current I=100A, these values are:

$n_{e0} \simeq 8.10^{22}$ m^{-3}, and $T_{e0} \simeq$ 12700K, and

n_e(t=60µs) $\simeq$ 1.77 10^{23} m^{-3}, T_e(t=60µs) $\simeq$ 14950K.

After insertion of these values in (6.2) a pressure change $\Delta p/p_0 \simeq 35\%$ is obtained.

This pressure change will not be reached in reality, due to the large volumes of cold argon gas that surround the plasma, and which will cause a reduction of the pressure rise.

In fig. 6.1 we have sketched part of the arc chamber, showing the volumes between the cascade plates and the silicone sealing rings, and also the large volumes at the ends of the plasma.

The magnitude of the respective volumes is also given in the figure, together with the plasma volume of a 8 mm diameter 56 mm long arc (these are the diameter and length of the arc that was used for this experiment).

From this figure we expect damping of the initial pressure jump:

1. Due to the volume of the gas between the plates that surrounds the plasma.

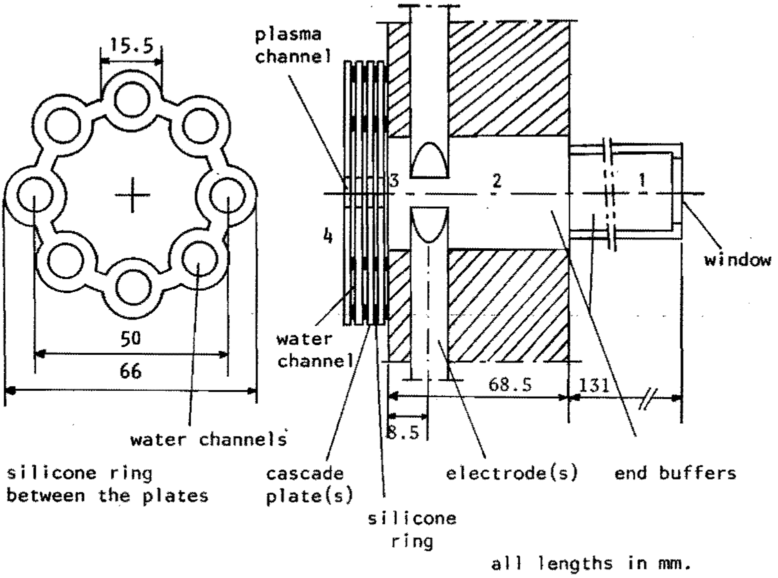

Fig. 6.1
Illustration of part of the arc vessel showing the different volumes of cold argon gas that surround the arc plasma (cf. fig. 4.9).
$V_1 = 70.4\ cm^3$; $V_2 = 43.6\ cm^3$; $V_3 = 4.7\ cm^3$; $V_{4total} = 7\ cm^3$; $V_{plasma} = 2.8\ cm^3$.

The ratio of the plasma volume to the total surrounding gas volume is roughly 1/3. Accordingly the initial pressure jump will be attenuated by a factor of 3 within a time of about $2R/v_{accoustic} \approx 4\ \mu s$ ($R = 4.10^{-3}$ m; $v_{accoustic} \approx 2000$ m/s; at the plasma temperature.

2. By the gas volume in the end buffers.

   These cilindrical prolongations of the arc vessel can be regarded as accoustic resonators (with low Q-factors) coupled to the plasma. The effect of these buffers is the reduction of the initial pressure jump to a substantially lower value (less than 5%). In addition the pressure shock front bounces back and forth in the buffer cilinders, with a period of about 300 ms ($v_{accoustic}$ is much lower due to the low value of the temperature in these buffers). These oscillations are not pronounced in the plasma due to the bad coupling efficiency from the buffers to the plasma channel.

Fig. 6.2 shows an oscilloscope trace of the time variation of the pressure pulse registered with a pressure transducer (Kistler type 603B). This pressure transducer was placed in one of the end buffers of the arc container.

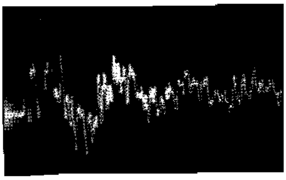

Fig. 6.2
Pressure fluctuations in one of the end buffers of the arc chamber.
The zero level corresponds to the stationary pressure of 1 bar.
Vert. scale: 20 mbar/div ; Hor. scale: 500 μs/div.

The duration of the pulse is about 1 horizontal division in the picture. As can be seen, the maximum pressure does not exceed ~0.06 bar. Additionally, the pressure oscillations in the cold gas end buffers of the arc can be observed. This change of the arc pressure, which from the observations does not exceed about 5%, will be neglected.

6.2.2 *Energy balance and mass balance equations*

Since we pulse the system to currents much higher than the initial current we may expect electron densities much higher than the initial density. Such a strong and sudden change of the density causes a $\frac{\partial n}{\partial t}$ which is much larger than the stationary $\nabla \cdot n\underline{w}$ terms. This can be observed by comparing the experimental $\frac{\partial n}{\partial t}$ values from fig. 6.4 with the stationary diffusive flows discussed in chapter V. Similarly the increase in the internal energy is also much larger than the heat diffusion term. This enables us to study the time dependent mass- and energy balances without having to know the profiles. So we will analyse the first part of the rise of the pulse by using the simple energy balance in which the radiative loss is retained even though also this term should be small:

$$E_{01} \frac{\partial n_e}{\partial t} \approx j.E - Q_{rad} \tag{6.3}$$

The left hand side represents the change of internal energy of the plasma, the first term on the right is the joule energy input, and the term Q_{rad} represents radiative energy losses. [MIT73]

Furthermore we have ignored the effect from possible differences between the heavy particle temperature and T_e. These differences are equalized by electron-ion and ion-atom energy exchanges. The time constants for these processes have been calculated [STE79]. The temperature difference between T_e and T_i is equalized with a time-constant of less than 1μs.
The slower time-constant for the equalization of T_i and T_a is of the order of 10μs for the parameter range in our measurements. These values are in accordance with the results of Pierstorff [PIE78], after extrapolation to higher values of the electron density (pulse current).
A discussion of the continuity equation was given in section 2.2.3, where

the overpopulation of the excitation equilibrium was briefly discussed. We will use the result obtained for dn_1/dt under the following assumptions:

1. Transport processes are neglected.
2. Radiation loss is limited to recombination radiation to the ground state.
3. All overpopulations of levels other than the ground state level are neglected.

Then equation (2.9) can be rewritten as:

$$\frac{\partial n_1}{\partial t} = - \frac{\partial n_e}{\partial t} = n_e \, n_{1saha} \, \delta b_1 \, K_1 + n_{1saha} \, R^{(2)}_{1+} \, k^{(2)}_{+1} \, \Lambda^{(2)}_{+1} \qquad (6.4)$$

or with the notation (2.7)

$$\frac{\partial n_e}{\partial t} = n_e n_{1saha} \, \delta b_1 \, K_1 - n_e^2 \, k^{(2)}_{+1} \, \Lambda^{(2)}_{+1} \qquad (6.4a)$$

In order to discuss equations (6.3) and (6.4a) to some more extent, we will first present some preliminary results of the pulsed experiment.

6.3 The first results of the pulsed experiments

The electron temperature was determined from time dependent measurements, of the intensity of the 696.5 nm argon neutral line. We used the source function method, in the way that was described in section 3.2.4, for time varying conditions. Fig. 6.3 is a picture of the intensity modulation of the spectral radiation at 696.45 nm. In this figure, both $I_{\lambda,1}(t)$ and $I_{\lambda,2}(t)$ (cf. section 3.2.4) are shown.

The time resolved measurements were done at one fixed value of the wavelength, end-on along the arc axis.

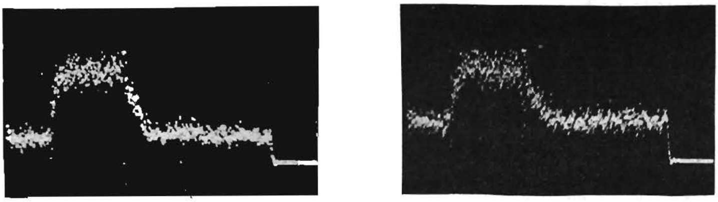
(a) (b)

Fig. 6.3
Time dependent intensity variations at a wavelength position in the profile of the ArI line 696.5 nm (λ = 696.45nm; apparatus width ~0.04nm). In this figure both $I_{\lambda,1}(t)$ -(a)- and $I_{\lambda,2}(t)$ -(b)- are shown (cf. section 3.2 and fig. 4.4).
Vert. scale: relative units
Hor. scale: 204.8 μs/div (1024 samples; 2μs/sample)

The electron density was determined interferometrically, with the same set-up that was described in chapter 4.

From these and other similar recordings we determined time constants for the intensity decay after the pulse which range from 40 μs to 60 μs. These values agree reasonably with the value of 43.6 μs determined by Baessler and Kock [BAE79] in the afterglow of a 4mm atmosphéric argon arc (decaying from a lower stationary value of the current).

The time variation of $n_e(t)$ and $T_e(t)$ obtained for a 8 mm diameter arc at atmospheric pressure with a stationary value of the current of 100A, and pulsed to about 350A, is shown in fig. 6.4.

In this figure we show $n_e(t)$ and $T_e(t)$ for the first 60 μs after pulse application.

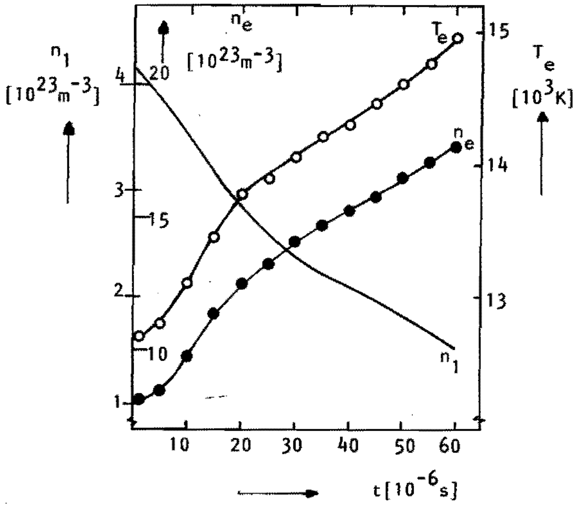

Fig. 6.4
Time dependence of T_e, n_e and n_1 for the first 60μsec after pulse application.

The rise-time of the pulse is about 2 μs, and is much faster than the rise in the electron temperature and density.

Using these results, and values of the electrical conductivity taken from Devoto [DEV73] (see fig. 6.5) the relevant terms in (6.3) and (6.4a) can be estimated.

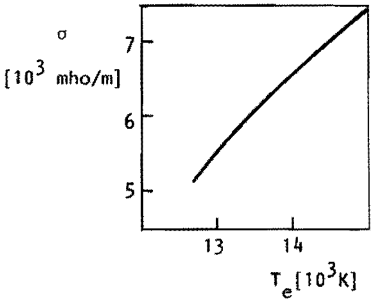

Fig. 6.5
Electrical conductivity as a function of the electron temperature for an atmospheric pressure argon arc after Devoto [DEV73].

In fig. 6.6 the rise of Joule energy input to the arc is shown together with the rise of the internal energy.

As is evident from this figure, the internal energy does not attain the same level as the level of the power input. The difference, which can be attributed partly to radiative losses is also shown as a function of time in this figure; note that heat diffusion is expected also to contribute.

For comparison, the expected free-bound radiation loss is also shown in this figure. As can be seen, the radiation loss is of the same order as the difference between joule energy input and increase of internal energy.

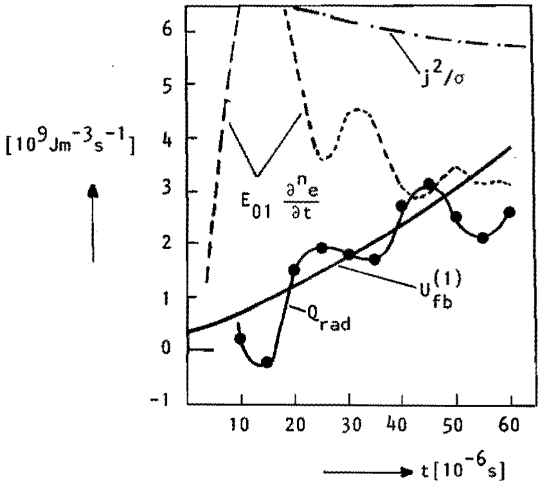

Fig. 6.6
Different contributions to equation (6.3) as a function of time.

Using the values of $n_e(t)$ shown in fig. 6.4, and values for $n_1(t)$ derived from the PLTE relationship, the time dependence of $K_1(t)$, the total excitation and ionization cross-section can be estimated from (6.4a).

The result is shown in fig. 6.7 where the results obtained from the stationary measurements, and the theoretical values have also been plotted.

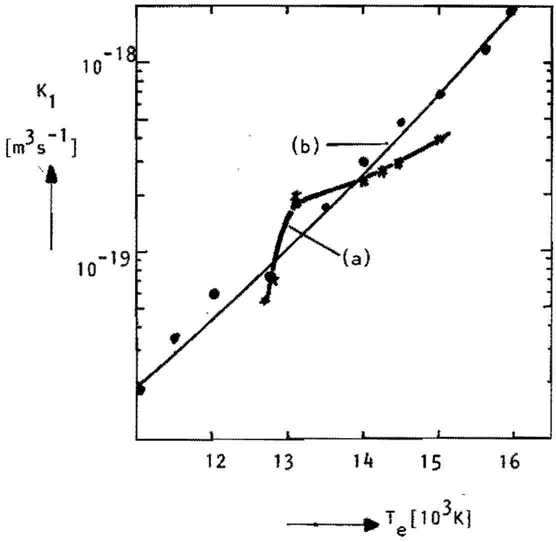

Fig. 6.7
Comparison of values of the total excitation cross-section K_1 as a function of T_e. Curve (a) from the pulsed experiments (b) from the stationary measurements.

The experimental values of $K_1(t)$ determined in this way agree reasonably with the stationary determination of K_1. For longer times after the rise of the current, a departure from the stationary values is observed. This effect indicates that transport processes cannot be completely neglected especially not towards the end of the pulse, as is to be expected.

We conclude from these observations that the power input to the arc during the current pulse causes an increase of the internal energy of the arc, and that the electron temperature rise is determined by this process.

Part of the power is lost due to recombination radiation, while also transport processes cannot be neglected as the processes evolve in time.

CHAPTER VII. CONCLUDING REMARKS

1. Deviations from Local Thermal Equilibrium (LTE) can be measured by the source function method, even for systems where these deviations are small.

2. The deviations from LTE for the argon neutral system are mainly caused by radiative recombination to the neutral ground level and by inward diffusion of neutrals.

   Radiative recombination is more pronounced at high values of the temperature, while diffusion effects dominate at low values of the current.

   The observed deviations from LTE of the ground level density are in fair agreement with the deviations predicted by a model in which diffusion and radiative recombination are assumed to be the major causes of the non-equilibrium in the neutral system.

3. With the source function method the electron temperature (T_e) and density (n_e) have been determined. The relationship between n_e and T_e appears to be independent of the radial position in the arc.

4. An accurate determination of T_e can be obtained by the following procedure:
   1. A measurement of n_e using an interferometric method;
   2. a derivation of T_e from this value of n_e with the $n_e(T_e)$ relationship obtained with the source function method.

5. The influence of the apparatus profile on the obtained results can be taken into account by:
   1. Numerical convolution of a trial profile with the measured apparatus profile;
   2. Fitting the obtained profile to the measured profile by a least squares approximation procedure.

   With our method the trial profile can be generated from the basic plasma parameters. Accordingly, by the least squares approximation procedure a direct determination of the plasma parameters is obtained with good accuracy.

6. By repetitive current pulsing the electron temperature and density of the plasma can be increased substantially without the need of large power supplies and extensive cooling systems.
   With the methods described in this thesis the characteristics of such a plasma can be studied with high precision.

7. The determination of plasma transport properties requires an accurate knowledge of the equilibrium state of the plasma.
   From the measured values of electron density and temperature we have obtained values of the heat conductivity and the electrical conductivity which are in good agreement with theoretical predictions.

APPENDIX A*

Relevant data for the Argon I simplified model

The aim of this appendix is to supply additional information and numerical values relevant to the simplified 4 level model of the argon neutral spectrum discussed in chapter two. A diagram of this model is given in figure A.1, while the energy values considered are given in table A.1.

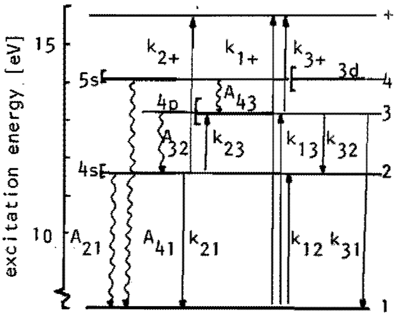

Fig. A.1
Diagram of the simplified 4 level model of the argon neutral spectrum showing the considered collisional (→) and radiative (⇝) transitions (cf. figure 2.2).

*Note: In this appendix, the following additional notations are used:

σ for cross-section ($[m^2]$).
$<\sigma v>$ for rate coefficients ($[m^3 s^{-1}]$)
k_{pq} for $<\sigma v>$ with the specification of the transition $p \rightarrow q$
$K_m = \Sigma_l k_{lm}$

Furthermore, the subscript L denotes the Lorentzian part of a line profile and D the Gaussian part

Table A.1: Considered levels with the corresponding energy ranges and values for the effective energy and statistical weight

			Effective energy (eV)	Range of energies (eV)	Statistical weight
Ground level	$3p^6$	(1)	0	0	1
Excited levels	4s	(2)	11.652	11.548-11.828	12
	4p	(3)	13.171	12.907-13.480	36
	3d+5s	(4)	14.094	13.845-14.304	60+12
Ion ground levels	$3p^5$		15.759	15.759 and 15.936	4 and 2

The rates for electron (de) excitation between the sublevels within a group are very large. An estimate yields rates for (de) excitation, $n_e<\sigma v_e>_{exc}$, which are significantly larger than $n_e<\sigma_{exc} v_e> \approx 10^{22} \cdot 10^{-12} = 10^{10} \text{sec}^{-1}$. Because of this strong coupling it is justified to consider effective levels instead of all the sublevels. The energy, E_q^{eff}, of an effective level q composed of sublevels j can be obtained from:

$$E_q^{eff} \equiv \frac{\sum_j g_{q_j} E_{q_j}}{\sum_j g_{q_j}} = \frac{\sum_j g_{q_j} E_{q_j}}{g_q} \qquad \text{(a.1)}$$

where E_{q_j} is the energy and g_{q_j} is the statistical weight of sublevel j. The sum of the statistical weights of the sublevels is the total statistical weight g_q.

The transition probabilities for transitions between effective level q and effective level p, A_{qp}, can be obtained from the individual transition probabilities, $A_{q_jp_i}$ for transitions between the sublevels q_j and p_i as follows [POT78]:

$$A_{qp} \equiv \sum_i \frac{\sum_j g_{q_j} A_{g_jp_i}}{\sum_j g_{q_j}} \qquad \text{(a.2)}$$

The effective transition probabilities are given in the following table, table A.2. (A_{qp} is given in units of 10^7 sec^{-1}) [WIE69]

qp	levels	λ_{eff}(nm)	A_{qp}	$\Delta\lambda_{\text{Stark}}$(nm)	$\Delta\lambda_{\text{Doppler}}$(nm)	$\Delta\lambda_{\text{resonanc}}$(nm
4-1	$(3d+5s)_{\text{eff}}-3p^6$	88	2.90	$10^{-4}\hat{n}_e$	10^{-3}	4.10^{-6}
2-1	$4s[^3/2]^\circ \quad -3p^6$	104.8	15.73	$5.10^{-5}\hat{n}_e$	1.310^{-3}	2.10^{-5}
2-1	$4s[^1/2]^\circ \quad -3p^6$	106.7				
3-2	$4p_{\text{eff}} - 4s_{\text{eff}}$	817.3	3.644	$5.10^{-3}\hat{n}_e$	10^{-2}	3.10^{-4}
4-3	$(3d+5s)_{\text{eff}}-4p_{\text{eff}}$	1343.0	1.27	$7.10^{-3}\hat{n}_e$	2.10^{-2}	2.10^{-4}

Table A.2: Effective spectral line wavelengths, transition probabilities and line widths of the considered levels

In the same table the corresponding Stark widths are given for an electron temperature of $\hat{T}_e = 1.0$eV, proportional to $\hat{n}_e$ ($\hat{n}_e$ in units of 10^{22} m^{-3}). Also the Stark widths are weighted over the sub-transitions:

$$\Delta\lambda_{qp} = \sum_i \frac{\sum_j g_{q_j} A_{q_jp_i} \Delta\lambda_{g_jp_i}}{\sum_j g_{q_j} A_{g_jp_i}} \qquad \text{(a.3)}$$

The procedure of averaging of the radiative transitions is only adequate for optically thin lines. For resonance lines, which are optically thick (optical depth > 1000), a more adequate procedure is to consider separate lines, calculate the escape factor and then average the $\Lambda \cdot A$-values over the group considered.

Radiation trapping

For the determination of the effective radiative lifetimes we must also take into account the effect of radiation trapping. Though, as mentioned above, this has to be considered before summing over the transitions between the sublevels, taking into consideration the corresponding Stark widths, we have worked with effective levels, transition probabilities and Stark widths. As mentioned above this procedure is good enough for our purpose, since the coupling between the levels is large and we are only interested in estimates of the radiation losses.

In an extension of the treatment by Klein [KLE69], Batenburg [BAT81] has obtained the trapping corrections (Holstein factors) for Voigt emission profiles for the plasma at the axis of a cylindrical discharge. In this treatment it is assumed that absorption and emission profiles can be described by the same Voigt profiles and that the radial dependences of the densities of the lower and upper levels of the transitions are weak. The result is given in fig. A.2, where the trapping coefficient, Λ_{qp}, is given as a function of the effective optical depth $\bar{\kappa}\bar{R}$. This quantity is defined as:

$$\bar{\kappa}\bar{R} = \frac{\sqrt{\ln 2}}{4\pi\sqrt{\pi}} \frac{\lambda_{qp}^{4}}{c\Delta\lambda_{qp}} \frac{g_q}{g_p} A_{qp} \bar{n}_p \mu R \qquad (a.4)$$

where $\Delta\lambda_{qp}$ is the half width (FWHM) of the emission profile, $\bar{n}_p$ is the averaged number density of the lower state and μ is a geometrical constant. This constant varies between $1<\mu<1.4$ for several assumptions on the radial dependence of n_p, [BAT81, KLE69]. For our treatment we have assumed that $\mu \simeq 1.2$. For $\bar{\kappa}\bar{R} >> 1$ we find for the escape factor of the axial plasma:

$$\Lambda(\bar{\kappa}\bar{R}) \simeq \sqrt{\frac{\sqrt{\ln 2}}{\sqrt{\pi}\,\bar{\kappa}_L \bar{R}}} = \sqrt{\frac{4\pi c \, g_p \, \Delta\lambda_L}{g_q \, A_{qp} \, \bar{n}_p \, \lambda_{qp}^{4}}} \qquad (a.5)$$

where $\bar{\kappa}_L$ and $\Delta\lambda_L$ are the quantities taking only the Lorentzian part of the line profile into account.

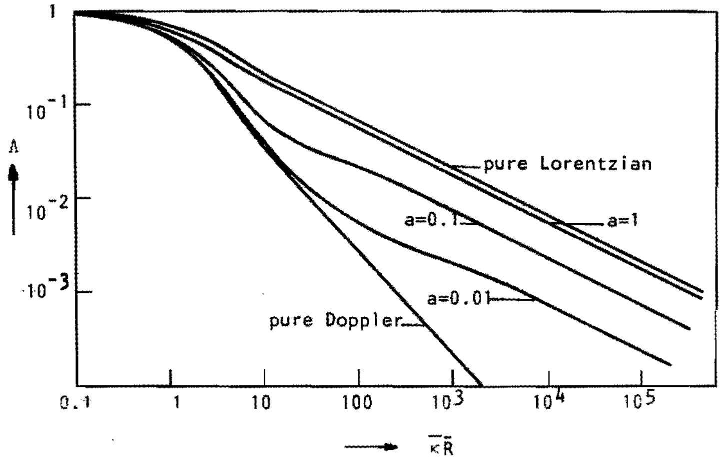

Fig. A.2
The trapping coefficient for line radiation as a function of the optical depth. In this figure the line profile is considered to be a Voigt profile.
$a = \sqrt{\ln 2}\,(\Delta\lambda_L/\Delta\lambda_D)$.

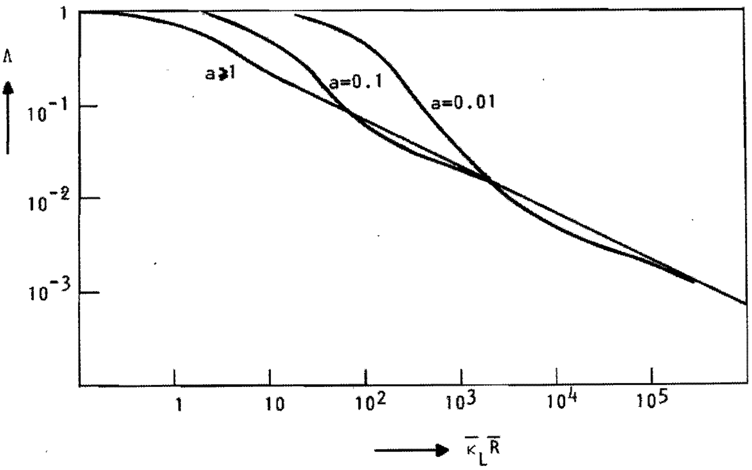

Fig. A.3
The trapping coefficient for line radiation in the case of a Lorentzian line shape.
$a = \sqrt{\ln 2}(\Delta\lambda_L/\Delta\lambda_D)$.

This approximation is valid provided that $\frac{\Delta\lambda_L}{\Delta\lambda_G} \geq \frac{100}{\bar{\kappa}\bar{R}}$ as can be observed from fig. A.3 where $\Lambda(\bar{\kappa}_L\bar{R})$ is given as a function of $\bar{\kappa}_L\bar{R}$

Note, that if the absorption is strong, this approximation is valid even if the Lorentzian width is smaller than the Gaussian width.

In table A.2 we have given several values of the relevant resonance lines in the ArI system.

* * *

We observe that the approximation given in eq.(a.5) is valid within a factor of 1.5. We also note, that as far as the Lorentzian part is concerned the Stark broadening dominates.

So, the effective transition probability for resonant transitions, including the trapping effect, can approximately be written as:

$$A_{qp}\Lambda_{qp} \simeq A_{qp}\sqrt{\frac{4\pi c\, g_p\, \Delta\lambda_L}{\lambda_q A_{qp}\, \bar{n}_p\, \lambda^4_{qp}}} = \alpha_{qp}\sqrt{\frac{n_e}{n_1}} \qquad (a.6)$$

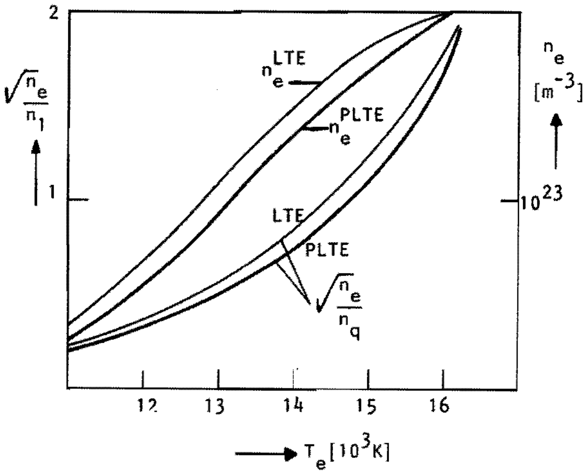

Fig. A.4

The ratio $\sqrt{n_e/n_1}$ *and the electron density as functions of the electron temperature, for both the LTE and the PLTE situation (argon; 1 bar)*

In fig. A.4 the quantity $\sqrt{\frac{n_e}{n_1}}$ and the density n_e are plotted as functions of the temperature, both under assumption of LTE. Also indicated is the variation of these quantities if we take the experimental PLTE-results of chapter 5.

We observe, that for the treatment here the quantity $A_{qp}\ \Lambda_{qp}$ is roughly proportional to n_e for temperatures between 8000K and 15000K. Above 15000K the quantity $\sqrt{n_e/n_1}$ increases faster than linearly with n_e. So at these temperatures the influence of radiation escape will again increase.

For the optically thick resonant lines also the radiative term is approximately proportional to the electron density, as is the collisional term. This is valid provided that the line is sufficiently optically thick and provided that the ratio of Lorentzian and Gaussian widths is larger than $100/\overline{\kappa R}$.

Note, that this does not mean that the line must be dominantly Lorentzian. In fact, for the resonance lines in ArI the Lorentzian widths are of the same order of magnitude as the Gaussian widths.

Radiation trapping of nonresonant lines

Radiation trapping of nonresonant lines of the ArI-system needs only to be considered for the 4p-4s transitions. Even for these lines, which represent the dominant line radiation, the optical depth is only of the order of the radius, so $\overline{\kappa R} \sim O(1)$.

These lines are dominantly Stark broadened, so we can ignore the Gaussian part, and treat the lines as Lorentzian lines. Furthermore, the densities of both the upper and lower states of the transition decrease with increasing radius. From fig. A.2 we can see that for most conditions this factor is still close to 1, so that we will ignore radiation trapping in this treatment for all the transitions but the resonant transitions.

Radiative recombination

Radiative recombination is the inverse proces of photo ionization. Cross-sections of the latter proces can be found in the literature.
We have followed the analysis of Katsonis [KAT76] who assumes a photo-ionization cross-section:

$$\sigma_{+1}^{(2)} = 3{,}5.10^{-21} m^2 \tag{a.7}$$

This value, obtained with the application of the principle of detailed balancing is in agreement with the value found by Trommer from measurements of the freebound emmissivity [TRO81].

This value for the photo ionization cross-section leads to the radiative recombination coefficient $k_{+1}^{(2)}$ (cf. eq. 5).

$$k_{+1}^{(2)} \simeq 0.995\ \hat{T}_e^{-0.17} \quad m^{-3}\ s^{-1} \tag{a.8}$$

As far as radiative recombination to excited states is concerned only experimental information on the metastable states is available. Following Katsonis, we will assume for the other states hydrogenic values.

$$k_{+2}^{(2)} \simeq 1.5\ 10^{-20} \qquad m^{-3}\ s^{-1} \tag{a.9}$$

$$k_{+3}^{(2)} \simeq 2.5\ 10^{-21} \qquad m^{-3}\ s^{-1} \tag{a.10}$$

Radiation trapping is only important for the free-bound radiation to the ground state. The calculation of the effective energy loss is complicated because of the radial dependence of both the emissivity ($\sim n_e^2$) and the absorption coefficient ($\sim n_1$). The first quantity decreases with increasing radius, the second increases with increasing radius. Furthermore, the optical depth is of the same order of magnitude as the radius. In a cylindrical geometry one must expect in this case that for the central plasma a significant part of the radiation escapes. This radiation is trapped in the outer layers. As there the local emissivity is much smaller, this may lead to energy gain in the outer layers instead of radiative energy loss.

Instead of solving the problem ourselves, we will briefly outline the results of an extensive treatment by Herrman [HER68]. In this paper the local escape factor is calculated numerically under the assumption of LTE. The results obtained for a cylindrical arc with a diameter of 5 mm and at atmospheric pressure are given in fig. A - 5a and b.
In this figure we have plotted the escape factor for the axial part of the plasma as a function of the temperature (fig. A.5a) and also the radial dependence of $\Lambda_{+1}^{(2)}$ (fig. A.5b).

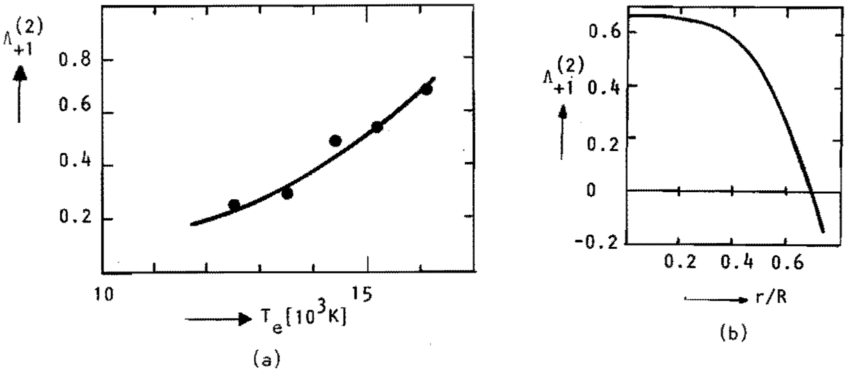

Fig. A.5
(a) The trapping coefficient for recombination radiation as a function of the electron temperature, as calculated by Hermann [HER68].
(b) Radial dependence of $\Lambda_{+1}^{(2)}$ *for a Ø5mm arc at atmospheric pressure [HER68].*

In this study the results are formulated in terms of an escape factor, which for this case will be negative in the outer layers of the plasma. In the calculation LTE is assumed; in reality there will prove to be small deviations from LTE. This means that these results overestimate slightly the radiative escape.
It can be concluded that over the full range of parameters the escape factor varies from 0.2 - 0.6. So, in the calculation we will use these numbers.

Finally we will note in this respect, that in this calculation no allowance is made for the radiation with wavelengths longer than the free-bound edge. From measurements of Hofsaess [HOF78] we can show that there is a significant addition with wavelengths longer than the free-bound limit. This radiation will be less effectively reabsorbed, so in this respect the above quoted treatment ove estimates the reabsorption.

Excitation and ionization rate coefficients

Several approaches have been followed in the literature to obtain expressions for excitation rates. The first is entirely empirical; the measured dependence of $\sigma(E)$ is described by a simple analytical formula which is integrated over velocity space to obtain the rate coefficient $<\sigma v>$. A Maxwellian velocity distribution is assumed. A very simple but typical example is illustrated in fig. A.6, where $\sigma(E)$ is assumed to increase linearly from treshold.

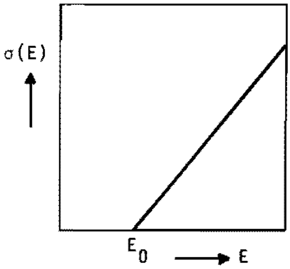

Fig. A.6
Simplified threshold behaviour of $\sigma(E)$.

$$\sigma(E) = \left(\frac{d\sigma}{dE}\right)_{treshold} \cdot (E - E_{treshold}) \qquad \text{(a.11)}$$

This behaviour appears also from beam experiments [LLO72], [CON73] and [ZAP73].

In this case one obtains for a Maxwellian distribution:

$$k_{pq} = \left(\frac{8kT_e}{\pi m_e}\right)^{\frac{1}{2}} \frac{d\sigma}{dE}\ kT\ \left(2 + \frac{E_{pq}}{kT_e}\right)\ \exp\left(-\frac{E_{pq}}{kT_e}\right)\ [m^3 s^{-1}] \qquad \text{(a.12)}$$

This formula is only useful if the kinetic energy of the electrons kT_e is much smaller than the treshold energy for excitation E_{pq}. In that case the treshold behaviour of $\sigma(E)$ determines entirely the behaviour of $<\sigma v>$ as function of the temperature.

For the excitations from the ground state $3p\text{-}4s^{met}$, $3p\text{-}4p$, we have used this expression with the following numerical values ($4s^{met}$: metastable levels of the 4s-group; $4s^{res}$: resonant levels of the 4s-group).

Table A.3: Values of dσ/dE for the different transitions

	$E_{treshold}$ (eV)	dσ/dE	dσ/dE
$3p\text{-}4s^{met}\ {}^3P_2 + {}^3P_0$	11.58 eV	$2.26\ 10^{-22}$ 1) m^2/eV	$1.41\ 10^3\ m^2/J$
$3p\text{-}4s^{res}\ {}^1P_1 + {}^3P_1$	11.78 eV	$1.26\ 10^{-22}$ 2) m^2/eV	$0.79\ 10^3\ m^2/J$
$3p\text{-}4s^{tot}$	11.65 eV	$3.52\ 10^{-22}\ m^2/eV$	$2.2\ 10^3\ m^2/J$
$3p\text{-}4p$	13.17 eV	$6.40\ 10^{-22}$ 3) m^2/eV	$3.53\ 10^3\ m^2/J$

The numbers are based on the work of:

1) C. Lloyd et al. (cf. [LLO72]) and Pesnelle ([PES70])

2) J. McConkey & Don ([CON73])

3) M. Peterson & Allen ([PET72])

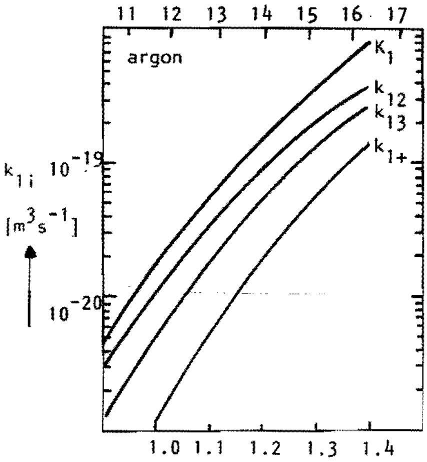

Fig. A.7
Rate coefficients for excitation and ionization from the neutral ground level $K_1 = k_{12} + k_{13} + k_{1+}$

For optically allowed transitions as the 3p-4s $^1P_1$, $^3P_1$ we could have used the expressions which couple the excitation cross-sections with the oscillator strength. The expression of Drawin [DRA66] allows, moreover, for adjustments to the experimental values with two parameters. However, even with these adjustments this formula does not show the linear increase at threshold as the experiment does. The use of Drawin's formula leads to an overestimate for $<\sigma v>$ of about a factor of 2 at $\hat{T}_e \approx$ 1eV. Therefore we have chosen the simple expression (a.12) with the linear dependence [POT79].
The total excitation rate for the resonant transitions is given in fig. A.7. In figure A.8 the total 4s de-excitation rate (k_{21}) is given, obtained from detailed balancing. This rate is obtained by averaging over the contributing sublevel rates taking into account the statistical weights of the 4s sublevels. For ionization from the ground states we have used the rates as calculated by Pots [POT 79]. He used the semi-empirical approach of Drawin and Katsonis.

In fig. A.7 also the ionization rate from the ground state k_{1+} is given. In this figure also the sum of $k_{12}+k_{13}+k_{1+}$ is drawn. For electron temperatures lower than 2eV this sum is by far the largest contribution to K_1, the total excitation and ionization rate from the ground state.

We note, that Pots has shown by comparison of experiment and model that the total excitation rate from the ground state is too large by a factor of 2.5-3 [POT79]. These experiments are performed at temperatures of 2.5eV and larger. In this study we have used the calculated values, corrected by a factor 2.5, in accordance with these results.

Both the procedures mentioned above are in principle empirical, since the results for both the allowed and forbidden transitions are adapted to experimental results. This procedure is especially adequate for excitations from the ground state for three reasons. At first, most experimental data for cross-sections concern excitation from the ground state. Secondly, especially for complicated atomic systems as ArI, the ground state is significantly different from the hydrogen ground state. Thirdly, for excitations from the ground state the excitation energy is larger than the kinetic energy, so that only the treshold behaviour of σ_E is important and an empirical adoption to experimental results improves the accuracy.

The situation is entirely different for (de) excitation from excited states. Experimental data are scarce or absent. The system resembles better a hydrogenic system especially for higher excited states. In addition the energy separation is usually in the same order or even smaller than the kinetic energy of the electrons, so that the high energy part of $\sigma(E)$ is also important. Here, one can hope on a better applicability of predictions based on calculations on the hydrogen system. Several descriptions are available here; from simple, Drawin [DRA66], to more elaborate semi-empirical descriptions as e.g. by Vriens and Smeets [VRI80]. For hydrogen also full calculations are available (cf. Van de Ree [REE81]). Vriens' [VRI80]approximations are in fair agreement with these calculations. As Pots did in his model we used for 4s-4p the Drawin approach; the results are shown in fig. A.8 and A.9. For ionization from the excited states 4s and 4p, we have also used semi-empirical expressions by Drawin, again following Pots.

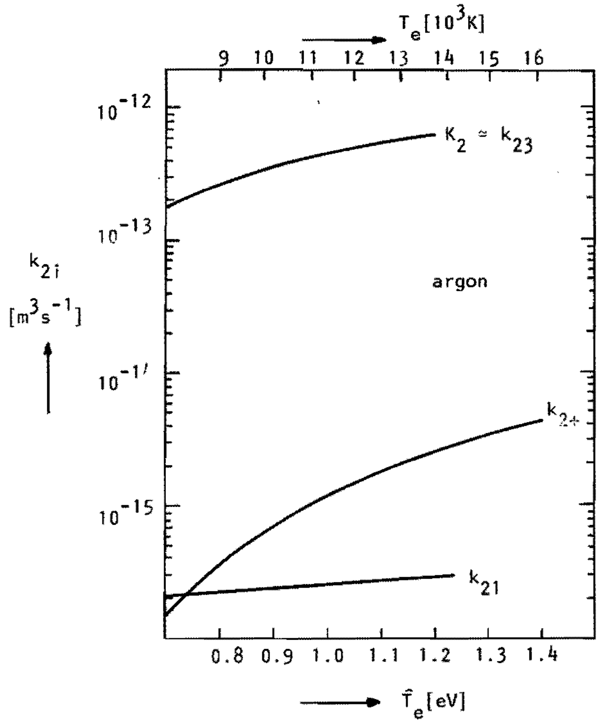

Fig. A.8
Rate coefficients for (de) excitation and ionization from effective level 2 (4s group). $K_2 = k_{21} + k_{23} + k_{2+} \approx k_{23}$

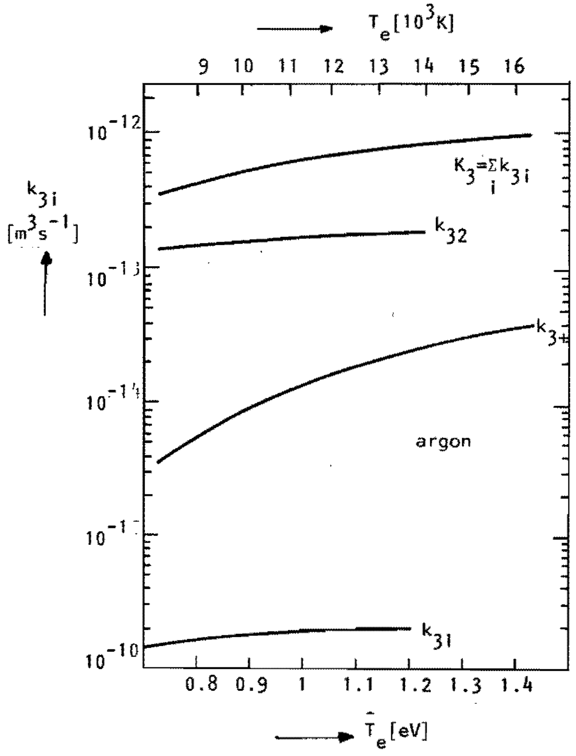

Fig. A.9

Rate coefficients for (de) excitation and ionization from effective level 3 (4p group). $K_3 = k_{31} + k_{32} + k_{3+}$

APPENDIX B

Line and continuum emission and absorption

Definition of spectral intensity

We define the spectral intensity I_λ as the radiant power per area, per solid angle and per wavelength. The dimension of I_λ is accordingly $Js^{-1}\ m^{-3}\ sterad^{-1}$.

Throughout the thesis the subscript λ denotes a spectral quantity. The relation between a spectral quantity A_λ in the wavelength domain and the corresponding quantity A_ν in the frequency domain is given by:

$$A_\nu = \frac{\lambda^2}{c} A_\lambda \qquad \text{(b.1)}$$

Emission and absorption coefficients

Line radiation

The emission coefficient $\varepsilon_{\lambda,L}$ for line radiation is given by:

$$\varepsilon_{\lambda,L} = \frac{hc}{4\pi\lambda_0} n_u A_{ul}\ P^e(\lambda) \qquad [J\ s^{-1}\ m^{-4}\ sterad^{-1}] \qquad \text{(b.2)}$$

and the line absorption coefficient $\kappa_L(\lambda)$ by:

$$\kappa_L(\lambda) = \frac{\lambda_0^4}{8\pi hc} \frac{g_u}{g_l} n_l A_{ul}\ P^a(\lambda) \qquad [m^{-1}] \qquad \text{(b.3a)}$$

or, including induced emission,by

$$\kappa_L'(\lambda) = \kappa_L(\lambda)\ \{1- \frac{g_l n_l}{g_u n_u} \frac{P^a(\lambda)}{P^{ie}(\lambda)}\}\ [m^{-1}] \qquad \text{(b.3b)}$$

The following notations have been used:

n_u, n_e density of the excited levels of the considered transition

g_u, g_l statistical weight of the excited levels

A_{ul} transition probability

λ_0 central wavelength of the line $\lambda_0=hc/E_u-E_l)$.

Here E_u, E_l represent the energy of the excited levels.

$P^e(\lambda)$, $P^a(\lambda)$, $P^{ie}(\lambda)$ line profile functions. $\int_{-\infty}^{+\infty} P(\lambda)d\lambda=1$.

Subscripts: u = upper level, l = lower level; L = line, C = continuum.

Superscripts: a = absorption, e = emission; ie = induced emission.

We will assume $P^e(\lambda) = P^a(\lambda) = P^{ie}(\lambda)$ (valid for PLTE conditions).

Continuum radiation

The total continuum emission coefficient is given by (for a singly ionized plasma):

$$\varepsilon_{\lambda,C} = \varepsilon_{\lambda,ff} + \varepsilon_{\lambda,fb} = \frac{C_1}{\lambda^2}\frac{n_e^2}{\sqrt{T_e}}\{[1-\exp(-\frac{hc}{\lambda kT_e})]\,\xi_{fb}(\lambda,T_e) +$$

$$+\exp(-\frac{hc}{\lambda kT_e})\,\xi_{ff}(\lambda,T_e)\} \qquad [\mathrm{J\ s^{-1}\ m^{-4}\ sterad^{-1}}] \qquad (b.4)$$

and the continuum absorption coefficient by

$$\kappa_C(\lambda) = C_2\,\lambda^3\,\frac{n_e}{\sqrt{T_e}}\,[1-\exp(-\frac{hc}{\lambda kT_e})]\,\{[\exp(-\frac{hc}{\lambda kT_e})-1]\,\xi_{fb}+\xi_{ff}\}\ [\mathrm{m^{-1}}] \qquad (b.5)$$

The values of the constants C_1 and C_2 are

$$C_1 = 1.632\ 10^{-43} \qquad [\mathrm{J\ K^{1/2}\ s^{-1}\ sterad^{-1}}] \qquad (b.6)$$

and $C_2 = 6.842\ 10^{-28}$ $\qquad [\mathrm{m^2 K^{1/2}}]$ (b.7)

The terms proportional to the so called ksi-factors, ξ_{ff} and ξ_{fb}, describe the contributions of the "free-free" (ff) or "brehmsstrahlung" radiation and of the "free-bound" (fb) or recombination radiation to the continuum.

The factors ξ_{ff} and ξ_{fb} introduce the specific electronic structure of the considered atom in the expressions for the continuum radiation [SCH67, HOF78].

For argon ξ_{ff} and ξ_{fb} are shown in fig. B.1 and B.2 for the spectral region of interest and for two values of the electron temperature.

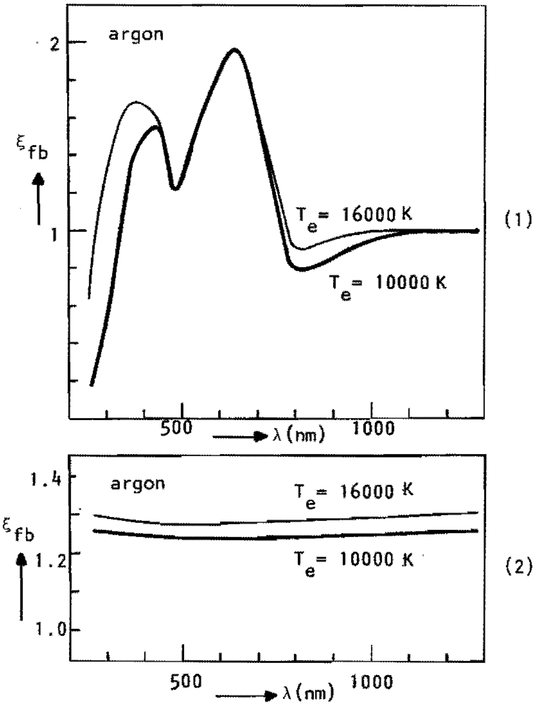

Fig. B.1 and B.2
Ksi-factor for argon.
ξ_{fb} from Schlüter [SCH65]
ξ_{ff} from Venugopalan [VEN71]

APPENDIX C

Radiative energy losses from the cascade arc plasma

We will derive approximate expressions for the radiative losses from the literature. We will attempt to express all losses in terms of local plasma parameters even if this introduces some inaccuracy.

a. Free bound radiation to the ground state, u_{fb}

The dominant radiation loss arises from the free-bound recombination radiation to the ground state atoms. An approximate expression for the recombination rate, $k_{+1}^{(2)}$ is [KAT76, TRO81]:

$$k_{+1}^{(2)} = 0.995\ 10^{-19}\ T_e^{-0.17}\ [m^3 s^{-1}] \tag{c.1}$$

The average foton energy, $h\upsilon \approx E_{01} + f(T_e)$ is (somewhat) larger than the ionization energy by the energy of the recombining electron.

The combined effect leads approximately to a temperature independent expression over the temperature range of interest. This leads to an average power loss (if absorption is neglected):

$$u_{fb}^{(1)} \approx n_e n_i k_{+1}^{(2)} [E_{01} + f(T_e)]/4\pi \approx 2\ 10^{-38}\ n_e^2 T_e^{-0.17}\ [Wm^{-3}\ sterad] \tag{c.2}$$

Here we have neglected the term $f(T_e)$ which is of the order of $\frac{3}{2}kT_e \approx 1.5eV$, with respect to $E_{01} \approx 15.8eV$.

As has been stated in section 2.2.2 a serious problem here is the finite absorption. The optical depth is of the order of one, which complicates the problem significantly. Hermann [HER68] calculated the excape for a

5mm argon arc at a pressure of 1 bar assuming LTE. His results are given in figure A.5. However, he ignores the radiation below the ionization threshold; both from Hofsaess [HOF78] as from Trommer [TRO81] it can be observed that there is significant radiation loss below threshold. This leads us to consider his calulation as an overestimate of the absorption.

Also a non-LTE behaviour will lead to stronger gradients and thus to more escape. On the other hand the LTE assumption will overestimate n_e and underestimate n_1. The latter effect will not be serious since the system values are not too far from the LTE-values. In view of the uncertainties we will calculate the free-bound radiation both for free escape ($\Lambda_{+1}^{(2)} = 1$) as for $\Lambda_{+1}^{(2)}$ according to Hermann.

The latter can be described as

$$\Lambda_{+1}^{(2)} \simeq 0.2\,\hat{T}_e^{3.7} \qquad \text{(c.3)}$$

The final expressions for the free bound radiation are summarised in table C.1.

b. Free-bound radiation (excluding the recombination radiation to the ground state), $\bar{u}_{fb}$, and free-free radiation (u_{ff}).

The expressions for $\varepsilon_{\lambda,ff}$ and $\varepsilon_{\lambda,fb}$ have been formulated in appendix B equations b.4 and b.5. Also shown in appendix B are the functions $\xi_{ff}(\lambda)$ and $\xi_{fb}(\lambda)$. More important, however, are the products

$$\alpha_{ff} = \xi_{ff}\exp\left(-\frac{hc}{\lambda kT}\right)\frac{hc}{\lambda kT_e}\frac{1}{\lambda^2} \quad \text{and} \qquad \text{(c.4)}$$

$$\alpha_{fb} = \xi_{fb}\left[1-\exp\left(\frac{hc}{\lambda kT}\right)\right]\frac{hc}{\lambda kT_e}\frac{1}{\lambda^2} \qquad \text{(c.5)}$$

These are shown in figure C.1 and C.2

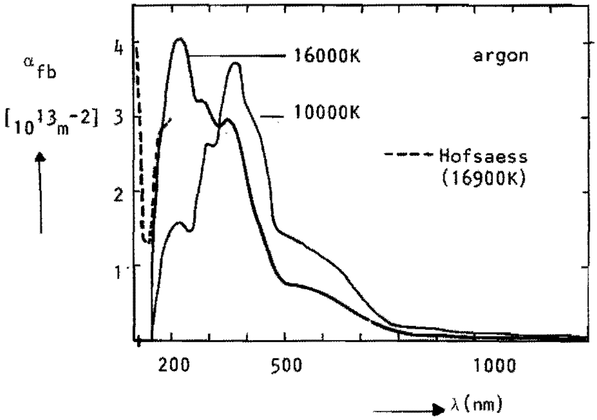

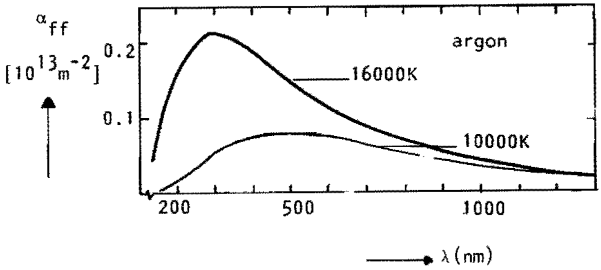

Fig. C.1 and C.2
The free-free and free-bound factors α_{ff} *and* α_{ff} *(cf. equation c.4 and c.5) as a function of the wavelength for two values of the electron temperature.*

In figure C.1 is also indicated the deviation that Hofsaess measured from the expected behaviour. This means that more radiation than is calculated may escape from the plasma. We also see that free-free radiation loss is unimportant as compared to the free-bound radiation loss. We integrated the expressions for $\varepsilon_{\lambda,ff}$ and $\varepsilon_{\lambda,fb}$ over the wavelength spectrum, for $260\,\mathrm{nm} \leq \lambda \leq 1440\,\mathrm{nm}$ to ~~obtain~~ the total continuum emission:

$$\bar{u}_{cont} = u_{ff} + \bar{u}_{fb} = \int_{260nm}^{1450nm} (\varepsilon_{\lambda,ff} + \varepsilon_{\lambda,fb})\,d\lambda \qquad (c.6)$$

for two values of the electron temperature (T_e = 10000K and T_e = 16000K).

From these values we obtain the following simplified relation for

u_{ff}, $\bar{u}_{fb}$ and $\bar{u}_{cont}$:

$$u_{ff} \simeq 7.80\ 10^{-39}\, n_e^2 \hat{T}_e^{1.27} \qquad [\mathrm{Wm^{-3}sterad}] \qquad (c.7)$$

$$\bar{u}_{fb} \simeq 5.93\ 10^{-38}\, n_e^2 \hat{T}_e^{-0.27} \qquad [\mathrm{Wm^{-3}sterad}] \qquad (c.8)$$

$$\bar{u}_{cont} \simeq 5.93\ 10^{-38}\, n_e^2 (\hat{T}_e^{-0.27} + 0.13\hat{T}_e^{1.27}) \qquad [\mathrm{Wm^{-3}sterad}] \qquad (c.9)$$

for $10000K \leq T_e \leq 16000K$

c. Line radiation.

c.1 Resonant lines.

4s-3p

From the expressions (a.4) and (a.5) we obtain for the optical depth

$\bar{\kappa}\bar{R} \simeq 10^4$ and trapping coefficient $\Lambda_{21} \simeq 3\;10^{-3}$

5s/3d-3p

For these lines the Lorentz width is larger, so the escape is stronger $\Lambda_{41} \simeq 10^{-2}$. Note that with $\frac{n_3}{n_2} \simeq 0.15$ and $\frac{n_4}{n_2} \simeq 0.06$, these radiative losses are small compared to the 4p-4s radiation loss, even if one considers the larger photon energy.

c.2 4p-4s radiation

This radiation is partially trapped, but the absorption is so small that we may approximate $\Lambda_{32} \simeq 1$. Then the radiative loss is equal to

$$u_{32} = n_3 A_{32} \frac{hc}{4\pi\lambda_{32}} \tag{c.10}$$

with

$$n_3 = \frac{n_e^2 g_3}{g_e g_+} \hat{C}_+ \hat{T}_e^{-1.5} \exp\left[\frac{E_{+3}}{kT_e}\right] \text{ (assumption of PLTE; cf equation 2.3)}$$

$$\hat{C}_+ = 0.3313\;10^{-27}\;[\mathrm{m}^{-3}\,\mathrm{eV}^{1.5}],$$

$$g_3 = 36;\; g_e g_+ \simeq 12;\; \hat{E}_{+3} = 2.588\text{ eV},\; A_{32} = 3.644\;10^7\;\mathrm{s}^{-1}.$$

$$u_{32} \simeq 7.0\;10^{-40}\; n_e^2\; \hat{T}_e^{-1.5} \exp\left[\frac{2.588}{\hat{T}_e}\right] \qquad [\mathrm{Wm}^{-3}\mathrm{sterad}] \tag{c.10a}$$

c.3 Other line radiation

In order to investigate the line radiation from other lines we will estimate the 3d/5s-4p losses. These are:

$$u_{43} = \frac{n_e^2\, g_4}{g_e g_+} \hat{C}_+ \hat{T}_e^{-1.5} \exp + \left[\frac{1.665}{\hat{T}_e}\right] A_{43} \frac{hc}{4\pi\lambda_{43}}\;; \tag{c.11}$$

with $A_{43} \simeq 1.27\;10^7\;\mathrm{s}^{-1}$ $\frac{hc}{\lambda_{43}} \simeq .923$ eV and $g_4 = 72$

$$u_{43} \simeq 3.1\ 10^{-40}\ n_e^2\ \hat{T}_e^{-1.5}\ \exp\left(\frac{1.655}{\hat{T}_e}\right) \qquad [\mathrm{Wm}^{-3}\mathrm{sterad}] \qquad (c.11a)$$

Also in view of the smaller argument of the exponent this radiative loss is considerable smaller than the 4p-4s loss.

In table C.1 we have summarized the results for the different forms of radiation loss, where only the 4p-4s radiation loss has been included as "line-radiation".

TABLE C.1 Approximate expressions for the various radiative loss mechanisms in the cascade arc plasma.
u_{ff} and $\bar{u}_{fb}$ are valid for 10000 K$\leqslant T_e \leqslant$ 16000 K

type of radiation loss	approximate expression for u [Wm^{-3}sterad]
radiative recombination to the neutral ground state	$u_{fb}^{(1)} \simeq 2.10^{-38}\ n_e^2\ \hat{T}_e^{-0.17}$
$u_{fb}^{(1)}$ with reabsorption	$u_{fb}^{(1)}\Lambda_{+1}^{(2)} \simeq 4\ 10^{-39}\ n_e^2\ \hat{T}_e^{-3.53}$
total free bound radiation to all excited states with exception of the neutral ground state	$\bar{u}_{fb} \simeq 5.91\ 10^{-38}\ n_e^2\ \hat{T}_e^{-0.27}$
free-free continuum	$u_{ff} \simeq 7.8\ 10^{-39} n_e^2 \hat{T}_e^{1.27}$
line radiation (4p-4s)	$u_{32} \simeq 7.0\ 10^{-40}\ n_e^2\ \hat{T}_e^{-1.5}\ \exp[\frac{2.588}{\hat{T}_e}]$

APPENDIX D

Physical Constants.

- SI units are used throughout this thesis.

- Special notations are:

  $\hat{n}_e$ for values of n_e expressed in $10^{22} m^{-3}$

  $\hat{T}_e$ for values of kT_e expressed in eV

  The following conversion may be used:

  1eV $\hat{=}$ 11605 K

  1eV = $1.6021892\ 10^{-19}$J.

- Values for the physical constants.

e	elementary charge	$1.6021892\ 10^{-19}$	C
m_e	electron rest mass	$9.109534\ 10^{-31}$	kg
k	Boltzmann constant	$1.380662\ 10^{-23}$	J/K
h	Planck constant	$6.626176\ 10^{-34}$	J/Hz
c	Speed of light in vacuum	$2.99792458\ 10^{8}$	m/s
ε_0	permittivity of vacuum	$8.85418782\ 10^{-12}$	F/m

REFERENCES

ASH63 Ashby, D.E.T.F. and D.F. Jephcott, Appl.Phys.Lett. 3 (1963) 13

ALP65 Alphe R.A. and D.R. White in: *Plasma diagnostics techniques*, Huddlestone, R.H. and Leonard, S.L., New York 1965.

BAE79 Baessler P. and M. Kock, J.Phys.B:Atom.Molec. Phys. 13 (1980) 1351

BAK69 Bakeyev, T.P. R. Narozhnaya, Ye. Rovinskiy and N.V. Cheburkin Radio Engineering and Electronic Physics, 14 (1969) 1727

BAT81 Batenburg, J., Report no. VDF/NT 81-11, Eindhoven Univ. of Techn., 1981

BAU75 Baum D., J. Hackman and J. Uhlenbusch, Plasma Physics, 17 (1975) 79.

BIB73 Biberman, L.M., V.S. Vorober, I.I. Yakubov, Sov.Phys.Uspekhi 15 (1973) 375.

BOB70 Bober, L. and R.S. Tankin, J.Quant.Spectrosc.Radiat. Transfer, 10 (1970) 991.

BRI77a Bridges J.M and W.R. Ott, Applied Optics, 16 (1977) 367

BRI77b Bridges J.M., W.R. Ott, E. Pitz, A. Schulz, D. Einfield and D. Stuck, Applied Optics, 16 (1977) 1788.

CAC76 Cacciatore M., M. Capitelli and H.W. Drawin, Physica 84C (1976) 267

CHA75 Chan P.W, M. Niimura, R.J. Churchill and B.C. Schanberg, Transactions on Plasma, Science PS-3 (1975) 174

CIL75 Cilliers, W.A., J.D. Hey and J.P.S. Rash, J.Quant.Spectrosc. Radiat. Transfer, 15 (1975) 963

CON73 McConkey, J.W. and F.G. Donaldsen, Can.J.Phys. 51 (1973) 914

DEV65 Devoto, R.S., The Physics of fluids, 9 (1966) 1230

DEV73 Devoto, R.S., The Physics of fluids, 16 (1973) 616

DRA66 Drawin, H.W., Report no. EUR-CEA-FC383, Fonteney-aux-Roses, 1966.

DRA69 Drawin, H.W., Z.Physics 225 (1969) 470

DRA73 Drawin, H.W., Phys.Letters 42A (1973) 423

EDD73 Eddy T.L., E. Pfender and E.R.G. Eckert, IEEE trans.plasma science, 1 (1973) 31

EIL75 Eilers, G.A.M., J.L. de Jong, R. Kool and H.N. Linssen, Eindhoven Univ. Techn., Cosor note R75-22, 1975

FAU79 Fauchais P. and J. Rakowitz, XIV ICPIG, Suppl. J. de Phys., C7 (1979) 289

FER79 Ferfers H., thesis, Univ. of Düsseldorf, 1979.

GAU70 Gautschi, W., SIAM, J. Numer.Anal., 7 (1970) 187

GER75 Gerrard, A. and J.M. Burch, *Introduction to Matrix Methods in Optics*, John Wiley & Sons, London 1975.

GRI63 Griem, H.R., Phys.Rev. 131 (1963) 1170

GRI64 Griem, H.R., *Plasma Spectroscopy*, McGraw Hill, New York, 1964

GUR63 Gurevich, D.B. and I.V. Podmoshenskii, Opt. and Spects. 15 (1963) 319

HER68 Hermann, W., Z.fur.Physik, 216 (2968) 33

HOF78 Hofsaess, D.,J.Quant.Spectrosc.Radiat.Transfer, 19 (1978) 339

KAT76 Katsonis, K., thesis, Unvers. Paris-Sud, 1976

KAF79 Kafrouni, H., Physica, 98c (1979) 100

KIN63 King, G.R. and G.J. Steward, New Scientist 17 (1963) 180

KLE69 Klein M., thesis Univers. of California, 1969

KOG66 Kogelnik, H. and T. Li, appl.Opt. 5 (1966) 155

KOP71 Kopainsky, J., Z.Physik 248 (1971) 417

KLM69 Kleen, W. und R. Müller, *Laser, Verstärkung durch induzierte Emission*, Springer Verlag Berlin, Heidelberg New York, 1969

LEC77 I.C.P.I.G. Berlijn, 1977

LLO72 Lloyd, C.R., E. Weigold, P.J.O. Tentsner and S.T. Houd, J.Phys.B 5 (1972) 1712

MAR63 Morgueardt, D.W., SIAM J., 11 (1963) 431

MIT73 Mitchner, M. and C.H. Kouger Jr., *Partially ionized gases* John Willey & Sons, New York, 1973

NIC79 Nick, K.P., Diplomarbeit, Univ. of Kiel, 1979

NIE79 Niessen T., At.Phys.Group-report, Eindhoven Univ.Techn. 1979.

OTT75 Ott, W.R. K. Behringer and G. Gieres, Applied Optics, 14 (1975) 2121

OTT76 Ott, W.R., National Bureau of Standards, Washington, D.C. 20234, SP456 (1976) 107

PEA67 Pearce, T.W., A.K. Hoeksberg and T.O. Poehler, Rev.Sci.Instr. 38 (1967) 835

PES70 Pesnelle A., thesi, Univ. Paris-Sud, 1970

PET72 Peterson, L.R. and J.E. Allen, J.Chem.Phys. 56 (1972) 6068

PIE78 Pierstorff G., thesis, Univ. of Düsseldorf, 1978

PRE77 Preston R.C., J.Quant.Spectrosc.Radiat. Transfer, 18 (1977) 337

POT78 Pots, B.F.M., B. van der Sijde and D.C. Schram, Physica, 94c (1978) 369

POT79 Pots, B.F.M., thesis, Eindhoven Univ. Techn., 1979

RIC71 Richter J., Proc. of the 10th ICPIG, Oxford, 1971, invited paper: Partial Thermodynamic Equilibria in plasmas.

REE81 V.d. Ree, J. private communication

SAL52 Salzer, H.E., R. Zucker and R. Capuano, J.Res. NBS 48 (1952) 111

SAU78 Saunders, R.D., W.R. Ott and J.M. Bridges, Applied Optics 17 (1978) 593

SCH65 Schlüter, D., Z.Astrophys. 61 (1965) 57

SCH67 Schlüter, D., Z. Physik 201 (1967), 80

SOB72 Sobel'man, I.I., *Introduction to the theory of atomic spectra*, Perganon Press, Oxford, 1972

SPI65 Spitzer, L., *Physics of Fully Ionised Gases*, John Wiley & Sons, New York, 1965

SCH67 Schlüter, D., Z. Physik 201 (1967), 80

SOB72 Sobel'man, I.I., *Introduction to the theory of atomic spectra*, Perganon Press, Oxford, 1972

STE79 Steen, J. van der, At.Phys.Group, report Eindhoven Univ. Techn., 1979

TRO81 Trommer, G., Proc. 15e Int.Conf.on Phen.Ion.fases, Minsk (1981), 1614

UHL70 Uhlenbusch J., E. Fischer and J. Hackmann, Z.Physik 239 (1970) 120

UHL74 Uhlenbusch J., *Gaseous electronics*, North-Holland Publishing Company, Amsterdam, 1974

VAC76 Vacque, S., J.P. Dinguirard, H. Kafrouni and I. Pages, J.Quant. Spectrosc.Radiat.Transfer 17 (1977) 755

VAE81 Vaessen, P.H., J. Arts, J.M. Houben, Proc. 5e Int.Symp.Plasma Chem. Edinburgh (1981) 115

VEN71 Venugopalan, M., *Reactions under Plasma Conditions*, John Wiley & Sons, New York, 1971

VOS53 Vos, de, Thesis, Univ. of Utrecht, 1953

VRI80 Vriens, L. and A.H.M. Smeets, Phys.Rev. A22 no. 3 (1980) 940

WIE69 Wiese, W., M.W. Smith and B.M. Miles *Atomic Transition Probabilities*, NSRDS-NBS 22, 1969

WIL62 Wilson, R., J.Quant.Spectrosc.Radiat. Transfer, 2 (1962) 477

ZAB73 Zapesochnyi, I.P., A.I. Imre, A.I. Dashchenko, V.S. Vukstich, F.F. Danch and V.A. Kel'man, Sov.Phys. JETP 36 (1973) 1056

SUMMARY

This thesis deals with the study of the validity of the assumption of Local Thermal Equilibrium (LTE) in the description of the parameters of a thermal argon plasma.

Our aim is twofold.

As the studied plasma is close to, but not completely in equilibrium, we first attempt to obtain a simple description of the plasma in terms of an LTE model in which suitable corrections for the deviations of the plasma parameters from their LTE values is introduced.
To this end the plasma parameters are studied by means of a diagnostic method in which the assumption of LTE is not made.
The evaluation of the usefullness of this method is the second aim of this thesis.

The considered diagnostic method is based on measurement of the source function, i.e. the ratio of emission and absorption of suitably chosen spectral lines in the argon neutral system.
The electron temperature, T_e, follows directly from the obtained value of the source function. From the total line intensity of the measured spectral transition the electron density, n_e, is obtained. Here the assumption of Partial Local Thermal Equilibrium (PLTE) is used.
We have compared the measured relationship between n_e and T_e at atmospheric pressure, with the corresponding relationship obtained from LTE calculation of the plasma parameters and found deviations from the LTE composition.

A simple collisional radiative model for the argon neutral spectrum has been developed, allowing us to study the mechanisms that are responsible for the deviations from LTE in the argon arc plasma.
The deviations are explained in terms of an overpopulation of the neutral ground level with respect to the corresponding Saha population. This overpopulation proves to be partly caused by radiative recombination of ions and electrons and partly by inward diffusion of neutral atoms.
The description of the overpopulation of the ground state density in terms of radiative recombination and diffusion, is satisfactory at high current values and close to the arc axis, but does not account fully for the overpopulation at lower values of the current and close to the walls.

With the obtained values of the plasma parameters the total excitation and ionization rate coefficient of the neutral ground level has been derived and also values for the electrical and thermal conductivities. These agree reasonably with the theoretical values.
For a more accurate determination of the electron density a two wavelength laser interferometer has also been used. The results of these experiments are in agreement with the spectroscopic determination of n_e from the source function, within experimental error.

Finally a pulsed experiment is described. Pulsed operation of the arc (by pulsing the arc current) can provide additional information concerning the mechanisms that determine the equilibrium in the plasma.
The first results of this experiment indicate that the rise of the temperature, following a sudden current rise, is determined by the change of internal energy of the plasma

SAMENVATTING

Dit proefschrift bevat een studie over de geldigheid van de aanname van Lokaal Thermisch Evenwicht (LTE) in de beschrijving van de parameters van een thermisch argon plasma.

Ons doel is tweeledig.
Aangezien het onderzochte plasma nabij evenwicht, maar niet volledig in evenwicht is, proberen wij allereerst een eenvoudige beschrijving van het plasma te vinden in termen van een LTE model waarin geschikte correcties voor de afwijkingen van de plasma parameters ten opzichte van hun LTE waarden worden ingevoerd.
Hiertoe worden de plasma parameters onderzocht met een methode waarin de aanname van LTE niet wordt gebruikt.
Het vaststellen van de bruikbaarheid van deze methode is het tweede doel van dit proefschrift.

De beschouwde diagnostiek gaat uit van een meting van de bronfunctie, d.i. de verhouding van emissie en absorptie van geselecteerde spectraallijnen uit het argon neutraal spectrum.
De elektronentemperatuur, T_e kan direkt bepaald worden uit de verkregen waarde van de bronfunktie.
De elektronendichtheid n_e wordt verkregen uit de totale lijn-intensiteit van de gemeten spectraalovergang, waarbij de aanname van Partieel Lokaal Thermisch Evenwicht (PLTE) wordt gebruikt.
We hebben de gemeten relatie tussen n_e en T_e bij atmosferische druk vergeleken met de overeenkomstige relatie die volgt uit LTE berekeningen van de plasma samenstelling en afwijkingen van de LTE samenstelling gevonden.

Er is een eenvoudig botsings-stralingsmodel voor het argon neutraal spectrum ontwikkeld waarmee mechanismen die verantwoordelijk zijn voor de afwijkingen van LTE in het plasma van een argon boog bestudeerd kunnen worden.
De afwijkingen worden verklaard in termen van een overbezetting van het neutraal grondniveau ten opzichte van de overeenkomstige Saha bezetting. Deze overbezetting blijkt gedeeltelijk te worden veroorzaakt door stralingsrecombinatie van ionen en elektronen en gedeeltelijk door diffusie van neutrale atomen naar binnen.
De beschrijving van de overbezetting van de grondtoestand in termen van stralingsrecombinatie en diffusie is bevredigend voor hoge stroomsterkten en dicht bij de as van het plasma, maar verklaart de overbezetting bij lage stroomsterkten en dicht bij de wand niet volledig.

Met de verkregen waarden van de plasma parameters is de totale gemiddelde botsingsdoorsnede voor botsingsexcitatie en ionisatie vanuit de grondtoestand bepaald, alsmede waarden voor de elektrische en thermische geleidingsvermogens. Deze komen redelijk overeen met de theoretische waarden.
Voor een nauwkeuriger bepaling van de elektronendichtheid is tevens een twee golflengten laser interferometer gebruikt.
De resultaten van deze experimenten komen binnen de meetonnauwkeurigheid goed overeen met de spectroscopische bepaling van n_e d.m.v. de bronfunktie.

Tenslotte wordt een gepulst experiment beschreven.
Het gepulst bedrijven van de boog (door de boogstroom te pulsen) kan aanvullende informatie verschaffen omtrent de mechanismen die het evenwicht in het plasma bepalen.
De eerste resultaten van dit experiment duiden aan dat de temperatuurstijging na een plotselinge stroomtoename bepaald wordt door de verandering van de interne energie van het plasma.

NAWOORD

Het onderzoek dat in dit proefschrift wordt beschreven is verricht in de onderwerpgroep Atoom- en Plasmafysica van de afdeling der Technische Natuurkunde van de Technische Hogeschool Eindhoven.
Naast een goed instrumentarium, is een prettige samenwerking met allen die aan een onderzoek meewerken van belang voor het slagen ervan. Aan beide voorwaarden is in deze groep ruimschoots voldaan.
Voor deze prettige samenwerking in de loop van de afgelopen 5 jaar, dank ik alle leden van de groep.
Tevens wil ik hierbij herinneren aan de gezamenlijke inspanningen met Volkmar Helbig van de Universiteit van Kiel (BRD) tijden de voorbereiding en uitvoering van de interferometrie. Dat ondanks alle mogelijke tegenslagen toch nog een goede opstelling tot stand is gekomen is zeer zeker mede te danken aan zijn doorzettingsvermogen en onstuimige werklust.
Voor de min of meer als vanzelfsprekend beschouwde medewerking van de groep Molecuulfysica bij het beschikbaar stellen van apparatuur en kennis t.b.v. de automatisering van de data collectie, opslag en verwerking is een speciaal woord van dank op zijn plaats.

De vele metingen bij dit onderzoek zijn dankzij de technische assistentie van John Bleize en Lambert Bischops en de bijstand van Bertus Hüskens voor wat betreft het elektronische gedeelte mogelijk geworden.
In dit verband moet ook de hulp van de studenten H. Verwey, J. Cremers, C. de Meyer, J. Janssen, J. v.d. Steen, F. Niessen, S. Groh en A. Buuron vermeld worden.
Voor de altijd snelle manier van reageren van de afdelingswerkplaats,

wanneer er weer eens een spoedkarwei moest worden opgeknapt ben ik zeer erkentelijk.

Een zeer speciaal woord van dank voor het "redaktieteam" van dit proefschrift:

Erna Baaijens, voor de geweldige hulp op het juiste moment.

Mieke Beesems, voor het getoonde geduld en het razendsnelle typewerk.

Lambert Bisschops, voor het maken van een gedeelte van de tekeningen.

Huub Jeuken, voor de samenwerking en de adviezen bij het drukken.

Petra van Zutphen, voor het uitzetten van een gedeelte van de grafieken en tabellen.

Behalve "blood, sweat and tears" was het ook een ervaring apart.

En "last but not least" wil ik José danken voor de steeds aanwezige glimlach en goede zorgen, ondanks de afgelopen tijden van "afzien".

LEVENSLOOP

26 oktober 1950	geboren te Willemstad (Curaçao)
mei 1969	eindexamen HBS-b, Radulphus College te Willemstad (Curaçao)
juni 1976	doctoraal examen Technische Natuurkunde (vaste stof fysica) aan de Technische Hogeschool Eindhoven
juli 1976 - december 1980	Wetenschappelijk Ambtenaar in de groep Atoom- en Plasmafysica, afdeling der Technische Natuurkunde, Technische Hogeschool Eindhoven.

STELLINGEN

behorende bij het proefschrift van

R.J. Rosado

I

Een zeer nauwkeurige bepaling van de elektronentemperatuur in thermische bogen is mogelijk door met behulp van interferometrie de elektronendichtheid te meten.

Dit proefschrift (hoofdstuk 5)

II

Door gedurende korte tijd de ontladingsstroom door het plasma van een cascadeboog te vergroten tot aanzienlijk hogere waarden, kunnen op een eenvoudige manier plasma's van een hoge dichtheid worden gerealiseerd. Dit opent perspectieven voor de bestudering van zwak-Debye plasma's.

Dit proefschrift (hoofdstuk 6)

III

Bij het onderzoek naar transportgrootheden van zwak-Debye plasma's dient rekening gehouden te worden met afwijkingen van lokaal thermisch evenwicht.

IV

In veel gevallen wordt ten onrechte de elektronentemperatuur bepaald uit de gemeten verhouding van bezettingen van aangeslagen niveaus.

M.R. Teixeira en F.C. Rodriguez, Journal of Physics D12 (1970) p.2173
J.J.A.M. van der Mullen et.al., Physics Letters 79A (1980) p.51

V

Botsings-detachment bepaalt de vorm van de achterflank van de Trichelpuls die optreedt in een negatieve corona ontlading.

VI

Holle kathode bogen zijn bij uitstek geschikt om toegepast te worden als handzame lijnstralings- en deeltjesbronnen.

L.A. Bisschops en F. Niessen, persoonlijke mededeling.

P.G.A. Theuws, proefschrift, Technische Hogeschool Eindhoven (1981).

VII

Onafhankelijke bepalingen van karakteristieke grootheden, uitgevoerd door verschillende groepen met bij voorkeur verschillende methodieken vergroten bij overeenstemming de betrouwbaarheid van het resultaat.
Met name voor de ontwikkeling van primaire en secundaire standaarden is dit van zeer groot belang.

V. Helbig et.al., Proceedings of the 5th Europhysics sectional conference on the atomic and molecular physics of ionized gases, Dubrovnik, September 1980, p.130.

VIII

Bij de toepassing van lasers bij materiaalbewerking heeft de struktuur van de lasermode grote invloed op de kwaliteit van het resultaat.

J. Uhlenbusch, persoonlijke mededeling (1981).

IX

Voor de correcte uitvoering van de oefenvormen van de japanse bewegingskunst Aikido is het een vereiste dat men de eigen bewegingsenergie, via spiraalvormige patronen, in overeenstemming brengt met die van de partner. Het beoefenen van deze vorm van sport door kinderen draagt dan ook bij tot een harmonieuze ontwikkeling van het kind in de omgang met anderen.

X

Een werkelijke doorbraak in de industriële innovatie vereist een meer positieve instelling van ondernemers ten aanzien van nieuwe technische mogelijkheden.

Eindhoven, 23 oktober 1981